

NATIONAL INSTITUTE FOR FUSION SCIENCE

Frontiers of Pulse Power Technology Development

Edited by Weihua Jiang

( Received - Nov. 9, 2021 )

NIFS-PROC-124

Feb. 5, 2023

This report was prepared as a preprint of work performed as a collaboration research of the National Institute for Fusion Science (NIFS) of Japan. The views presented here are solely those of the authors. This document is intended for information only and may be published in a journal after some rearrangement of its contents in the future.

Inquiries about copyright should be addressed to the NIFS Library, National Institute for Fusion Science, 322-6 Oroshi-cho, Toki-shi, Gifu-ken 509-5292 JAPAN.

E-mail: tosho@nifs.ac.jp

**<Notice about copyright>**

NIFS authorized Japan Academic Association For Copyright Clearance (JAC) to license our reproduction rights and reuse rights of copyrighted works. If you wish to obtain permissions of these rights, please refer to the homepage of JAC (<http://jaacc.org/eng/>) and confirm appropriate organizations to request permission.

# **Frontiers of Pulse Power Technology Development**

Edited by Weihua Jiang

January 7-8, 2020  
National Institute for Fusion Science  
Toki, Gifu, Japan

## **Abstract**

The papers appeared in this volume of research report have been presented at the “Symposium on Frontiers of Pulsed Power Technology Development” held by National Institute for Fusion Science. They report the present status and recent progress in experimental and theoretical studies on pulsed power technology and its applications.

**Keywords:** pulsed power, particle beam, plasma, high power microwave, material processing, pulsed discharge, high voltage.

## **PREFACE**

The collaborative research symposium on “Frontiers of Pulsed Power Technology Development” was held at National Institute for Fusion Science (NIFS), Toki, on Jan. 7-8, 2020. This symposium was attended by 36 researchers and students from universities, institutes, and industrial companies. At the symposium, 30 research papers were presented, each of them was followed by fruitful discussions. This symposium has provided an excellent environment for information exchange between the researchers and has promoted collaborations between NIFS and universities.

I would like to express my sincere thanks to all of the symposium attendees, all of the paper authors, and the staffs of National Institute for Fusion Science.

Weihoa Jiang  
Extreme Energy-Density Research Institute  
Nagaoka University of Technology

## LIST OF ATTENDEES

A. Tokuchi	Pulsed Power Japan, Inc.
K. Nakata	Pulsed Power Japan, Inc.
K. Nakayama	Pulsed Power Japan, Inc.
T. Kawamura	Tokyo Institute of Technology
Y. Ikeda	Tokyo Institute of Technology
J. Hasegawa	Tokyo Institute of Technology
Y. Ishikawa	Tokyo Institute of Technology
Y. Matsueda	Tokyo Institute of Technology
R. Tani	Tokyo Institute of Technology
T. Jinnai	Tokyo Institute of Technology
K. Takahashi	Iwate University
Y. Saito	Iwate University
T. Yamada	Iwate University
H. Ito	University of Toyama
M. Terada	University of Toyama
R. Haruki	University of Toyama
K. Yamamoto	University of Toyama
K. Watanabe	University of Toyama
M. Takao	University of Toyama
K. Takasugi	Nihon University
T. Kikuchi	Nagaoka University of Technology
K. Takahashi	Nagaoka University of Technology
Y. Uchida	Nagaoka University of Technology
D. Sasaki	Nagaoka University of Technology
Y. Miyamoto	Nagaoka University of Technology
H. Aoyama	Nagaoka University of Technology
T. Fukuda	Nagaoka University of Technology
T. Kobayashi	Nagaoka University of Technology
Y. Feng	Nagaoka University of Technology
K. Sakurai	Nagaoka University of Technology
T. Ishida	Nagaoka University of Technology
A. Kamada	Nagaoka University of Technology
H. Kuno	Nagaoka University of Technology
T. Deguchi	Nagaoka University of Technology
W. Jiang	Nagaoka University of Technology
T. Ozaki	National Institute for Fusion Science

## CONTENTS

<b>Divergent Gas-Puff Z Pinches with Ar and H<sub>2</sub> Mixtures</b>	<b>1</b>
K. Takasugi and M. Nishio (Nihon University)	
<b>Measurement of High-frequency Characteristics of High-Voltage Semiconductors</b>	<b>8</b>
K. Nakayama, A. Tokuchi, H. Mori (Pulsed Power Japan Lab., Inc.)	
<b>Development of High-Voltage Pulse Power Supplies Using Semiconductor Devices</b>	<b>12</b>
K. Nakata, Y. Mushibe, H. Mori, A. Tokuchi (Pulsed Power Japan Lab., Inc.)	
<b>Numerical Study of Conical Terahertz Emission From Laser Created Plasma</b>	<b>14</b>
T. Kobayashi, T. P. Otsuka and N. Yugami (Utsunomiya University)	
<b>Experiments of Forward THz Emission From Femtosecond Laser Created Plasma With Applied Transverse Electric Field</b>	<b>15</b>
T. Fukuda, T. P. Otsuka and N. Yugami (Utsunomiya University)	
<b>K<math>\alpha</math> Spectra of Medium-Z Plasma Dominated by M-shell Multipleionization By An Ion Beam</b>	<b>16</b>
Y. Ikeda, T. Okui, and T. Kawamura (Tokyo Institute of Technology)	
<b>Study on Electrode Structure of Reflex Triode Virtual Cathode Oscillator for High Power Microwave Generation</b>	<b>20</b>
R. Haruki, R. Tanaka, and H. Ito (University of Toyama)	
<b>Energy Evaluation of Pulsed Heavy Ion Beams in Bipolar Pulsed Accelerator</b>	<b>25</b>
M. Terada, H. Ishida, and H. Ito (University of Toyama)	
<b>Dependence of Anode Shape on High Intensity Ion Beam Characteristics in Plasma Focus Device</b>	<b>30</b>
K. Yamamoto, Y. Sagano, and H. Ito (University of Toyama)	
<b>Influence of Voltage Polarity on Development of Pulsed Discharge Over Water Surface And Active Species Production</b>	<b>36</b>
H. Takayama, M. Takeda, K. Karashima, K. Takahashi, K. Takaki, and T. Namihira (Iwate University and Kumamoto University)	
<b>Influence of Drying Rate and Quality Changes on Hot Air Drying Processing of Spinach using Pulse Electric Field</b>	<b>41</b>
T. Yamada, Y. Kouya, K. Takahashi, K. Takaki, T. Orikasa, J. Kamagata, and H. Aoki (Iwate University and Inc Nichirei Foods)	
<b>Silicon Wafer Etching by Burst-Mode High-Power Inductively Coupled Ar/CF<sub>4</sub> Plasmas with 150 kHz Band Frequency</b>	<b>46</b>
Y. Saito, K. Shibata, K. Takahashi, S. Mukaigawa, K. Takaki, K. Yukimura, H. Ogiso, and S. Nakano (Iwate University and AIST)	

# Divergent Gas-Puff Z Pinches with Ar and H<sub>2</sub> Mixtures

Keiichi Takasugi, Mineyuki Nishio\*

*Institute of Quantum Science, Nihon University*

*\*Anan College, National Institute of Technology*

## ABSTRACT

Experiment of a divergent gas-puff z pinch using Ar and H<sub>2</sub> mixture was conducted. When the Ar partial pressure was lowered while keeping the total plenum pressure at 5.0 atm, a strong pinch occurred until the Ar partial pressure was 1.5 atm. Soft x-ray emission was observed and a single spot image was observed. It is considered that plasma with electron temperature of about 1 keV was obtained.

## Keywords

Divergent gas-puff z pinch, Hot spot, Soft x-ray, Radiation cooling, Gas mixture

## 1. Introduction

The plasma focus discharge is made in gas-filled state, and the plasma contracts while collecting the gas and converges at a point in front of the center electrode[1, 2]. Rayleigh-Taylor instability does not occur in the plasma contraction process. Furthermore, neutrons are easily generated by the discharge using D<sub>2</sub> gas. However, this neutron generation is not thermonuclear reaction and is explained by the beam-target model associated with the generation of ion beam[3]. Since the plasma focus starts to discharge due to the surface discharge of the insulator, the input energy is considered to be limited by the deterioration of the insulator[4]. The gas-puff z pinch is an efficient x-ray source with repeated operation[5, 6]. The divergent gas-puff z pinch has been devised for the purpose of realizing a highly efficient point radiation source having both advantages[7]. The divergent gas-puff z pinch performs gas-puffing from the center conductor to shrink the plasma three-dimensionally and generate a hot spot in front of it. Efficient energy input has been performed compared to the conventional gas-puff z pinch[8].

Experiments have been carried out in the gas-puff z pinch with three kinds of gases, Ne, Ar, and Kr, and it has been shown that the heavier gas have shown larger input energy and stronger x-ray emission[9]. Higher electron temperatures have been obtained with heavier elements in metal wire z-pinch experiments[10]. A mixed gas experiment of D<sub>2</sub> and Ar has been carried out in the gas-puff z pinch, and it has been shown that the pinch plasma has been stabilized by a small amount of Ar gas[11]. It has been pointed out that radiative cooling works to stabilize the pinch plasma[12]. Taken together, these results suggest that mixing a small amount of heavy elements in the fusion fuel stabilizes the pinch plasma and creates a high temperature plasma. It has become possible to see thermonuclear reaction rather than beam-target reaction in plasma focus.

In this study, mixed gas discharges of Ar and H<sub>2</sub> were performed in the divergent gas-puff z pinch. Stronger pinch formation is expected compared to the straight nozzle by using the divergent gas-puff. Electron temperature of about 1 keV has been obtained in a pure Ar discharge, and the spectrum of He-like Ar ions

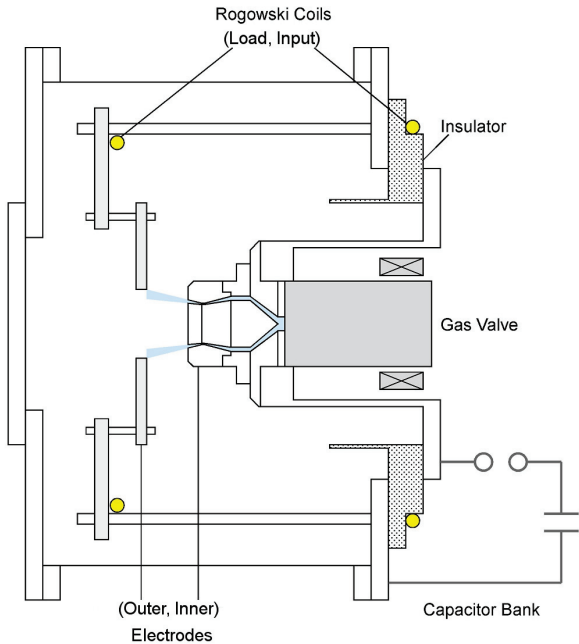


Fig. 1: Schematic diagram of the SHOTGUN III-U divergent gas-puff z-pinch device. The gas is puffed from the annular Laval nozzle mounted on the inner electrode.

has been observed [13, 14]. It is considered that similar spectra is observed in the mixed gas discharge of Ar and H<sub>2</sub>, and soft x-ray emission is considered to indicate the presence of He-like Ar ion. By changing the mixing ratio of Ar and H<sub>2</sub>, the effect on pinch plasma production was investigated from the observation of its spatial structure and hot spots.

## 2. Experimental Setup

The experiment was carried out with the SHOTGUN III-U z-pinch device at Nihon University (Fig. 1). The energy storage section of the device consists of a 40 kV 18  $\mu$ F capacitor bank, with a typical discharge current of 200 kA. The feature of the device is that it can be charged both positively and negatively. In this experiment, in order to suppress the generation of hard x-ray, the bank was charged to -25 kV and operated.

Gas-puffing was performed by a high-speed gas valve installed in the center conductor and a divergent annular Laval nozzle mounted on the inner electrode. The divergence angle of the nozzle was 10° with respect to the central

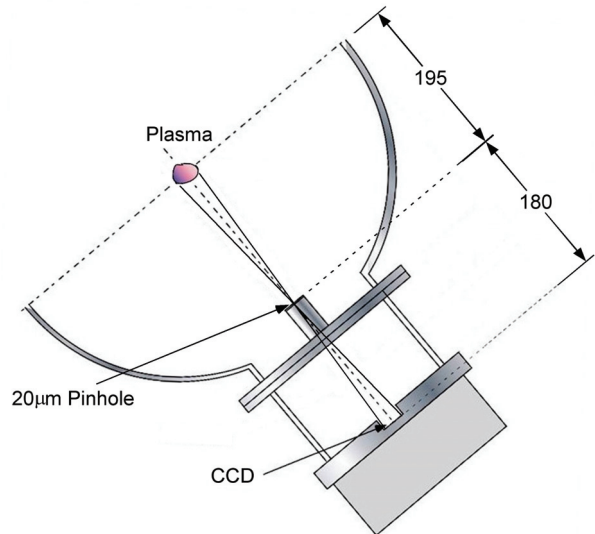


Fig. 2: Soft x-ray pinhole camera with CCD. A 15  $\mu$ m Be filter is used for removing soft x-ray with energy less than 1 keV.

axis. The diameter of the nozzle was 30 mm, and the outer electrode had a hole of 60 mm. The distance between the inner electrode and the outer electrode was 30 mm.

The gas valve was evacuated and then filled with Ar and H<sub>2</sub> gas. The filling pressure was measured using a Pfeifer piezo gauge APR266. The combined pressure was 5.0 atm.

The discharge current was measured by Rogowski coils placed on the input side and the load side. A scintillation probe (SCI) with a 3 mm thick plastic scintillator was used to monitor soft x-ray. Since there is a Be filter of 5  $\mu$ m, soft x-ray below 700 eV was blocked, so only K-shell radiation of Ar ions can be captured. An x-ray diode (XRD) with Ni photocathode without filter was also used to monitor soft x-ray and extreme ultraviolet light. Since the XRD was not calibrated, the absolute amount cannot be measured, but it has a wide sensitivity range from ultraviolet light to soft x-ray [15]. The XRD can mainly capture L-shell and M-shell radiations of Ar ion.

A high-speed camera was used to observe the contraction process of the pinch plasma. A gated image intensifier Hamamatsu V3063U was used for the camera, and observation was made with the gate width of 20 ns.

Hot spots were observed using a pinhole

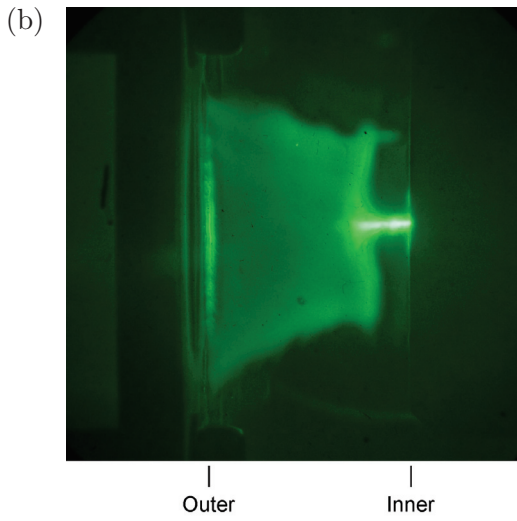
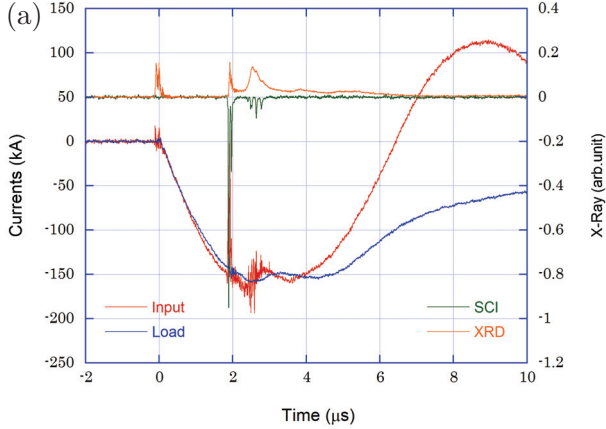


Fig. 3: (a) Discharge currents and soft x-ray signals and (b) a gated image of discharge at  $\text{Ar:H}_2 = 5.0:0.0$ .

camera equipped with a CCD (Fig. 2). The CCD used was made by Laser-Laboratorium Göttingen e.V. The sensitivity region is  $< 1 \text{ nm} \sim 1,100 \text{ nm}$ , and the pixels are  $6.45 \mu\text{m}$  and  $1,392 \times 1,040$  pixels. A pinhole with a diameter of  $20 \mu\text{m}$  and a Be filter with a thickness of  $15 \mu\text{m}$  were used. Since soft x-ray below  $1 \text{ keV}$  was blocked, only the K-shell radiation of Ar ions could be captured. The distance from the center of the device to the pinhole was  $195 \text{ mm}$ , and the distance from the pinhole to the CCD was  $180 \text{ mm}$ . The images were colorized using NIH ImageJ software.

### 3. Pinch Formation

The pinch formation was investigated by observing the discharge currents, the soft x-ray signals (SCI and XRD) and the gated images

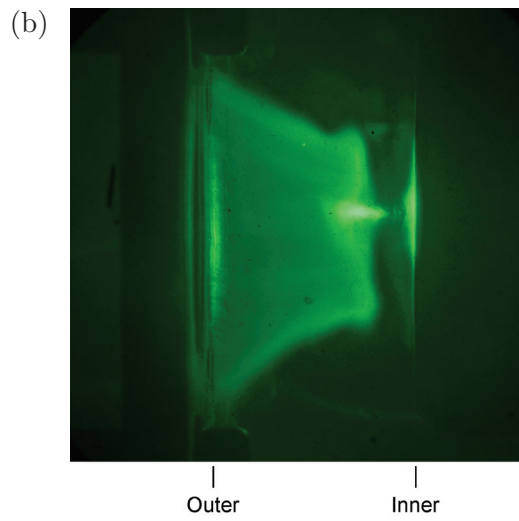
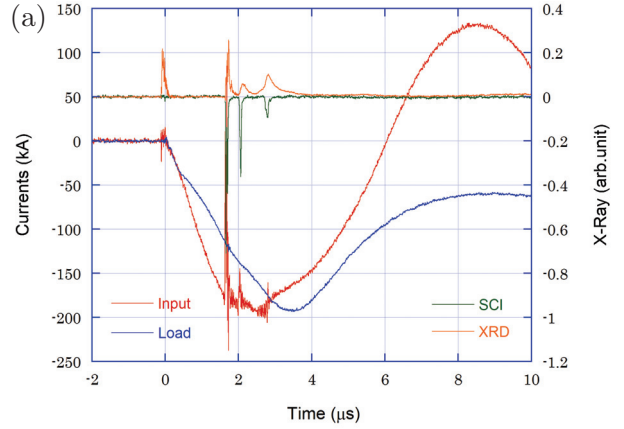


Fig. 4: (a) Discharge currents and soft x-ray signals and (b) a gated image of discharge at  $\text{Ar:H}_2 = 1.5:3.5$ .

of the plasma with changing the mixing ratio of Ar and  $\text{H}_2$ . When the partial pressure ratio was changed while keeping the total pressure constant, the discharge condition changed because the mass of the entire gas changed. The gas pressure between the electrodes increases with time from the gas puff. Therefore, the optimum delay time of discharge from the gas puff was found from preliminary experiments so that the pinch time was almost constant even if the partial pressure ratio was changed. If the pinch time is almost constant, the discharge current at the time of pinch is also considered to be almost constant.

Figure 3(a) shows discharge currents and soft x-ray signals at Ar  $5.0 \text{ atm}$  and  $\text{H}_2$   $0.0 \text{ atm}$ . The delay time of discharge from gas puff was  $0.50 \text{ ms}$ . A pinch occurred at  $1.65 \mu\text{s}$  after the start of discharge and a sharp signal was gen-

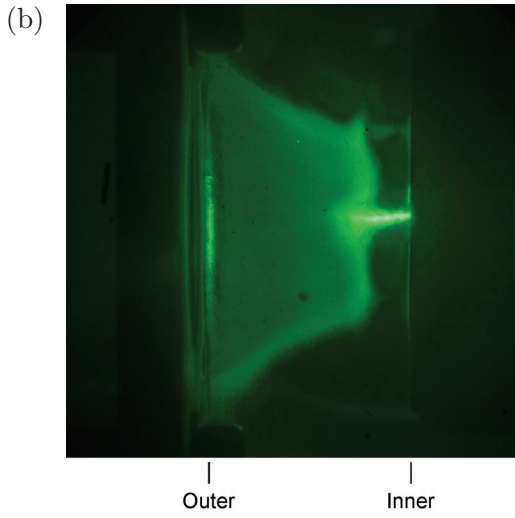
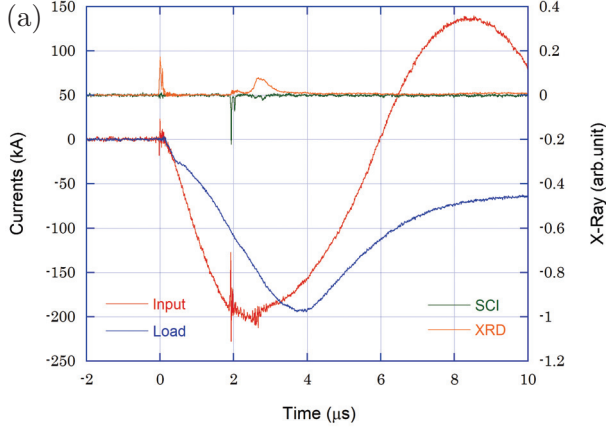


Fig. 5: (a) Discharge currents and soft x-ray signals and (b) a gated image of discharge at  $\text{Ar:H}_2 = 1.0:4.0$ .

erated in SCI and XRD. Signal values were in arbitrary units, but SCI was  $-0.95$  and XRD was  $0.16$ . Although the current dip occurred at the pinch, the input current just before the pinch was  $-152$  kA and the load current was  $-141$  kA. Up to the pinch, the input current and load current were almost the same. Figure 3(b) shows the plasma image taken 40 ns before the pinch under the same condition. A pinch column was formed on the left side of the inner electrode over 7 mm. The rest of the area did not shrink, and the shape of the initial discharge was maintained.

Figure 4(a) shows discharge currents and soft x-ray signals for Ar 1.5 atm and  $\text{H}_2$  3.5 atm. The delay time of discharge from gas puff was 0.58 ms. The first pinch occurred at  $1.66 \mu\text{s}$  after the start of discharge and a sharp signal was generated on SCI and XRD. The signal val-

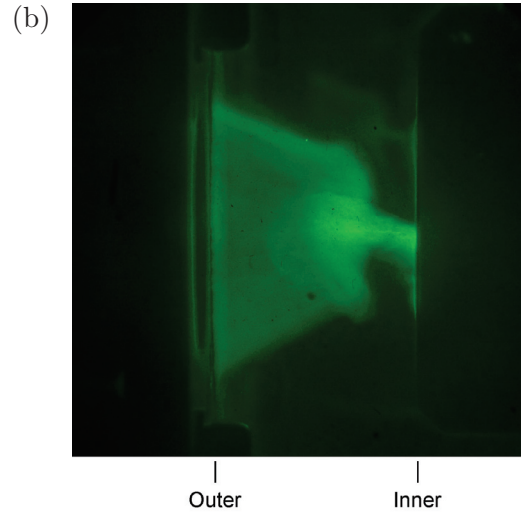
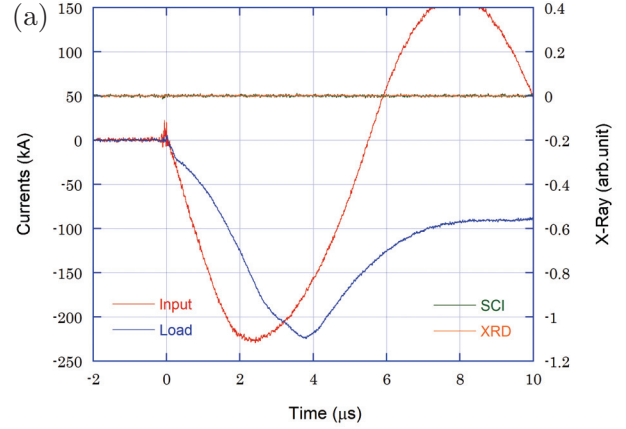


Fig. 6: (a) Discharge currents and soft x-ray signals and (b) a gated image of discharge at  $\text{Ar:H}_2 = 0.5:4.5$ .

ues were SCI  $-0.71$  and XRD  $0.26$ . The value of the input current just before the pinch was  $-184$  kA and the load current was  $-112$  kA. The difference between the input current and the load current was a little larger. Figure 4(b) shows the plasma image taken 2 ns after the pinch under the same condition. The pinch column has already broken and moved to the left. The other parts did not move much.

Figure 5(a) shows discharge currents and soft x-ray signals for Ar 1.0 atm and  $\text{H}_2$  4.0 atm. The delay time of discharge from gas puff was set to 0.64 ms. The pinch occurred at  $1.94 \mu\text{s}$  after the start of discharge and a sharp signal was generated on SCI and XRD. Signal values were  $-0.22$  for SCI and  $0.02$  for XRD. The value of the input current just before the pinch was  $-192$  kA and the load current was  $-97$  kA. The difference between the input current and the

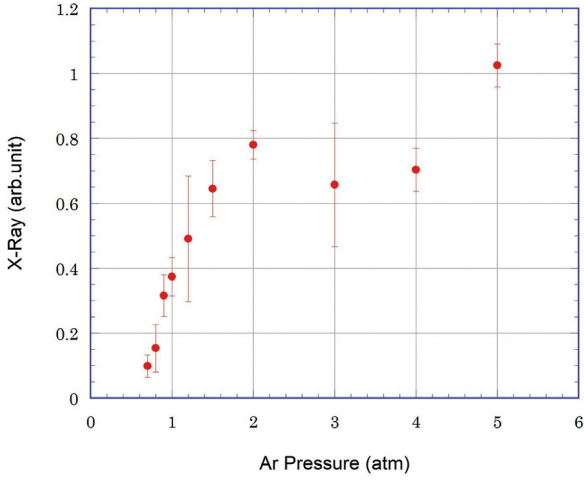


Fig. 7: Soft x-ray intensity as a function of Ar partial pressure.

load current was large. Figure 5(b) shows the plasma image taken 36 ns before the pinch under the same condition. The plasma contracted to form a pinch column.

Figure 6(a) shows the discharge currents and soft x-ray signals for Ar 0.5 atm and H<sub>2</sub> 4.5 atm. The delay time of discharge from gas puff was 1.00 ms. No soft x-ray signal was observed anymore and we could not know when the pinch occurred. Figure 6(b) shows the plasma image taken at time 2.00  $\mu$ s. The plasma was shrinking, but no strong pinch was formed. At this time, the input current value was -220 kA and the load current was -123 kA. The difference between the input current and the load current was large.

Figure 7 shows the intensity of SCI signal with respect to the partial pressure of Ar. The SCI signal was almost constant when the Ar partial pressure was higher than 1.5 atm. When the partial pressure was smaller than 1.5 atm, the signal strength decreased significantly.

#### 4. Hot Spot Formation

Hot spots were observed using a pinhole camera equipped with a CCD. Figure 8 shows a CCD image for Ar 5.0 atm and H<sub>2</sub> 0.0 atm. A clear single spot image was observed. The spot size was 84  $\mu$ m in the horizontal direction (axial direction) and 63  $\mu$ m in the vertical direction (radial direction). Figure 9 shows a

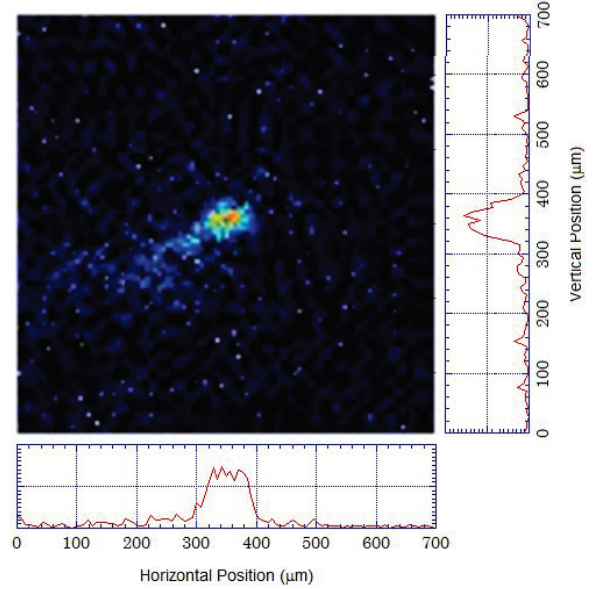


Fig. 8: Soft x-ray pinhole image of the pinch plasma at Ar:H<sub>2</sub> = 5.0:0.0.

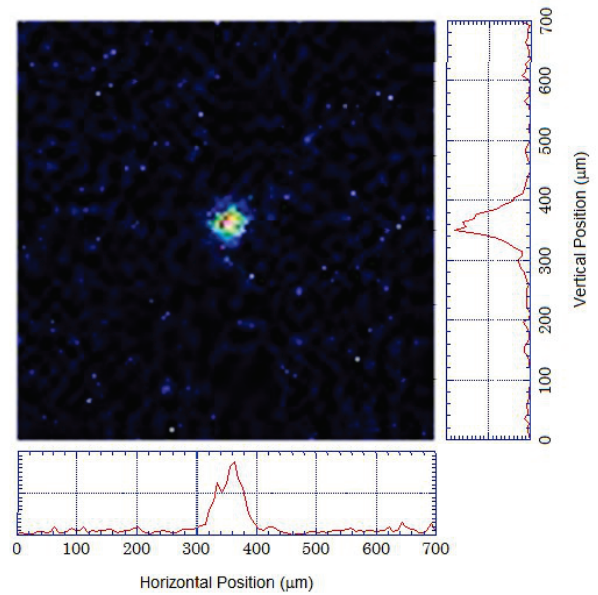


Fig. 9: Soft x-ray pinhole image of the pinch plasma at Ar:H<sub>2</sub> = 1.5:3.5

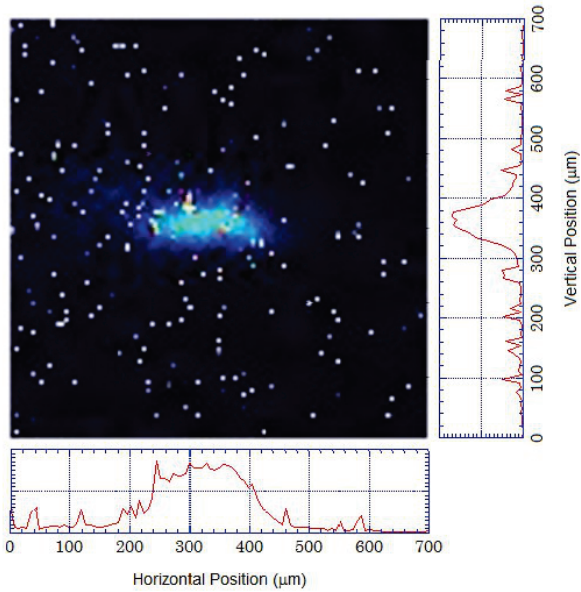


Fig. 10: Soft x-ray pinhole image of the pinch plasma at Ar:H<sub>2</sub> = 1.0:4.0.

CCD image for Ar 1.5 atm and H<sub>2</sub> 3.5 atm. A clear single spot image was observed. The spot size was 70 μm in the horizontal direction (axial direction) and 70 μm in the vertical direction (radial direction). Figure 10 shows a CCD image for Ar 1.0 atm and H<sub>2</sub> 4.0 atm. A spot image extending in the axial direction was observed. The spot size was 224 μm in the horizontal direction (axial direction) and 91 μm in the vertical direction (radial direction). Since 20 μm pinholes were used for the measurement, it is considered that each of them was observed as large as 40 μm.

## 5. Summary and Discussion

The experiment of mixed gas of Ar and H<sub>2</sub> was conducted using a divergent gas-puff z pinch. When the Ar partial pressure was lowered while keeping the total pressure at 5.0 atm, a strong pinch occurred until the Ar partial pressure was 1.5 atm. Soft x-ray emission was observed and a single spot image was observed. Although no spectroscopic measurement was performed, it is considered that plasma with the electron temperature of about 1 keV was obtained. Soft X-ray emission became weak when Ar partial pressure was further reduced. When the Ar partial pressure was 1.0 atm, the soft x-ray im-

age spread in the axial direction was observed. When the Ar partial pressure reached 0.5 atm, a strong pinch no longer occurred and soft x-ray was no longer observed.

From the above, it is considered that a pinch plasma with an electron temperature similar to that of a pure Ar discharge was obtained in a mixed gas discharge of Ar and H<sub>2</sub> with an Ar partial pressure of about 30 %. It was shown that a stable pinch can be obtained and a high-temperature plasma can be obtained by mixing a small amount of Ar to H<sub>2</sub>. He-like ions in pinch plasmas has often been observed, because stable plasma compression has been performed until the generation of He-like ions, which is the effect of radiation cooling. By expanding this knowledge, it is thought that a plasma with electron temperature of about 10 keV can be stably generated by mixing a small amount of heavy element such as Xe into the fusion fuel. The possibility of thermonuclear fusion by pinch discharge has become more apparent.

## References

- [1] N. V. Fillipov, T. I. Fillipova and V. P. Vinogradov, Nucl. Fusion Suppl. **2**, 577 (1962).
- [2] J. W. Mather, Phys. Fluids Suppl. **7**, S28 (1964).
- [3] S. P. Moo, C. K. Chakrabarty and S. Lee: IEEE Tras. Plasma Sci. **19**, 515 (1991).
- [4] W. Kies: Plasma Phys. Cont. Fusion **28**, 1645 (1986).
- [5] J. Shiloh, A. Fisher and N. Rostoker: Phys. Rev. Lett. **40**, 515 (1978).
- [6] P. G. Burkhalter, J. Shiloh, A. Fisher, and R. D. Cowan: Appl. Phys. **50**, 4532 (1979).
- [7] K. Takasugi and E. Kiuchi: Plasma Fusion Res. **2**, 036 (2007).
- [8] K. Takasugi and E. Kiuchi: NIFS-PROC **72**, 17 (2008).
- [9] K. Takasugi T. Miyamoto, K. Moriyama and H. Suzuki: AIP Conf. Proc. **299**, 251 (1993).

- [10] A. S. Safronova et.al.: IEEE Trans. Plasma Sci. **40**, 3347 (2012).
- [11] J. Bailey, Y. Ettinger, A. Fisher, and N. Rostoker: Appl. Phys. Lett. **40**, 460 (1982).
- [12] J. Bailey: Ph. D Thesis, U. C. Irvine (1983).
- [13] K. Takasugi and H. Akiyama: Jpn. J. Appl. Phys **43**, 6376 (2004).
- [14] V. Shlyaptseva et.al.: IEEE Trans. Plasma Science. **46**, 3842 (2018).
- [15] R. H. Day, P. Lee, E. B. Saloman, and D. J. Nagel: LA-7941-MS (1981).

# Measurement of High-frequency characteristics of high-voltage semiconductors

K. Nakayama, A. Tokuchi, H. Mori

*Pulsed Power Japan Lab., Shiga, Japan*

**Abstract**—This paper is summary of test results that we investigated high-frequency characteristics of high-voltage semiconductors that are sold on the market, which were performed at development process of 5 kV pulsed power supply using resonant charge. At first, we considered circuit prototype and evaluated current characteristics of some FETs and shotkey-barrier diodes(SBDs). As a result, we found that the smaller stray capacitor was the faster resonant current dumped. At the next, we set up circuit with better-characteristic component selected from the results and tested output with comparative low voltage. Finally we strengthened withstand voltage and achieved 5 kV output.

**Keywords**—pulse, development, FET, SBD, characteristic

## I. Introduction

Recently, a trend using semiconductor for high-voltage application of pulsed power and high power switching gets more active. Electron tubes(e.g., vacuum tube, thyatron, etc.) have used at these application traditionally, but these device had many disadvantage, for example it was expensive, short lifetime, unstable, low repetitive. The semiconductor can improve those disadvantage extremely and is expected to substitute those role. In Addition compared with Si, to commercialize SiC that have high withstand voltage, low-on resistor and high-thermal conductivity is started so application for pulsed power is being advanced rapidly.

5 kV pulsed power supply we develop now use technique called “resonant charge”. The resonant charge means a method that can charge with about twice the voltage of a main DC power supply by switching on a current of any resonant frequency and then switching off at the half period(see fig.1). This also allows the charged capacitor load to return the voltage to the power supply in the opposite direction of the charge(This means recirculation). From this principle, a high resonant frequency is required to speed up the rise time. In this study, we investigated how the characteristics of SiC semiconductors under such a special high frequency operation affect the design.

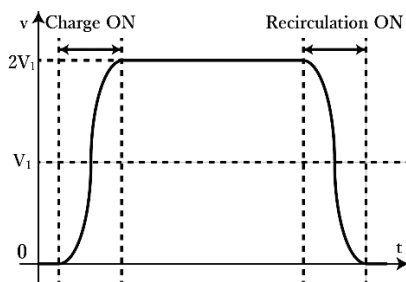


Fig.1 Schematic of resonant charge and recirculation

## II. Purpose

In this paper, the high-frequency characteristics of several SiC FETs and shotkey-barrier diodes(SBDs) with respect to current are measured and the differences between the components are seen. Finally, we select the most suitable one for the power supply under development.

## III. Methods

### A. The current characteristics of FETs

The test circuit is shown in fig.2. D1 and D2 are the parasitic diodes of the FET and C2 is the load. The operation of the circuit is as follows.

1. Switch on FET1 and flow the resonant current in the dark orange path to charge the capacitor.
2. Switch on FET2 to return the charge that load has by the light orange path to the power supply.

The resonant period is about 500 ns, and the rise and fall time of the output voltage are about half of that, about 250 ns. We prepared three kinds of FETs (Sample A1, A2, B). and measured output voltage by changing the FET2 while fixing the FET1 by B. Note that only B is not SiC.

### B. The current characteristics of SBDs

We prepared two kinds of SBDs (Sample C, D).

#### 1) Test of SBD alone

The test circuit is shown in fig.3. The FET A1 and SBD C is used. The resonant period is about 80 ns. The supply voltage was set to 200 V and the trigger input was set to 25 ns. The current waveform was measured on the cathode side of the SBD.

#### 2) Test on a real circuit

The test circuit is shown in fig.4. The explanation of the circuit operation is the same as III.I.A. The FETs are A1, and

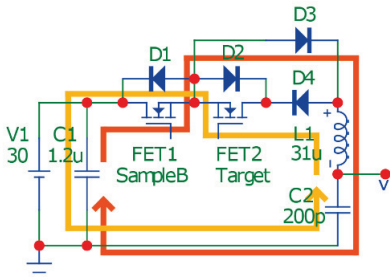


Fig.2 FET-characteristics test circuit

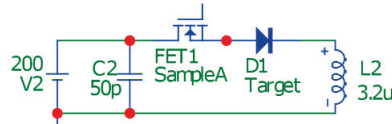


Fig.3 SBD-characteristics test circuit 1

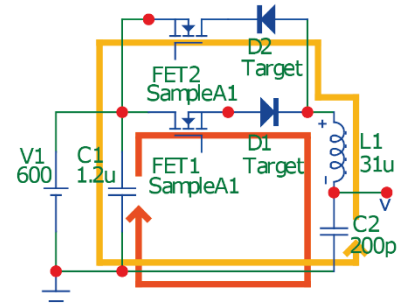
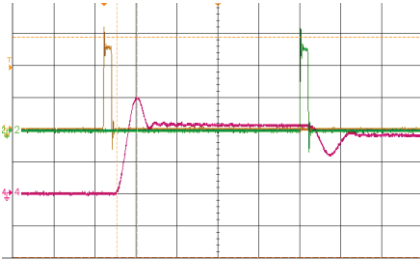
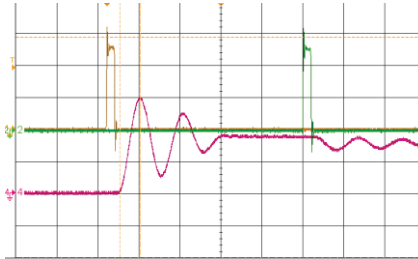


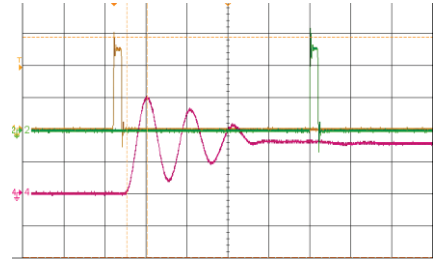
Fig.4 SBD-characteristics test circuit 2



(a) Sample A1



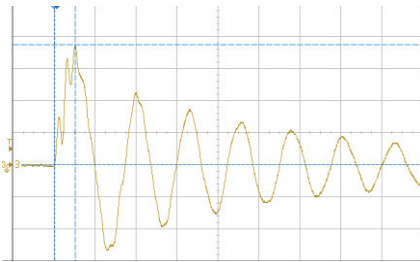
(b) Sample A2



(c) Sample B

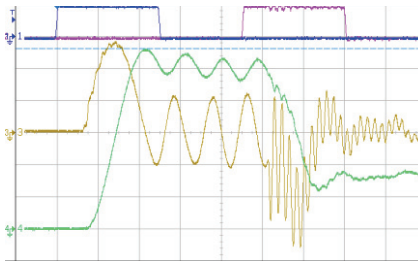
500 ns/div, Red : Voltage 20 V/div, Yellow : Trigger for charge, Green : Trigger for recirculation

Fig.5 Results of FET test

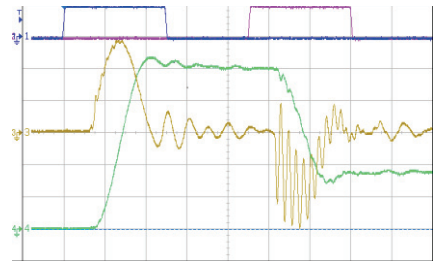


Sample C

50 ns/div, Yellow : Current 0.2 A/div



(a) Sample C



(b) Sample D

200 ns/div, Green : Voltage 200 V/div, Yellow : Current 0.5 A/div

Fig.6 Results of SBD test 1

Fig.7 Results of SBD test 2

the SBDs are C or D. Note that the same SBDs are used for D1 and D2. The resonant period is about 500 ns. The supply voltage is 600 V, and the trigger input is 500 ns. The output voltage and current were measured.

#### IV. Results

##### A. The current characteristics of FETs

The results are shown in fig.5. It can be seen from the three waveforms that after the output voltage rises to about 60 V by the FET1 trigger, the resonant current continues to flow and the output voltage drops even after the trigger is turned off. Especially as shown in the waveforms of A2 and B, the resonant current flowed as if FET1 and 2 were short-circuited after the output rise. We selected FET A1 for the power-supply design because the resonant current attenuation was the fastest when the A1 was used. In addition, difference between the voltage after rising up and the power supply voltage decreased due to voltage drop, so even in the case of A1, little recirculation was possible and the voltage remained in the load capacitor.

##### B. The current characteristics of SBDs

###### 1) Test of SBD alone

The results are shown in fig.6. From the waveforms, it was found that the resonance current continued to flow as if it ignored the SBD and FET even though the trigger was input only 50 ns.

###### 2) Test on a real circuit

The results are shown in fig.7. From the waveform(a), it was found that the SBD C allowed the resonant current to flow without damping during the period when the trigger was not input, whereas as shown in the waveform(b) D allowed the current to dump faster and the vibration was smaller. As a result, we selected D for the power supply.

#### V. Consideration

##### A. The current characteristics of FETs

The parasitic capacitance of the FET(Cds) is one of the possible reasons why the decay rate of the resonance current changes significantly when the FET is changed. Cds of diodes

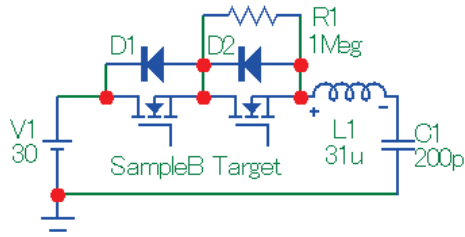


Fig.8 Circuit of FET-parasitic capacitance measurement

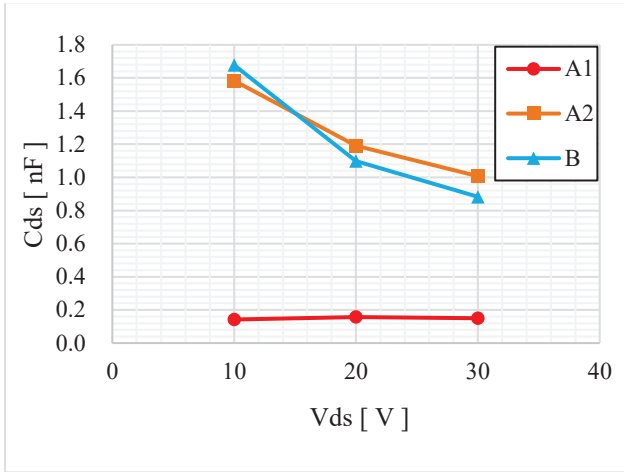
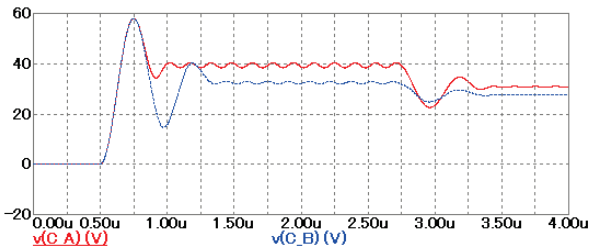
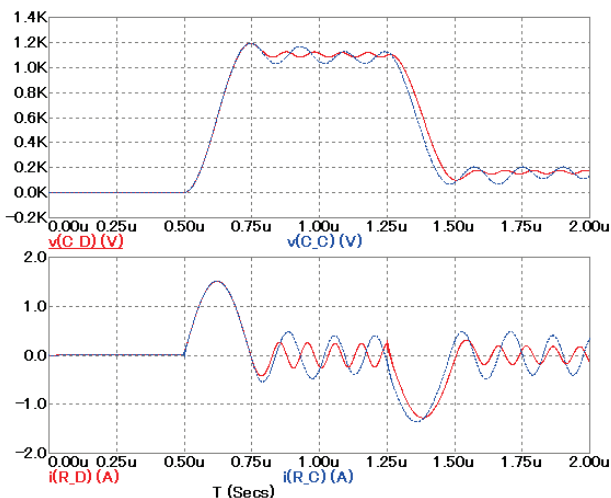


Fig.9 Results of calculation of FET-parasitic capacitance



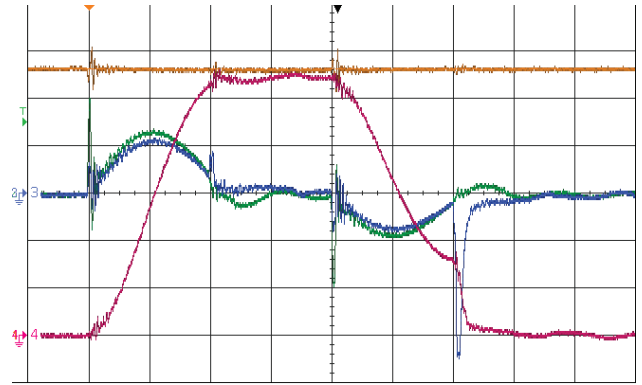
Red : SampleA1 (Cds=150 pF), Blue : SampleB (Cds=900 pF)

Fig.10 Results of FET-test simulation



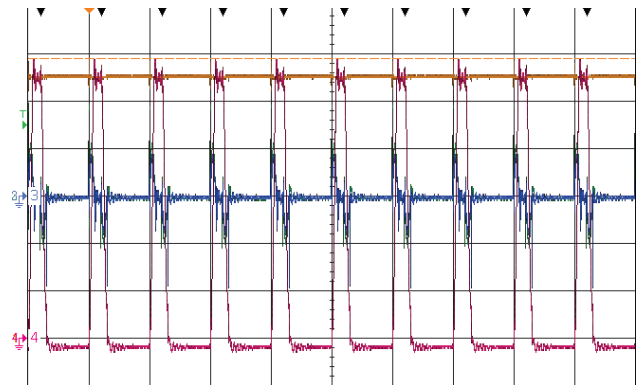
Red : SampleD (Cak=5 pF), Blue : Sample C (Cak=50 pF)

Fig.11 Results of SBD-test2 simulation



500 ns/div, Red : Voltage 1 kV/div, Green : Input Current 2 A/div, Blue : Output Current 2 A/div

Fig.12 Waveform of 5 kV output, 1 shot



10 μs/div, Red : Voltage 1 kV/div, Green : Input Current 2 A/div, Blue : Output Current 2 A/div

Fig.13 Waveform of 5 kV output, 100 kHz

and FET1 is also involved in the waveforms, but the capacitance of FET2 is the most important in this test. In order to know the actual Cds value, an additional test was performed with fig.8 circuit. FET2 is permanently turned off and FET1 is turned on to apply a steep voltage between drain and source of FET2(Vds). We measured the resonant current flowing at that time, and calculated the Cds from the period of waveforms. The results are shown in fig.9. The Cds value of FET A1 that attenuate current fastest was about a quarter of that of the other FETs at Vds=30 V. We used these value to simulation of fig.2 circuit, then similar waveforms to that of fig.5 was obtained(see fig.10).

### B. The current characteristics of SBDs

#### 1) Test of SBD alone

The reason why the resonant current flowed as if to ignore the diode was due to the influence of the parasitic capacitance of the diode(Cak), as in V.A. Especially in this test, the capacitance of the resonant capacitor was as small as 50 pF, so the effect of Cak could not be ignored.

#### 2) Test on a real circuit

The reason for the difference in the speed of decay of the resonant current between the SBD C and D is also Cak. The simulation results show that the vibration after the rise increases with increasing Cak(see fig.11). This is consistent with the waveform in fig.7.

## VI. Development of power supply

From IV. Results, it was decided to use FET A1 and SBD D. Fig.7(b) shows the waveform when these are used for the circuit. This circuit had to be upgraded to a 5kV output. Therefore, a 2.5 kV-DC power supply was used, and the withstand voltage was improved by using several FETs and SBDs in series. In addition, a droop compensation circuit was added to flatten the flat top, and a circuit to discharge the remaining charge in the load after recirculation. The rise time was set to an arbitrary value by changing the inductance of the coil. As a result of the above modifications, the output of a fig.12 waveform was achieved. The rise time is 1  $\mu$ s and the wave height is 5 kV. Finally, the waveform when this is operated at 100 kHz is also shown in fig.13.

## VII. Conclusion

This test was conducted as part of the development of the power supply. That power supply uses a technique called resonant charging, which deals with high-frequency resonant currents. It was necessary to investigate the behavior of the switching SiC semiconductor under such high-frequency operation.

In conclusion, it is necessary to select a device with as small a parasitic capacitance as possible in order to handle high-frequency currents in normal applications of semiconductor devices. When the parasitic capacitance is large, the current flows in the FET even if it is not turned on, while in the diode, the current flows in the opposite direction as if it were short-circuited. In addition, in circuits that handle high frequencies, there is a concern that the parasitic capacitance will have a greater effect to the circuit because the capacitance value in the circuit will be smaller accordingly.

In the development of the power supply, although the load is as small as 200 pF, we were able to develop a device that satisfies the specifications for a voltage of 5 kV and 100 kHz repetition operation because we were able to perform sufficient tests to select the components.

# Development of high-voltage pulse power supplies using semiconductor devices

Kyosuke Nakata A), Yoichi Mushibe A), Hitoshi Mori A), Akira Tokuchi A)

A) Pulsed Power Japan Laboratory Ltd. (PPJ)

**Abstract**— We have developed a high-voltage pulse generator that assumes a capacitive load using a high-speed, high-withstand voltage SiC semiconductor with small switching loss. In order to apply a high voltage pulse to the capacitive load, two high withstand voltage switches for charging and discharging are required. This time, we conducted a test of a small power supply in which eight series SiC-MOSFET for charging and discharging, respectively, were applied to a load of 10 pF with a peak voltage of 8 kV repeatedly at 1 kHz.

**Keywords**—

## I. Introduction

Today, most switches have been replaced by semiconductors. However, in the field of pulsed power, vacuum tubes are still used. This is because the withstand voltage of a vacuum tube is much higher than that of a semiconductor, and the rise time is shorter. However, it has the disadvantage of high losses and longevity due to deterioration.

Recently developed SiC semiconductors have higher voltage resistance and higher repetition rate compared to conventional Si semiconductors. In addition, the switching loss is small and the life is semi-permanent. Although the withstand voltage of this SiC semiconductor is not as high as that of a vacuum tube, it is possible to obtain sufficient withstand voltage and current by connecting it in series and parallel.

A small capacitive power supply with an output voltage of up to 8 kV was developed by using 8 series of 1.7 kV SiC-MOSFETs with a withstand voltage of 1.7 kV.

## II. Contents of development

Devices that use high electric fields, such as electron guns and electrostatic kickers, require a power supply that can output high voltages. In addition, since parallel metal plates are used to generate the electric field, it can be regarded as a capacitive load. It is also preferable that the rise and fall of the load voltage is also fast.

The power supply to be developed has a wide range of applications, with an output voltage of up to 8 kV and a rise and fall time of 100 ns or less. We also aim to create a compact pulse power supply that can be placed on a tabletop and operated by setting the pulse width and output frequency of the output waveform.

The resistive load does not store any charge, so a square wave can be output with a single switch. However, the capacitive load stores a charge, so a single switch cannot output a square wave (Fig. 1). In the case of capacitive loads, a circuit to discharge the capacitor charge using some method is required.

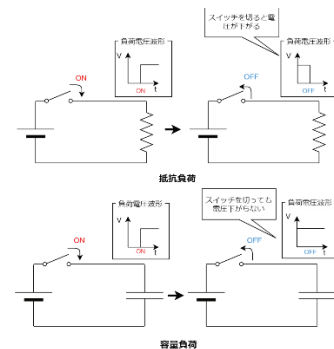


Figure 1: Difference between resistance and capacity.

Therefore, this power supply can discharge the charge of the load by making a switch circuit for charge-discharge separately from the switch circuit for charging (Fig.2). In this way, a square wave can be added to the capacitive load.

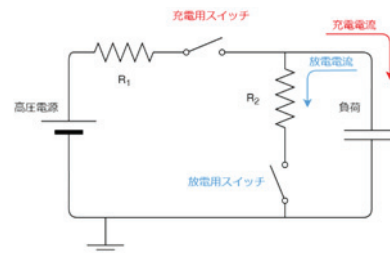


Figure 2: Charge and discharge circuit

## III. Production and testing of power supplies

The target specifications of the power supply to be developed for Tabel 1 are shown.

The output voltage, pulse width, and frequency are variable, and can all be operated from the power supply board. They are controlled by an FPGA.

The 8kV switch uses 8 series of 1.7kV SiC-MOSFETs with a 1.7kV breakdown voltage to reduce the number of switching elements, increase the rise and fall times, and achieve high switching efficiency.

Table 1: Requirement of Output voltage

Parameters	Requirement Specifications
Wave Form	Square
Polarity	Positive
Load Capacity	10pF
10%-90% Rise Time	Under 100ns
10%-90% Fall Time	Under 100ns
Voltage	0V~8000V
Pulse Width	200ns~100μs
Frequency	1~1000Hz

Figure 3 shows the appearance of the produced pulsed power supply. There are buttons and knobs on the top to set the frequency, pulse width and output voltage. On the back, there are power input and voltage output terminals.

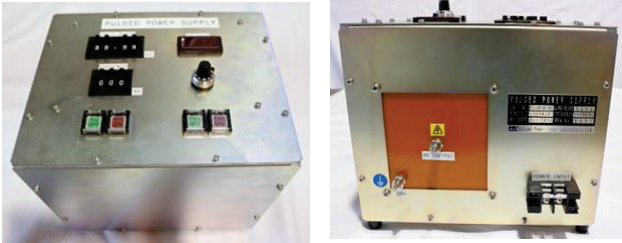


Figure 3: Pulsed power supply. 10pF is connected to the load.

Figure 4 shows the wiring and measurement device when 10pF was connected to the load and the output voltage waveform was measured, and the measured conditions are shown in Table 2. The output voltage waveform under this condition is shown in Fig. 5.

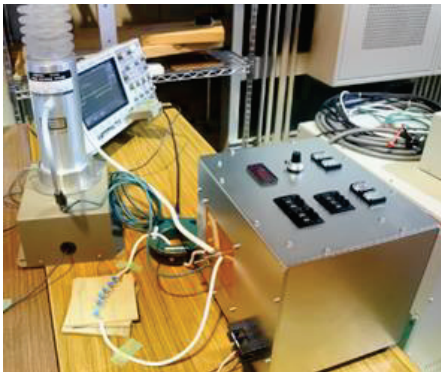


Figure 4: Measurement circuit.

Table 2: Test Conditions

Parameters	Conditions
Load Capacity	10pF
10%-90% Rise Time	66ns
10%-90% Fall Time	67ns
Voltage	8000V
Pulse Width	100μs
Frequency	1000Hz

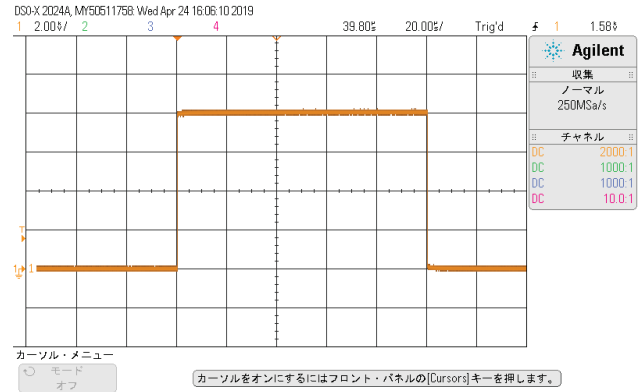


Figure 5: Output voltage waveform.

From Figure 5, it can be confirmed that the waveform is output according to the set value. The rise and fall times were 66ns and 67ns, respectively. This is well below the target value of 100ns.

#### IV. Conclusions

We have developed a power supply for capacitive loads with an output voltage of 8 kV, a square wave output, and a rise and fall time of 100 ns or less, meeting our target specifications.

The target specifications have been achieved, but there are some areas where improvements can be made. For one thing, the assumed load capacity is too small. By making it possible to output at a higher capacity, it will become a power supply that can be used for further applications. Next is the output voltage. In order to move an electron gun or an electrostatic kicker, a voltage of several tens to several hundred kV is required. In order to run these devices, higher voltages at higher outputs are desired. Also, since this power supply does not have an external trigger input or internal trigger monitor, we think that adding those terminals and functions would make it easier to use.

In the future, we aim to develop a power supply that is easy to use in a wider range of applications, mainly by making the improvements mentioned above.

# Numerical study of conical terahertz emission from laser created plasma

T. Kobayashi, T. P. Otsuka and N. Yugami

Graduated School of Utsunomiya University, 7-1-2 Yoto, Utsunomiya, Tochigi 321-8585, Japan

**Abstract**—Radiation in a sub-THz range with a broad spectrum was observed in laser plasma interaction experiments. The direction of the radiation is symmetrical from 30 to 60° with respect to the laser direction, and its polarization is in the radial direction. This suggests that the radiation is generated by the radial oscillation of plasma electrons under the electric field of a laser generated immovable ion column. To explain the frequency distribution of the radiation, the radiation is emitted from the plasma column. The numerical calculation of the distribution is in good agreement with the experimental data.

**Keywords**—laser created plasma, terahertz emission, terahertz, conical structure

## I. Introduction

Since the pioneering experiments by Hamster et.al. in 1993, numerous experiments on terahertz(THz) wave generation by intense laser pulse have been reported[1,2]. Recently the THz radiation rapidly became important tool for researching atoms, molecules and biomedical tissues, organic chemical materials etc. Many applications have been proposed in imaging, security screening and chemical identifications.

Several groups have observed radially polarized THz wave from laser-created gas plasma. N. Yugami et. al. and C. D'Amico et. al. have observed a conical forward THz radiation from the plasma which is created femtosecond-laser pulse[3,4]. The radiation emits having small angle with respect to the laser direction and the angle depends on the radiation frequency.

In this report, we briefly show the THz radiation from laser created plasma experiments and the calculation for the frequency of emitted radiation by using 2D PIC(particle in cell) code.

## II. Experiments and calculations

In the experiment, we used a 10 Hz Ti:Sapphire laser beam at a wavelength of 800 nm, with a maximum energy of 100 mJ and a duration of 100 fs [full width at half maximum(FWHM)], is used for the plasma creation and its maximum intensity is on the order of  $10^{17}$  W/cm<sup>2</sup>. In order to measure the spectrum of the emitted radiation, we used five crystal detectors which has different frequency region: The sensitivity of all detectors cover between 0.1 and 0.3 THz. All of detectors were connected with a waveguide and a horn antenna. The radiation is emitted in the forward direction with respect to the laser propagation direction and uniformly emitted in the azimuthal direction. The radiation with higher frequency component is emitted with small angle.

The laser wakefield is generated after the laser propagation in the plasma. This has not only longitudinal electric field but also transverse one and both electric fields oscillate at the plasma frequency which depend on the local plasma density and attribute the radiation generation. Although the longitudinal field can emit the radiation in the transverse direction, it strongly damps due to  $\omega = \omega_p$ . On the other hand, the transverse field can emit in the forward direction with respect to the laser propagation. The electron

in the plasma can oscillate between overdense and underdense region, because the plasma density decrease in the radial direction due to radial change of the laser intensity. The radiation can propagate in the plasma when the electrons travel in the underdense region. We calculate the radiation in the THz frequency region after the intense laser propagation in the plasma using 2-dimensional particle in cell(PIC) code[5]. Figure 1 shows the frequency distribution as the function of the angle with respect to the laser propagation. Higher frequency component has the small angle between 2 and 3 THz and lower component under 1 THz is with wide angle. The radiation frequency is not continuous. This indicates the radiation strongly emits at the region where the plasma density is changed in the radial direction ( $dn/dr$ ).

In conclusion, the radiation by the interaction between laser and plasma can be explained the radial component of laser wakefield.

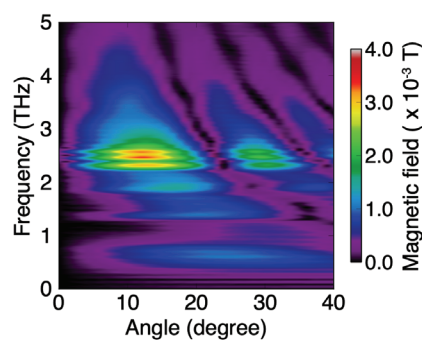


Fig. 1 Frequency distribution of radiation

## References

- [1] H. Hamster, A. Sullivan, S. Gordon, W. White, R. W. Falcone, Phys. Rev. Lett. **71** 2725, (1993).
- [2] H.-C. Wu, J. Meyer-ter-Vehn, H. Ruhl, and Z.-M. Sheng, Phys. Rev. E **83** 036407 (2011).
- [3] N. Yugami, K. Ninomiya, K. Kobayashi and H. Noda, Jpn. J. Appl. Phys. **45** L1051(2006).
- [4] C. D'Amico, A. Houard, M. Franco, B. Prade, A. Mysyrowicz, A. Couairon and V. T. Tikhonchuk, Phys. Rev. Lett. **98** 235002 (2007).
- [5] Y. Sentoku and A. J. Kemp, J. Comput. Phys. **227**, 6846 (2008).

# Experiments of forward THz emission from femtosecond laser created plasma with applied transverse electric field

T. Fukuda, T. P. Otsuka and N. Yugami

Graduated School of Utsunomiya University, 7-1-2 Yoto, Utsunomiya, Tochigi 321-8585, Japan

**Abstract**—The radiation from laser created plasma with applied electric field is studied numerically and experimentally. We experimentally observed short terahertz radiation with frequency of 0.2 THz forward direction in air using THz-TDS system. The 2D PIC simulation shows that the radiation frequency is inversely proportional to the plasma diameter and is good agreement with experimental data.

**Keywords**—laser created plasma, terahertz emission, terahertz applied electric field

## I. Introduction

Since the pioneering experiments by Hamster in 1993, numerous experiments on terahertz (THz) wave generation by intense laser pulse have been reported[1]. Recently the THz radiation rapidly became important tool for researching atoms, molecules and biomedical tissues, organic chemical materials etc. Many applications have been proposed in imaging, security screening and chemical identifications.

In this report, we show that the THz radiation from laser created plasma with the transverse electric field. The radiation is emitted in the forward direction with the linear polarization which is parallel to the electric field. The radiation power is proportional to the square of applied electric field. Simple analytic model for the radiation is given. The mode describes the electron motion under the decayed electric field in the plasma due to Debye shielding. The peak radiation frequency is determined by the plasma diameter.

## II. Experiments

The laser which creates an ionization front is a Ti:sapphire chirped-pulse-amplification laser system. A central wavelength of the laser is 800 nm with maximum energy of 40 mJ, with 120 fs pulse duration (full width at half maximum: FWHM) at 10 Hz repetition rate. The laser light was focused in the gas and its focal diameter was 100  $\mu\text{m}$  using a plano-convex lens with focal length of 800 mm and the maximum intensity of laser light was estimated to be  $1.0 \times 10^{17} \text{ W/cm}^2$ . A static electric field was applied to the focal region along the  $y$  direction (perpendicular to the laser axis) by two copper plate electrodes. The electrodes length was 1 cm and were biased with a pulsed power supply up to 15.0 kV with the duration of 200 ns (FWHM). The maximum electric field  $E_0$  at the center of the gap was estimated to be 15 kV/cm. The working gas was nitrogen and its pressure was from 30 to  $1.0 \times 10^5$  Pa, i.e. atmosphere pressure. The emitted radiation was detected by several crystal detectors which had responses between 0.09 and 0.5 THz. To detect temporal evolution of the electric field of THz radiation, we used the single-shot THz-TDS system which is based on the EO sampling using multiple laser beamlets as the probe beam by creating an echelon mirror[2]. The maximum time resolution was 100 fs. This enables us to obtain the spectral information by Fourier transforming the THz waveform.

Figure 1 shows the temporal waveform (normalized) of radiation at 10 and  $10^5$  Pa gas pressure detected by the THz-TDS and their Fourier transformation. At both experiments, strong half cycle pulse can be seen between 5.5 and 7.5 ps. This indicates that the radiation is emitted the one-way current. The peak frequency of the radiation is 0.2 THz with 0.3 THz spectral width. The laser pulse propagated at speed of light in the gas with creating ionization front. The electrons are born with zero velocity at the surface and are accelerated by the external electric field in  $y$  direction. The electric field in the plasma is strongly decayed, i.e. Debye shielding, with the time scale of plasma frequency  $\omega_p$ . The electric field is given as  $E(t) = E_{ext} \exp(-\omega_p t)$  where  $E_{ext}$  is the external static electric field. The electron velocity is calculated by the equation of motion, here the collisional frequency is neglected in this time scale and the electron current ( $J$ ) is proportional to the electric field. This current is the source of radiation.

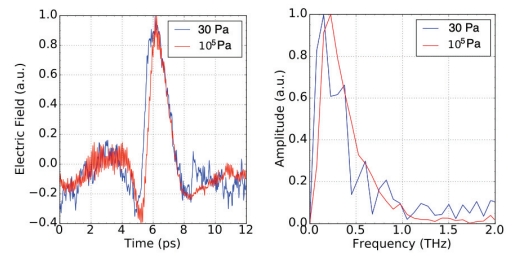


**Fig.1** The waveform of THz radiation at the gas pressure 30 Pa and  $10^5$  Pa (left) and their spectrum by Fourier transformation (right). Strong half cycle pulse can be seen between 5.5 and 7.5 ps. The peak frequency is 0.2 THz for both gas pressure. The radiation is single cycle due to the burst current at the front surface of ionization front.

## References

- [1] H. Hamster, A. Sullivan, S. Gordon, W. White, R. W. Falcone, Phys. Rev. Lett. **71** 2725, (1993).
- [2] J. Zhang, Z. Jin, S. Wakamatsu, T. Hosokai, N. Yugami, and R. Kodama, Rev. Sci. Instrum. **87** 066101 (2016).

# **K $\alpha$ spectra of medium-Z plasma dominated by M-shell multiple-ionization by an ion beam**

Yuki Ikeda, Takayuki Okui, and Tohru Kawamura

*Department of Physics, School of Science, Tokyo Institute of Technology*

## **ABSTRACT**

K $\alpha$  spectroscopy is useful as one of techniques for estimating temperature of plasma generated by an ion beam. Since the ion beam has large kinetic energy, it is easy to ionize electrons in the K-shell. However, during irradiation of the beam, electrons in the outer shell can be also ionized. This phenomenon is called a multiple-ionization process. In this study, spectral deformation of K $\alpha$  spectra caused by multiple-ionization is clarified under CRE conditions.

## **Keywords**

K $\alpha$  spectroscopy, heavy ion beam, multiple-ionization, population kinetics, CRE

## **1. Introduction**

K $\alpha$  spectroscopy is effective as one of techniques for estimating temperature of plasma generated by an ion beam. K $\alpha$  ray is emitted when electrons in the K-shell are ionized. It has also been confirmed that K $\alpha$  spectrum shifts to a higher energy side as the degree of ionization of a target ion increases [1]. Since the degree of ionization depends on plasma temperature, it can be estimated with the use of K $\alpha$  signature.

Not only K-shell electrons but also outer ones are simultaneously ionized by an ion impact. This is called a multiple-ionization process. If the influence of the multiple-ionization process cannot be ignored, the temperature of target plasma is deduced to be higher without consideration of the processes. This is because the degree of ionization is determined by only single

electron processes to numerically produce a desired K $\alpha$  spectrum. In this study, we focus on the conditions of plasma and incident ion beam relevant to K $\alpha$  radiation affected by the multiple-ionization.

## **2. Population Kinetics and Spectral Synthesis**

As a result of ion beam injection into plasma, K- and/or L-shell vacant states are mainly created. In order to estimate net K $\alpha$  emission, non-radiative processes, such as KLL-, KLM-, KMM- and LMM-Auger transitions, are considered in population kinetics calculation. Solving a corresponding rate equation under a CRE condition, population of each atomic state can be obtained. In the population

calculation, the K- and L-shell ionization cross sections by ion impacts published by Rice *et al.* [2], and Hansteen *et al.* [3] are adopted, respectively. In the calculation of the K $\alpha$  spectra, the spectral profiles are convolved by electron impact broadening with a semi-classical expression [4], natural and Doppler broadenings assuming that ion temperature is equal to electron temperature. Calculation of K $\alpha$ -lines was performed with the use of GRASP92 and RATIP codes [5,6] which are based on a multi-configuration Dirac-Fock (MCDF) method.

### 3. Model Descriptions of Multiple-ionization Cross Sections

Assuming that the multiple-ionization is simultaneous independent single ionization of binding electrons, the total probability can be represented by the product of the independent ionization probability of each shell. If the ionization probability in the same shell is identical, a cross section for ionizing a single K-shell electron,  $n_L$  L-shell electrons,  $n_M$  M-shell electrons, ... and  $n_J$  J-shell electrons has a binomial distribution [7]:

$$\begin{aligned} \sigma_{1K,n_L,n_M,n_J} = & \sigma_K \binom{N_L}{n_L} P_L^{n_L} (1 - P_L)^{N_L - n_L} \\ & \times \binom{N_M}{n_M} P_M^{n_M} (1 - P_M)^{N_M - n_M} \\ & \times \dots \binom{N_J}{n_J} P_J^{n_J} (1 - P_J)^{N_J - n_J}, \quad (1) \end{aligned}$$

where  $\sigma_K$  represents a cross section of K-shell ionization.  $N_L, N_M, \dots, N_J$  and  $P_L, P_M, \dots, P_J$  are number of L-, M-, ... , J-shell electrons and single L-, M-, ... , J-shell ionization probability, respectively.

In this study, the multiple-ionization for a single K-

shell electron and up to seven M-shell electrons are considered in the calculation. Then, the following Eq.(2) gives the corresponding KM multiple-ionization cross section:

$$\sigma_{K,nM} = \sigma_K \binom{N_M}{n} P_M^n (1 - P_M)^{N_M - n}. \quad (2)$$

### 4. Calculation Results and Discussion

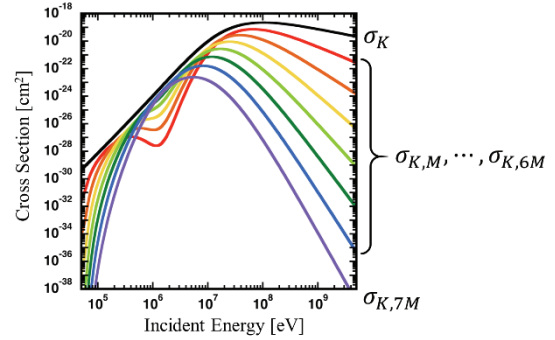


Fig.1 Multiple-ionization cross sections of a Cl atom collided with a C<sup>6+</sup> ion.  $\sigma_K$  indicates the cross section of the K-shell ionization.  $\sigma_{K,M-7M}$  indicates those of the multiple-ionization for a single K-shell and 1~7 M-shell electrons.

Figure 1 shows the multiple-ionization cross sections of a Cl atom. In the previous work [8], the incident energy was 30 MeV, and the multiple-ionization processes were neglected due to small number density of the incident ion beam compared with surrounding plasma free-electrons. It is found that almost no spectral shift can be seen in Fig.2(a). However, with the incident energy of 5 MeV, slight spectral shift due to the multiple-ionization was observed as shown in Fig.2(b). This is due to, as shown in Fig.1, the several curves of the cross sections concentrate around 5 MeV, occurring more frequent multiple-ionization.

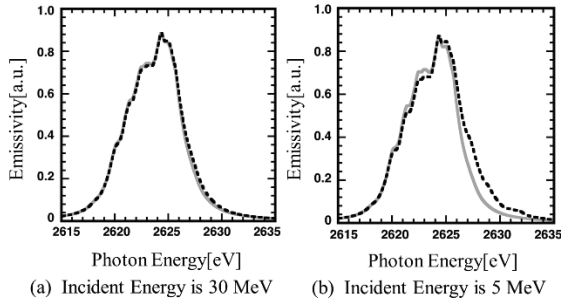


Fig.2 Calculated Cl-K $\alpha$  from C<sub>2</sub>H<sub>5</sub>Cl plasma at ion density  $\rho_i = 8.1 \times 10^{22} \text{ cm}^{-3}$  and electron temperature  $T_e = 10 \text{ eV}$ . C<sup>6+</sup> beam current is 3 kA/cm<sup>2</sup>. Solid line: without multiple-ionization, dashed line: with multiple-ionization.

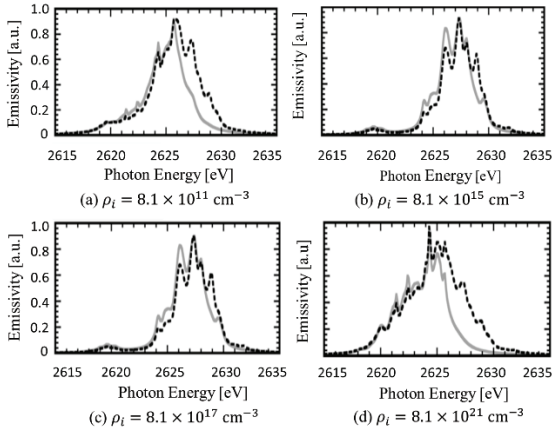


Fig.3 Calculated K $\alpha$  spectra of Cl plasma at electron temperature  $T_e = 5 \text{ eV}$  and plasma densities are (a)  $\rho_i = 8.1 \times 10^{11} \text{ cm}^{-3}$ , (b)  $\rho_i = 8.1 \times 10^{15} \text{ cm}^{-3}$ , (c)  $\rho_i = 8.1 \times 10^{17} \text{ cm}^{-3}$ , and (d)  $\rho_i = 8.1 \times 10^{21} \text{ cm}^{-3}$ . C<sup>6+</sup> beam current is 300 mA/cm<sup>2</sup>, and incident beam energy is 5 MeV. Solid line: without multiple-ionization, dashed line: with multiple-ionization.

Figure 3 shows the density dependence of spectral blue-shift caused by the multiple-ionization. With the beam density close to that of Cl plasma, the contribution of the multiple-ionization seems to be

enhanced. However, clear dependence on the plasma density cannot be seen. This is because, even if at the same temperature, main charge state of the K $\alpha$  lines is different depending on the plasma density, and it is hard to clearly see the spectral shift due to the multiple-ionization. In addition, M-shell electrons can be easily ionized at low plasma temperature and the spectral shift of the K $\alpha$  lines is intrinsically small. In this study, since only KM multiple-ionization is included, KL multiple-ionization may be necessary to see clear dependence of spectral shift on the plasma density. As shown in Ref. [1], K $\alpha$  lines with partially ionized L-shell show large blue-shift with increase in the charge states of K $\alpha$  lines.

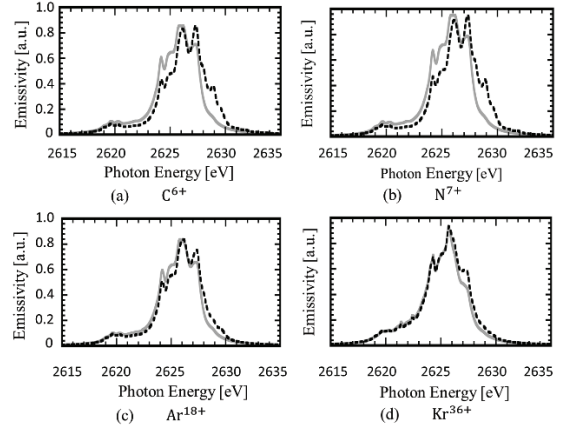


Fig. 4 Calculated K $\alpha$  spectra from Cl plasma at ion density  $\rho_i = 8.1 \times 10^{13} \text{ cm}^{-3}$  and electron temperature  $T_e = 5 \text{ eV}$ . The incident ion species are (a) C<sup>6+</sup>, (b) N<sup>7+</sup>, (c) Ar<sup>18</sup>, and (d) Kr<sup>36+</sup>, respectively. Solid line: without multiple-ionization, dashed line: with multiple-ionization.

Figure 4 shows the dependence of incident ion species for the multiple-ionization. In Ref. [7], the

ionization probability is proportional to the square of projectile charge, expecting that spectral blue-shift due to the multiple-ionization is enhanced. However, as results, such clear dependence cannot be seen in the figure. In the calculation, incident beam energies are selected to get large multiple-ionization probabilities.

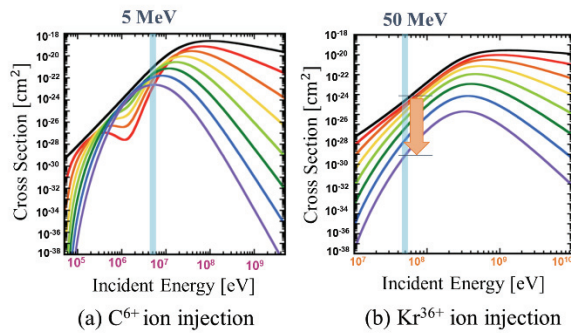


Fig.5 Multiple-ionization cross sections of a Cl atom with (a)  $C^{6+}$  ion injection, (b)  $Kr^{36+}$  ion injection. Each line represents the multiple-ionization cross section for a single K-shell and possible M-shell electrons. The incident ion energies are selected to be 5 MeV and 50 MeV, respectively.

Figure 5 gives the multiple-ionization cross sections for  $C^{6+}$ - and  $Kr^{36+}$ -beams. Comparison between the two cases indicates that the curves of cross sections for a  $Kr^{36+}$ -beam has wider intervals, resulting in small multiple-ionization probabilities.

## 5. Conclusions

In this paper, the dependence of beam and plasma conditions for multiple-ionization were briefly discussed. Although spectral shift due to the multiple-ionization was observed, the plasma density dependence was not clearly seen. It is expected that the KL multiple-ionization may give distinct spectral blue-shift, and the corresponding process is now being

considered in the calculation. The results will be reported somewhere.

## References

- [1] T. Kawamura *et al.*, *J. Quant. Spectrosc. Radiat. Trans.* **81**, 237 (2003).
- [2] R. Rice, G. Basbas, and F. D. McDaniel, *At. Data Nucl. Data Tables.* **20**, 503 (1977).
- [3] J. M. Hansteen, O. M. Johnsen, and L. Kocbach, *At. Data Nucl. Data Tables.* **15**, 305 (1975).
- [4] H. Griem, M. Blaha, and P. C. Kepple, *Phys. Rev. A.* **41**, 5600 (1990).
- [5] F.A.Parpia, C. F. Fischer, and I. P. Grant, *Comput. Phys. Commun.* **94**, 249 (1996).
- [6] S. Fritzsche, *J. Electr. Spec. Rel. Phenom.* **114-116**, 1155 (2001).
- [7] J. H. McGuire and P. Richard, *Phys. Rev. A* **8**, 1374 (1973).
- [8] T. Kawamura, K. Horioka and F. Koike, *Laser Part. Beams* **29**, 135 (2011).

# Study on Electrode Structure of Reflex Triode Virtual Cathode Oscillator for High Power Microwave Generation

Ryotaro Haruki, Ryota Tanaka, and Hiroaki Ito

*University of Toyama, Gofuku 3190, Toyama Toyama 930-8555, Japan*

## ABSTRACT

One of the candidates for the high-power microwave source is a virtual cathode oscillator. The virtual cathode oscillator has a simple structure, it can generate GW-class microwaves, and has the advantage that the frequency can be easily adjusted. It is expected to be applied to wireless power transmission, plasma heating, and accelerators. However, the large size of the device and the extremely low conversion efficiency of 10% or less are mentioned as disadvantages, and research for improving the conversion efficiency has been conducted around the world. In this study, the microwave power was evaluated using a calorimeter in a reflective triode virtual cathode oscillator. Attention was paid to the cathode material, which is considered to greatly affect the generation of electron beams. Aluminum, velvet, and carbon fiber were used as the electrode materials. Furthermore, a new double anode Vircator was developed to improve the microwave conversion efficiency, and its evaluation was performed.

## Keywords

High power microwave, Reflective triode virtual cathode oscillator, double anode Vircator

## 1. Introduction

Microwave refers to electromagnetic waves having a frequency between 300 MHz and 300 GHz. Microwaves with more than 100 MW of power are called high power microwaves (HPM). High power microwaves are expected to be applied to wireless power transmission, plasma heating, and accelerators. One of the candidates for the high-power microwave source is a virtual cathode oscillator (Vircator). The virtual cathode oscillator has a simple structure and the ability to generate GW-class microwaves, and its easy frequency control. However, it has the large system and the extremely low microwave conversion efficiency of 10%. Thus, many studies to improve the conversion efficiency have been conducted worldwide [1].

In this study, we evaluated the effect of the electrode materials on the microwave power and conversion efficiency using a calorimeter in a reflective triode virtual cathode oscillator. In order

to improve the microwave conversion efficiency, we also developed a new double anode Vircator and evaluated the power and conversion efficiency.

## 2. Principle of Vircator

Figure 1 shows the operating principle of the virtual cathode oscillator. When a positive high voltage pulse is applied to the meshed anode, electrons are extracted from the cathode surface due to electric field concentration. These electrons pass through the meshed anode and enter the drift space. At this time, when the electron beam exceeds the space charge limiting current, a virtual cathode is formed. The electron beam is reflected by the virtual cathode and moves back and forth between the cathode and the virtual cathode. Microwaves are generated by the oscillating motion of the electrons. The virtual cathode is an unstable area maintained by a subsequent electron beam, microwaves are also generated when the virtual cathode itself oscillates temporally and

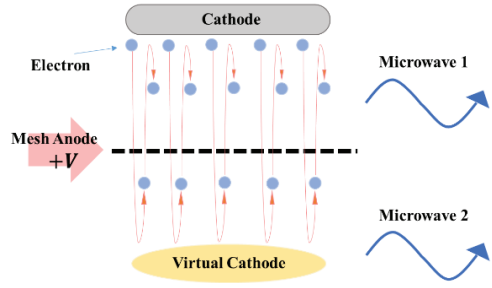


Fig.1 Principle of Vircator

spatially. As described above, the virtual cathode oscillator has two microwave sources.

### 3. Experimental Setup

Figure 2 shows the experimental setup. The virtual cathode oscillator consists of a cathode and an anode. As the cathode, an aluminum electrode having a diameter of 46 mm and 60 mm was used. Velvet and carbon fiber were used as the cathode materials. A stainless mesh with an aperture ratio of 64.5% was used for the anode. The diode voltage  $V_d$  was measured by a capacitive voltage divider installed in the Marx generator. The diode current  $I_d$  was measured using a Rogowski coil installed at the connection between the Marx generator and the vacuum vessel. The emitted microwave was measured using a coaxial waveguide converter installed 120 cm behind the output window. The calorimeter used in this

experiment is composed of a carbon plate (100 mm in diameter and 15 mm in thickness) as a microwave absorber and an alumel–chromel thermocouple. The carbon plate is placed in a vacuum vessel and rises in temperature when absorbing microwaves. The temperature change is measured by the thermocouple. Here, assuming that the temperature change of the carbon plate is  $\Delta T$ , the heat quantity  $Q$  is given by the following equation.

$$Q = A\rho h\Delta T$$

Here,  $A$  is the volume of the carbon plate,  $\rho$  is the density, and  $h$  is the specific heat. It is considered that the reflective triode virtual cathode oscillator emits microwaves in the entire radial direction. The total heat of the microwave passed through the spherical area  $S$  as shown in Fig.3 is represented by  $Q_{total}$ . The  $Q_{total}$  is calculated from  $Q$ . Thus, the microwave power  $P$  is

$$P = \frac{Q_{total}}{\tau_{mw}}$$

where  $\tau_{mw}$  is the pulse duration of the microwave. The microwave conversion efficiency  $\eta$  is defined as

$$\eta = \frac{Q_{total}}{J_d}$$

where  $J_d$  is the input energy of the Marx generator.

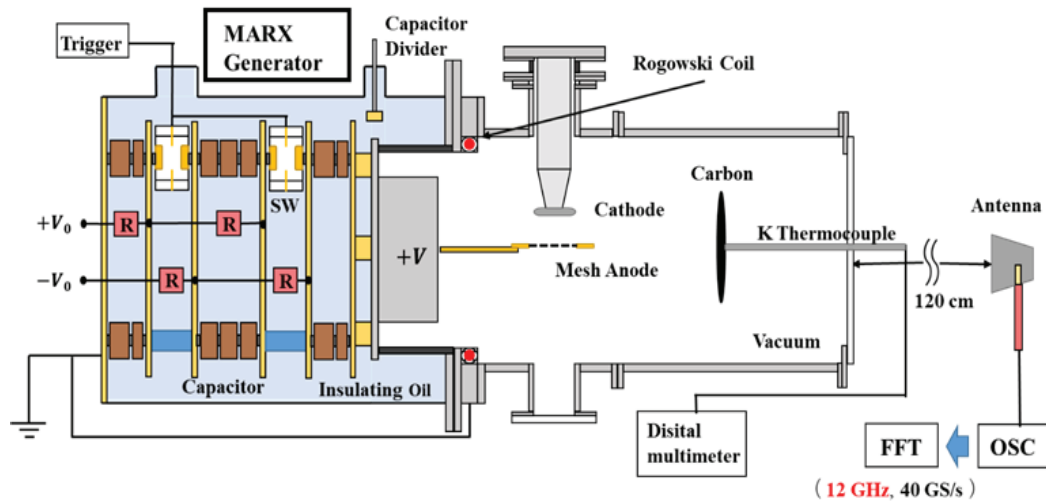


Fig2. Experimental Setup

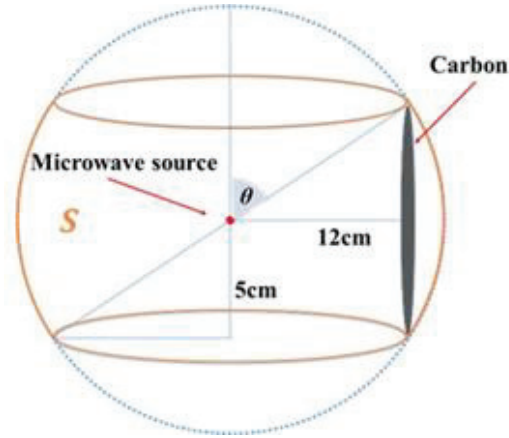


Fig.3 Microwave radiation area

## 4. Experimental Results

### 4.1 Microwave output with aluminum electrode

First, experiments on an aluminum electrode were performed. Figure 4 shows typical output waveforms. The diode voltage  $V_d$  is 180 kV (200 ns) and the diode current  $I_d$  is 15 kA (250 ns). Figure 5 shows the dependence of AKGAP on the electric field and frequency of emitted microwaves. The pulse width of microwave increases with the increase of AKGAP. The frequency ranges widely from 4 to 8 GHz. The oscillation frequency tends

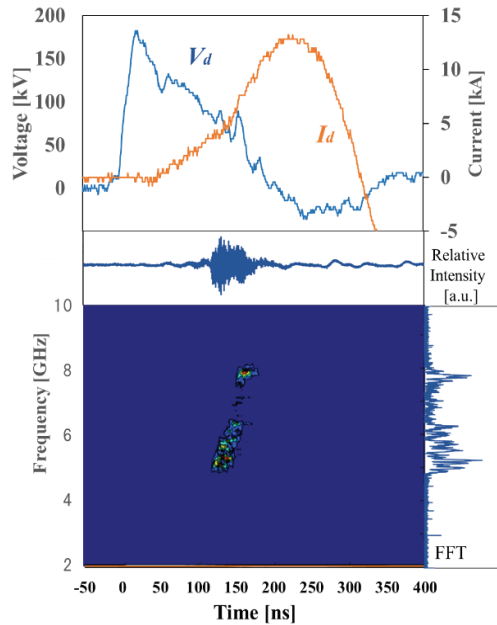


Fig.4 Typical waveforms with aluminum electrode

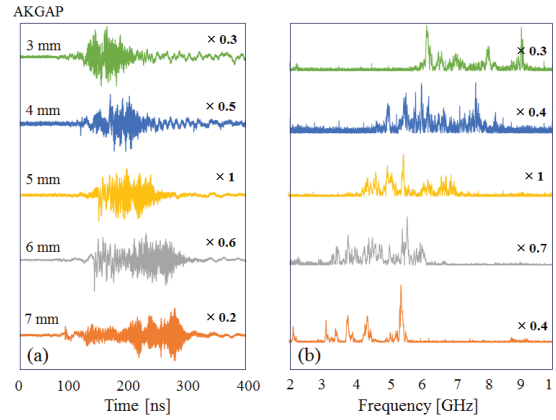


Fig.5 Dependence of AKGAP on (a) electric field and (b) FFT of emitted microwave

to shift down with the increase of AKGAP and can be easily controlled by AKGAP, which is an advantage of the virtual cathode oscillator. However, with aluminum electrodes, the output and frequency band of microwaves changed for each shot.

### 4.2 Material dependence of microwave power

Cathode materials have a significant effect on electron emission. Therefore, velvet and carbon fiber were newly prepared as the electrode materials. Velvet and carbon fiber have been reported to improve electron beam quality, microwave power and conversion efficiency [2].

Figure 6 shows typical output waveforms with the carbon fiber electrode. With the velvet and carbon fiber electrodes, the pulse width of diode voltage, diode current, and microwave become longer than with the aluminum electrode. Although the output and frequency of microwaves changed under the same conditions with the aluminum electrode, shot stability was greatly improved with the velvet and carbon fiber electrodes. In addition, with the velvet electrode the monochromaticity of the frequency was improved. On the other hand, using the carbon fiber the oscillation frequency tends to be monochromatic under some conditions. The current also rises earlier, since the discharge is more likely to occur at lower voltage due to the electric field concentration at the tip of fiber.

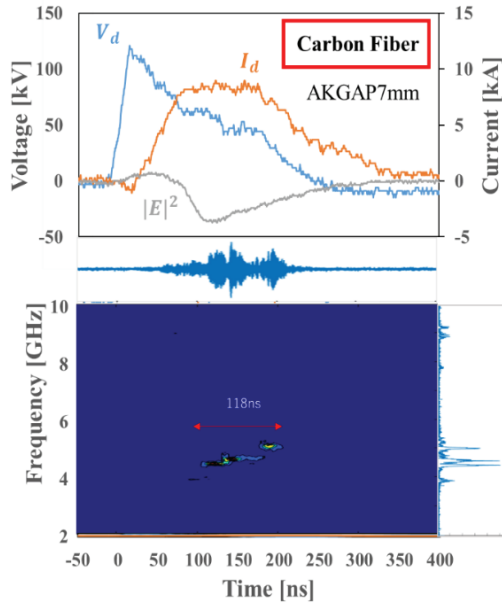


Fig.6 Typical waveforms and time-dependent frequency analysis with carbon fiber

Figure 7 shows the dependence of the electrode materials on the microwave conversion efficiency. Here, the electrode diameter was 46 mm and 60 mm, and the electrode materials were aluminum, velvet, and carbon fiber. The maximum microwave power of 180 MW and the conversion efficiency of 9 % were obtained when the diameter of the electrode was 46 mm and the AKGAP was 6 mm with the carbon fiber electrode.

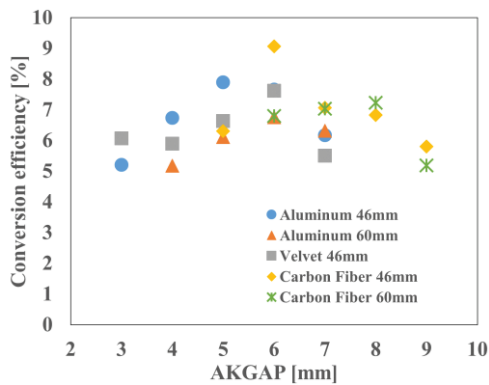


Fig.7 Material dependence of conversion efficiency

### 4.3 Evaluation of double anode Vircator

We have developed the double anode Vircator using two mesh anodes to improve the microwave

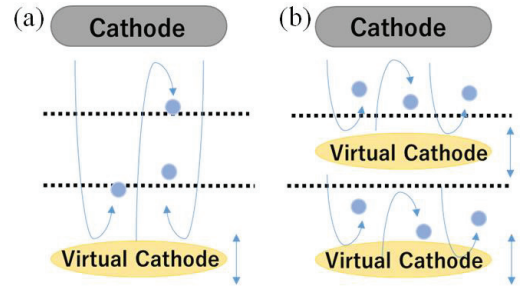


Fig.8 Principle of double anode vircator

conversion efficiency. The carbon fiber was used for the cathode material, since the carbon fiber electrode had the largest microwave power. Figure 8 shows two operation modes of the double anode Vircator. (a) The frequencies due to the electron reflexing in the potential well and to the oscillation of the virtual cathode are originally not equal. The introduction of another anode allows the frequency due to electron reflexing to independently adjust and to tune the latter one [3]. (b) The virtual cathode is formed behind the first mesh anode and reflects part of the electron. If the transmitted electron beam current is high enough, an oscillating virtual cathode builds up beyond the second anode and contributes to microwave generation [4]. This mode works like the multimode vircator. There are two microwave sources due to oscillating virtual cathode itself and three ones due to electron reflection. Therefore, the double anode vircator can improve the microwave conversion efficiency.

Figure 9 shows typical output waveforms in the double anode vircator. The most distinctive feature of the double anode vircator is that the microwave with multiple strong frequencies radiates. In particular, the frequencies are 2 GHz, 5 GHz and 7 GHz. This result indicates that the double anode vircator operates in the mode (b) which two virtual cathodes are formed. Although there are five microwave sources in the mode (b), it is considered that the microwaves are strongly emitted from some sources. When the cathode-anode gap is short compared to the distance between two anodes, the effect of the second anode little works, which

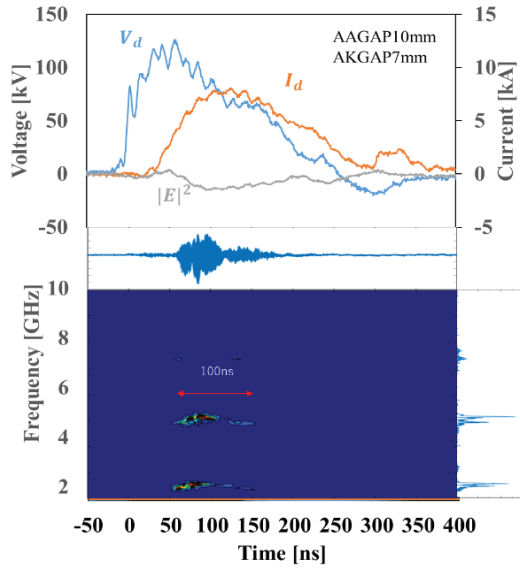


Fig.9 Typical waveforms and time-dependent frequency analysis of double anode vircator

operates like the conventional vircator.

Figure 10 shows the effect of AKGAP on the microwave conversion efficiency in the double anode vircator, where the distance between the anodes is 10 mm. The conversion efficiency is slightly higher than with a single anode. The conventional vircator with the carbon fiber electrode has the maximum conversion efficiency of 9 % at AKGAP 6 mm (see Fig. 7), while the double anode vircator has the efficiency of 6 %.

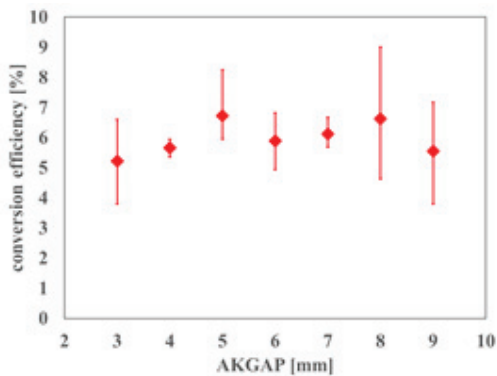


Fig.10 Dependence of AKGAP on conversion efficiency in double anode vircator

## 5. Conclusions

The dependence of electrode materials on the microwave output in the reflective triode virtual cathode oscillator was investigated. A maximum microwave output of 180 MW and a maximum conversion efficiency of 9 % were obtained for the carbon fiber electrode. We have developed a new double anode Vircator and conducted experiments. The microwave output with multiple frequency was obtained, but the microwave conversion efficiency was slightly reduced. Research on the double anode vircator need to be conducted to clarify many unclear points.

## Acknowledgement

This work was partially supported by JSPS KAKENHI Grant Number JP19H02126.

## References

- [1] Donald J. Sullivan, "High Power Microwave Generation from a Virtual Cathode Oscillator (Vircator)", IEEE Trans. Plasma Sci., Vol.NS-30, pp. 3426 - 3428 (1983).
- [2] Evan Rocha, *et al.*, "Evaluating the Performance of a Carbon-Epoxy Capillary Cathode and Carbon Fiber Cathode in a Sealed-Tube Vircator Under UHV Conditions ", IEEE Trans. Plasma Sci., Vol.43, pp. 2670 - 2675 (2015).
- [3] J. Benford, J. Swegle, and E. Schamiloglu, High Power Microwaves, 3rd ed. (CRC Press, 2016).
- [4] S. Champeaux, *et al.*, "Improved Design of a Multistage Axial Vircator with Reflectors for Enhanced Performances", IEEE Trans. Plasma Sci., Vol.44, pp.31-38 (2016).

# Energy evaluation of pulsed heavy ion beams in bipolar pulsed accelerator

Masashi Terada, Haruyasu Ishida, and Hiroaki Ito

*University of Toyama, 3190 Gofuku, Toyama 930-8555, Japan*

## ABSTRACT

We have developed a prototype of a bipolar pulse accelerator (BPA) that can generate a pulsed ion beam with high purity that is higher than conventional ion diodes. The BPA is operated with the bipolar pulse voltage and is a two-stage electrostatic accelerator. It was found that the ion beam was successfully accelerated in the 1st and 2nd gaps by applying the bipolar pulsed voltage. We used a Thomson parabola analyzer to evaluate the energy and ion species contained in the accelerated ion beam. The Thomson parabola analyzer is a device that deflects accelerated charged particles with the electric and magnetic fields, and the track pattern corresponding to ion species and energy is described on a solid track detector CR-39 installed as a detector. By comparing the track pattern obtained in the experiment and the track pattern calculated by the theory, it is possible to specify the energy and ion species. In this study, we report the results of BPA demonstration experiments using a Thomson parabola analyzer.

## Keywords

Pulsed heavy ion beam, Bipolar pulse accelerator, Pulsed ion implantation, Thomson parabola analyzer

## 1. Introduction

The high intensity pulsed ion beam refers to an ion beam with an energy of  $>100$  keV, pulse width  $<1$   $\mu$ s, and ion current density  $>100$  A/cm<sup>2</sup>, which generated by using high voltage and high power pulse generation technology called pulsed power technology. This high-intensity pulsed ion beam is applied to surface treatment techniques such as ion implantation and annealing because the energy given to materials by a beam irradiation is very large [1-4].

In recent years, in the semiconductor device industry, SiC (silicon carbide), which is one of the next-generation semiconductor materials of high frequency, low loss, and high efficiency, has attracted attention as a material to replace silicon. Localized doping techniques are essential for manufacturing SiC devices. Generally, local doping techniques include diffusion and ion implantation, but since the diffusion coefficient of impurities in SiC is extremely small, doping by diffusion is difficult, and ion implantation is used. Also, after ion implantation, a high temperature annealing process at 1500 to 1800 °C is necessary for

recovery of crystal loss and activation of impurity atoms. The conventional method at such a high temperature causes several disadvantages such as the redistribution of implanted dopants and surface roughness. These problems demand novel annealing techniques that do not require high temperature.

In order to realize a new ion implantation technology named “pulsed ion beam implantation” to the next-generation semiconductor material such as SiC, we have studied the high-intensity pulsed heavy ion beam. In this study, in order to generate various ion species that work as p-type and n-type dopants, we developed a pulsed heavy ion beam generation technology with a gas puff plasma gun as the ion source. In addition, we have developed a Bipolar Pulsed Accelerator (BPA) to improve the beam purity by using a newly developed bipolar pulse generator. The ion beam was successfully accelerated in the 1st and 2nd gaps by applying the bipolar pulsed voltage. We report the experimental results on the energy evaluation of the pulsed ion beam in the bipolar pulse accelerator by a Thomson parabola analyzer.

## 2. Principle of bipolar pulse accelerator

Figure 1 shows a conceptual diagram of the acceleration principle of the BPA. The BPA is composed of an anode having a ground potential, a drift tube, and a grounded cathode. The acceleration power supply is connected to the drift tube, and a bipolar pulse  $\pm V_0$  of negative pulse (pulse width:  $\tau_p$ ) and positive pulse (pulse width:  $\tau_p$ ) is applied. When the ion beam generated by the ion source reaches the surface of the anode, a bipolar pulse voltage is applied to the drift tube. Since a negative voltage is first applied to the drift tube, ions are accelerated between the grounded anode and the drift tube (1st gap) (①). When the ion beam passes through the drift tube and the tip reaches the 2nd Gap, when the polarity of the applied voltage is reversed and a positive voltage is applied, the ions are accelerated again from the drift tube toward the grounded cathode (②).

The principle of purity improvement of the pulsed ion beam is described in Fig.2. As an example, let us consider ion acceleration when the pulsed ion beam contains the main component of nitrogen ion ( $N^+$ ), which is n type dopant of SiC, and impurity ion, hydrogen ion ( $H^+$ ) generated from moisture attached to the electrode. First, when a negative pulse of bipolar pulse voltage is applied to the drift tube, each ion is accelerated from the anode toward the drift tube at the 1st Gap, and due to the difference in speed due to the mass difference of ions, as shown in Fig.2  $H^+$  beam length is longer than  $N^+$  beam length. When  $V_0 = 200$  kV and pulse width  $\tau_p = 70$  ns, the  $N^+$  beam length is 11.6 cm and the  $H^+$  beam length is 43.3 cm. When a negative pulse is applied to the drift tube, the 1st Gap is an accelerating electric field, but since the 2nd Gap

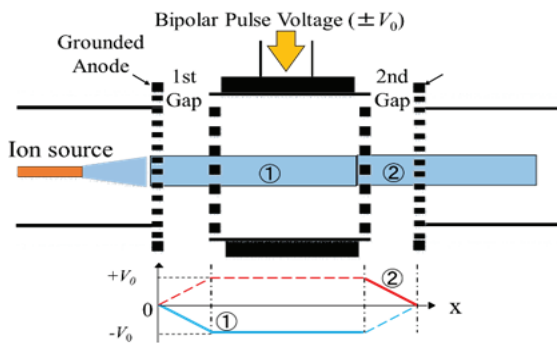


Fig. 1 Two stage acceleration mechanism of BPA

is the decelerating electric field, by designing the length of the drift tube according to the  $N^+$  beam length, 73% of the already arriving  $H^+$  beam is decelerated and energy cannot be obtained. That is, two stages of acceleration are not performed, and relative improvement in the purity of the  $N^+$  beam can be expected.

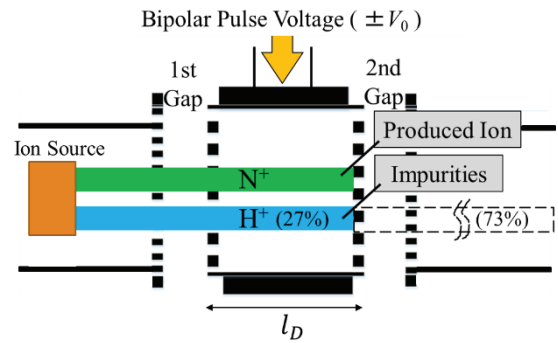


Fig. 2 Improvement of Ion Beam purity

## 3. Experimental setup

Figure. 3 shows a schematic configuration of the bipolar pulse accelerator in the present experiment. The pulse forming line (PFL) is a double coaxial structure consisting of a center conductor, an intermediate conductor, and an outer conductor, and water is used as a dielectric, and negative and positive pulse voltages are charged with a rating of  $\pm 200$  kV and a pulse width of 70 ns. After charging the intermediate conductor with the Marx generator, the bipolar pulse is generated by closing the rail gap switch filled in  $SF_6$  as insulating gas. Characteristic impedances between the center and intermediate conductors and between the intermediate and outer conductors are  $6.7 \Omega$  and  $7.6 \Omega$ , respectively.

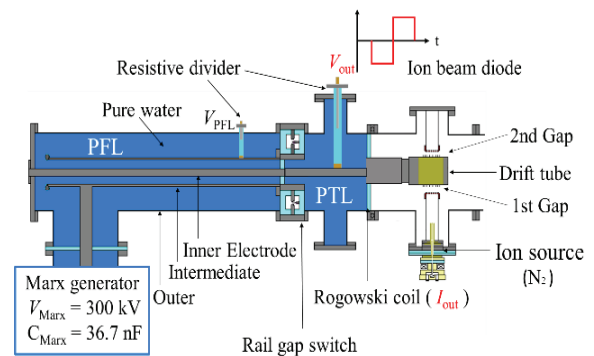


Fig. 3 Schematic configuration of BPA

#### 4. Thomson parabola analyzer

The Energy evaluation was performed using a Thomson parabola analyzer to confirm the two-stage acceleration. The Thomson parabola analyzer is an analyzer that measures the energy and ion species of the ion beam from the deflection distance by deflecting the ion beam with an electric field and a magnetic field. The deflection distances  $D_e$  and  $D_b$  due to the electric and magnetic fields are expressed in Eqs. (1) and (2), respectively.

$$D_e = \frac{ZeELl_d}{mv^2} \quad (1)$$

$$D_b = \frac{ZeBLl_d}{mv} \quad (2)$$

where  $Z$  is the charge state of the ion,  $e$  is elementary charge,  $E$  and  $B$  are the electric and magnetic field,  $L$  is the length of the electric and magnetic field,  $L_d$  is the length from the center of the electric and magnetic field area to the detector,  $m$  is the ion mass,  $v$  is the ion velocity. Combining Eqs. (1) and (2), Eq. (3) is obtained.

$$D_e = \frac{m}{Ze} \frac{EL}{(BL)^2 L_1} D_b^2 \quad (3)$$

From Eq. (3), it can be understood that the deflection distance  $D_b$  due to the magnetic field is a quadratic function of the deflection distance  $D_e$  of the electric field, and a parabola is drawn on the detector. The Thomson parabola analyzer used in the experiment is shown in Fig. 4. The Thomson parabola analyzer is composed of two pinholes with apertures of 0.3 mm and 0.14 mm spaced 4 cm apart, a permanent magnet, and a solid track detector CR-39, which is placed 5 cm behind the second pinhole. The electric and magnetic fields applied in this experiment are 800 kV/m and 0.75 T, respectively. Figure 5 shows a conceptual view of the pinhole configuration and the beam diameter on the detector CR-39. The beam diameter on the detector  $D_3$  can be obtained from Eq. (4).

$$D_3 = D_2 \left(1 + \frac{L_2}{L_1}\right) + D_1 \frac{L_2}{L_1} \quad (4)$$

where  $D_1$  and  $D_2$  are diameters of the first and second pinholes, respectively, and  $L_1$  and  $L_2$  are

distances between the two pinholes, and the second pinhole and detector, respectively. Using the experiment parameters, the beam diameter on the detector plane is  $D_3 = 0.69$  mm.

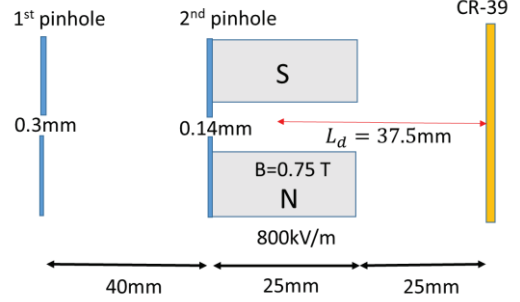


Fig. 4 Parameters of Thomson parabola analyzer used in the experiment

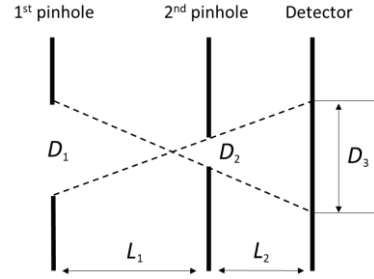


Fig. 5 Conceptual diagram of beam diameter on detector plane

#### 5. Experimental result

The experimental conditions were a charging voltage of 240 kV for the PFL, 6 kV and 15 kV for the gas puff plasma gun, and 2.5kV for the electron insulating magnetic field. Figure 6 shows typical output waveforms of PFL, PTL voltage and diode current. At this time, the maximum pulse forming line voltage was  $V_{PFL} = 261$  kV, and the maximum bipolar pulse voltage was  $V_{out} = -176$  kV and +175 kV, and the

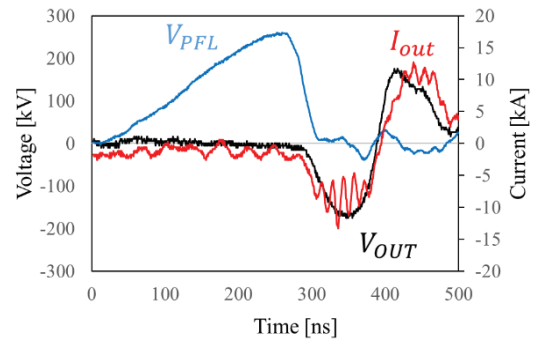


Fig. 6 Typical waveforms of 2nd acceleration

maximum diode current was  $I_{\text{out}} = -13.4 \text{ kA}$  and  $+12.7 \text{ kA}$ .

Figure 7 shows an example of the track pattern recorded on the CR-39 at the 2-stage acceleration, which is etched in a NaOH bath to make the tracks visible for 2 hours. The 7-shot ion beam was irradiated to CR-39 under the same condition. Figure 8 shows the track pattern along with the calculated trajectories of various ion species. From Figs. 7 and 8, the track patterns (a) and (b) are singly ionized nitrogen, (c) is doubly nitrogen, and (d) is hydrogen ion. It is clearly seen from the track patterns that the main component of ion beams is nitrogen, although singly and doubly ionized nitrogen ions are observed with impurity of hydrogen ions.

The energy at the center of the traces (a) and (c) can be estimated to be about  $360 \text{ keV}/Z$ , which is very close to the bipolar pulse output voltage of  $351 \text{ kV}$ . It can be seen from this result that the nitrogen ion is accelerated in two stages. However, the ion energy of the trace (a) is estimated to be  $300$  to  $605 \text{ keV}$ , which is a wide band. One of the reasons is due to the large beam diameter on the detector, which causes to the

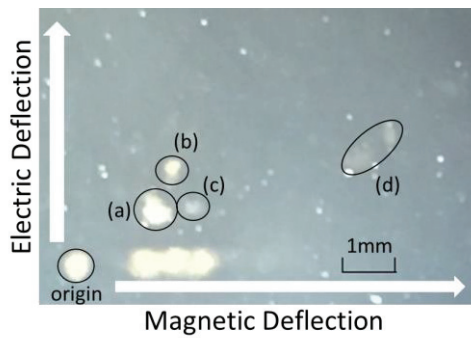


Fig. 7 Track patterns recorded on detector CR-39 at PFL charging voltage of  $240 \text{ kV}$

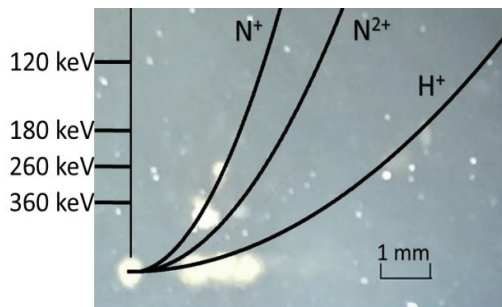


Fig. 8 Track patterns with theoretical curves

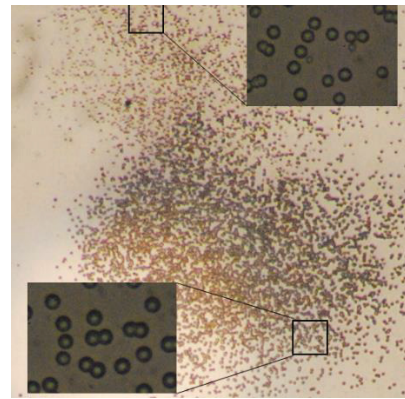


Fig. 9 Magnified image of the track (a) in Fig. 7

degradation of the energy resolution. Figure 9 show the magnified image of the track pattern (a). It can be seen from Fig. 9 that tracks with different size are contained in the high energy side of the trace (a) of singly nitrogen. These high-energy singly ionized nitrogen ions are considered to be produced by the charge exchange of doubly ionized nitrogen ions. Thus, the measured energy band broadens to high-energy side, which is larger than the bipolar pulse voltage. It is necessary to improve the resolution of the analyzer by reducing the diameter of pinhole or by increasing the applied electric field.

The track pattern (b) is on the trace of singly ionized nitrogen and the energy is estimated to be about  $260 \text{ keV}$ . The reason why the ion energy is smaller than the bipolar pulse voltage is that the condition of the bipolar pulse acceleration is not satisfied. When the nitrogen ions are accelerated at the rise of negative pulse voltage in the first gap, they do not accelerate enough in the second gap. On the other hand, the hydrogen ion (trace (d)) has the same energy of about  $260 \text{ keV}$  and the track number is much smaller than at the first gap acceleration.

Next, the same experiments were performed by changing only the charging voltage of the PFL to  $180 \text{ kV}$ . The bipolar pulse with the maximum voltage of  $V_{\text{out}} = -138 \text{ kV}$  and  $+127 \text{ kV}$ , and maximum diode current of  $I_{\text{out}} = -10.7 \text{ kA}$  and  $+9.3 \text{ kA}$  were obtained. The track patterns obtained by 7-shot irradiation is shown in Fig. 10. The photograph with the theoretical curves is shown in Fig. 11. The singly ionized nitrogen and hydrogen ions were detected. The

energy of about 260 keV was obtained for both nitrogen and hydrogen ions. This value almost agrees with the total of 265 keV of the bipolar pulse voltage, and it was found that the ion beam is accelerated by two stages.

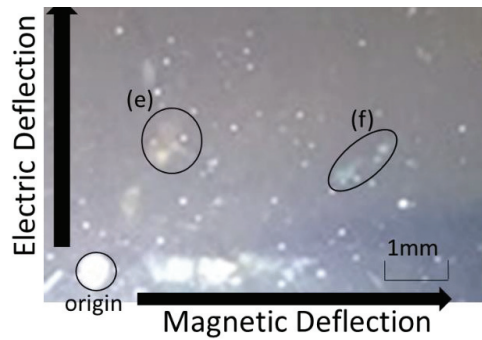


Fig. 10 Track patterns recorded on detector CR-39 at PFL charging voltage of 180 kV charge

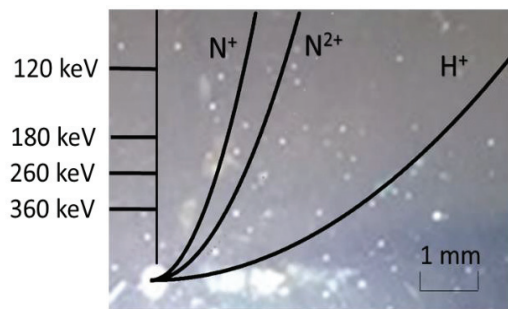


Fig. 11 Track patterns with theoretical curves

## 6. Conclusions

A two-stage acceleration experiment of the ion beam in a bipolar pulse accelerator was performed. The ion species and energy of the pulsed ion beam were evaluated using a Thomson parabola analyzer. By comparing the track pattern obtained in the experiment with the theoretical parabola, it was found that the ion beam contained singly, doubly ionized nitrogen ions and hydrogen ion. The nitrogen ion with an energy of about 360 keV/Z was obtained by the two-stage acceleration of the bipolar pulse accelerator. On the other hand, hydrogen ions were not sufficiently accelerated by two stages and removed, to improve the beam purity when the output voltage of the Marx generator was 240 kV. However, Thomson parabola analyzer used in this research has some problems that the track pattern with different ion species overlaps at

the high-energy end of the traces. Thus, it is necessary to improve the energy resolution. We need to evaluate the improvement of the beam purity of the pulsed ion beam by the two-stage acceleration.

## Acknowledgement

This work was supported by JSPS KAKENHI Grant Number JP19H02126.

## References

- [1] K. Yatsui *et al.* : "Applications of intense pulsed ion beam to materials science", *Phys. Plasma*, Vol.1, No.5, pp.1730-1737 (1994)
- [2] H. Akamatsu, T. Ikeda, K. Azuma, E. Fujiwara and M. Yatsuzuka : "Surface treatment of steel by short pulsed injection of high-power ion beam", *Suf. Coat. Technol.*, **136**, p.269 (2001).
- [3] R. M. Bayazitov, L. Kh. Zakirzyanova, I. B. Khaibullin, and G. E. Remnev : "Formation of heavily doped semiconductor layers by pulsed ion beam treatment", *Nucl. Instrum. & Methods in Phys. Res. B*, Vol.122, pp.35-38 (1997)
- [4] J. Khamsuwan, S. Intarasiri, K. Kirkby, C. Jeynes, P.K. Chu, T. Kamwanna, and L.D. Yu : "High-energy heavy ion beam annealing effect on ion beam synthesis of silicon carbide", *Surface & Coatings Technology*, Vol.206, pp.770-774 (2011)

# Dependence of anode shape on high intensity ion beam characteristics in plasma focus device

Kohei Yamamoto, Yuto Sagano, and Hiroaki Ito

*University of Toyama, 3190 Gofuku, Toyama 930-8555, Japan.*

## ABSTRACT

The plasma focus device can produce a high-temperature and high-density plasma and emits high-energy ions, electrons, X-rays, and neutrons. In order to apply the plasma focus device to the intense pulsed ion source, it is necessary to examine the ion acceleration mechanism for generating optimal ion beams. The characteristics of proton beams produced in the plasma focus device was studied. A capacitor bank of 41.6  $\mu\text{F}$  was charged to 30 kV to get a peak current of 460 kA. This paper reports the influence of the anode shapes on the ion beam. In the experiment, the angular distribution of the ion beam was measured with two different anode tips, cylindrical with a hollow top and tapered with a hollow top. The tapered hollow-end anode increases the ion beam intensity in comparison with the cylindrical hollow-end one.

## Keywords

Dense Plasma Focus, Z pinch plasma, Intense pulsed ion source,

## 1. Introduction

Plasma focus device has a relatively simple structure with a capacitor bank and electrodes, and can easily generate high-temperature and high-density plasma. Emissions of high-energy ions, electrons, X-rays, etc. and neutrons due to the DD reaction have been observed in the plasma focus device [1, 2]. The plasma focus has been anticipated for application as an ion source such as a fusion driver, an ion implantation and a thin film deposition [3,4], etc.

It is an interesting phenomenon that plasma focus devices having the charging voltage of a few tens of kV generate ions with energy more than a few hundred of keV to tens of MeV [5, 6]. The generation mechanism of the high-energy ion beam is believed to be closely correlated to phenomena that give rise to a localized high electric field, such as rapid compression during the radial pinch phase and instability. Many studies have been done to evaluate the characteristics of the high-energy ion beams to clarify the acceleration mechanism. Various models on the ion acceleration, such as the moving thermal plasma model [7], the generalized beam target model with a cross-field acceleration [8] and the converging ion

model [9], have been proposed and explained the production mechanism of high-energy ions to some extent. Although an individual model is best suited for a particular energy range, none of the models is in satisfactory agreement with the experimental results for all plasma focus devices. The physical production mechanism of these energetic ions has not been completely made clear.

The determination of ion beam characteristics is very important not only for understanding the generation mechanism of high-energy ions but also for their applications. It has been found that the generation of X-rays and neutrons depends on the material and geometry. We designed the tapered anode electrode with a hollow top to investigate the effect of the anode tip geometry on the ion beam. In this study, we evaluated the ion beam current produced by the plasma focus with the cylindrical and tapered anode electrodes with a hollow top.

## 2. Plasma Focus Concept

### 2.1 Operation principle of plasma focus

Figure 1 shows the principle of operation of the plasma focus. The plasma focus consists of a coaxial

inner electrode (anode) and an outer electrode (cathode), which are separated by an insulator. The operation principle is as follows. (1) When a high voltage is applied to the anode after filling a gas in the electrodes, the dielectric breakdown occurs between the two electrodes and a rapidly rising electric current (current sheath) flows on the insulator, as shown in the Fig 1. (2) The current sheath lifts off the insulator and is accelerated axially to electrode tip by the interaction of the current with its own magnetic field (Lorentz force  $J \times B$ ). (3) After the current sheath reaches the electrode top, the plasma contracts in the radial direction with axial motion. At the compression phase, a hot and dense plasma column is formed on the top of the anode. (4) The dense plasma column rapidly pinches and undergoes instabilities, such as Rayleigh-Taylor instability and sausage instability, etc. and breaks up. The intense x-rays and charged particle beams occur during the compression and breakup phases.

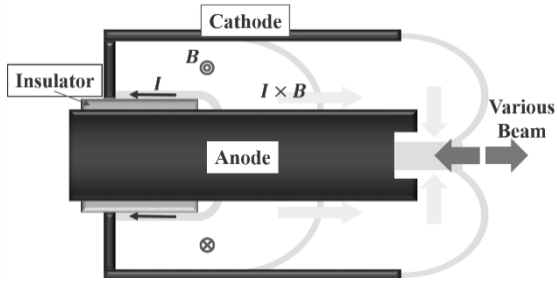


Fig. 1 Operation principle of plasma focus

## 2.2 Instability and Acceleration mechanism

The plasma column in the plasma focus pinches like the Z-pinch, which is a type of plasma confinement. The name refers to the direction of the current, the Z direction in cylindrical coordinate system. The plasma is compressed in the radial direction by the Lorentz force due to a magnetic field generated by the current in the plasma. The higher the current applied, the stronger the magnetic force generated and more tightly the plasma is confined. The plasma is not uniformly compressed, so passing high current through the plasma readily leads to instabilities such as narrowing at points known as a sausage instability, and kink instability.

Figure 2 shows the diagram of a sausage instability, which shows an axially symmetric perturbation

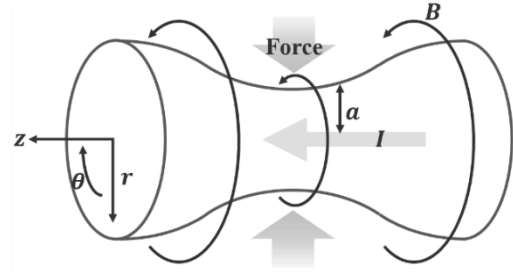


Fig. 2 Sausage instability

of the equilibrium of the Z-pinch. The magnetic field  $B_\theta$  around the plasma column is given by the following equation.

$$B_\theta = \frac{\mu_0 I}{2\pi r} \quad (r \geq a)$$

Here,  $r$  is the distance from the central axis,  $a$  is the radius of the plasma column and  $\mu_0$  is the magnetic permeability. Since  $B_\theta \propto r^{-1}$ , the magnetic pressure on the plasma surface is increased where the perturbation squeezes the plasma into a neck and is decreased where the perturbation fattens the plasma into a bulge. When the plasma is compressed nonuniformly, the gradient in the magnetic field causes the perturbation to grow and the necks contract to the axis, giving a sausage-like appearance to the plasma as shown in Fig. 2.

Figure 3 shows the diagram of the acceleration electric field generated by the neck. At both ends of the neck in sausage instability, ions and electrons in the plasma are deflected to form a virtual anode and cathode, thereby generating the acceleration electric field. The accelerated ions travel in the radial direction by the pressure of the magnetic field. When the ions pass over the central axis (z axis), the gradient in the magnetic field is reversed and they are moved back toward the central axis. Thus, in the sausage instability,

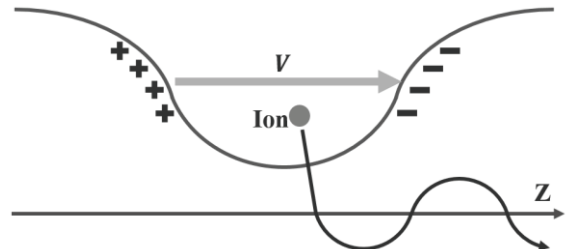


Fig. 3 Conceptual diagram of ion acceleration in sausage instability

the ions are thought to accelerate while meandering around the  $z$ -axis.

At the run-down phase of the plasma focus, the current sheath is accelerated and move toward the anode top at many times the speed of sound in the ambient gas. The shock wave is generated in front of the current sheath. As the current sheath reaches the top of the anode, the part of the sheath in contact with the anode slides axisymmetrically across the anode surface. As shown in Fig. 4, when the imploding front of the shock wave coalesces onto the axis, a reflected shock front emerges from the central axis and collides with the current sheath moving toward the center of the anode. After the collision, the radially inward motion of the magnetic piston is reversed. Thus, the axisymmetric boundary of the pinch plasma column is formed. To reduce the influence of the reflected shock wave, decreasing the diameter of the anode like the tapered electrode can reduce the time interval for the current sheath to move on the anode tip, i.e., radial phase and consequently, increase the induced electric field [10], [11]. Therefore, the ion beam is expected to be more accelerated axially.

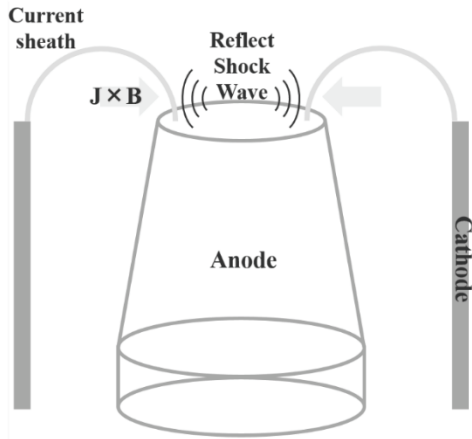


Fig. 4 Schematic of effect of taper electrode on pinch

### 3. Experimental Setup

The plasma focus device used in the present work is a Mather-type device having squirrel cage electrode geometry. The plasma focus device basically is comprised of a capacitor bank and an evacuated stainless-steel chamber. The electrode assembly of the plasma focus device consists of an inner electrode

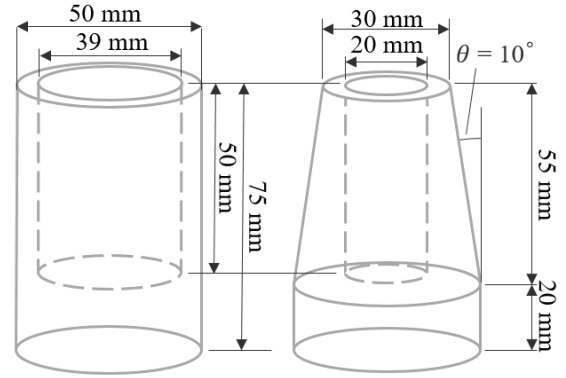


Fig. 5 Design of two anode tips

(anode), an outer electrode (cathode), and a glass insulator. The anode is a cylindrical copper electrode and its length and the diameter are 242 mm and 50 mm, respectively. The cathode is made up of 24 copper rods having 10 mm diameter and 230 mm long that are uniformly mounted coaxially with the anode. The effective inner diameter of the cathode is 100 mm. The bottom end of the electrode assembly is separated by a 100 mm long glass insulator sleeve, which is rigidly fixed around the central anode. The outer diameter of the insulator is 60 mm.

The cylindrical and tapered anodes with a hollow top were used in this experiment. Figure 5 shows the design of two anodes. Each electrode material is copper. In order to reduce the production of impurity ions and to reduce the damage of the electrode, the anode has a hollow shape top. The hollows of cylindrical and tapered anodes have 50 mm in depth and 39 mm and 20 mm in diameter, respectively. The diameters of cylindrical and tapered anode tips are 50 mm and 30 mm, respectively and the length of two anode tips is 75 mm. The inclination angle of the taper part is  $\theta = 10^\circ$ .

Figure 6 shows the experimental configuration of the plasma focus. The vacuum chamber is evacuated to  $5.0 \times 10^{-5}$  Torr or less and then filled with hydrogen gas. The filling pressure was changed in the range of 100 to 1000 Pa in steps of 100 Pa. The capacitor bank with a capacitance of 41.6  $\mu\text{F}$  was charged to 30 kV, which corresponded to the discharge energy of 19 kJ. The discharge current and ion current density were measured with a Rogowski coil and a biased ion collector (BIC), respectively. The BIC were arranged

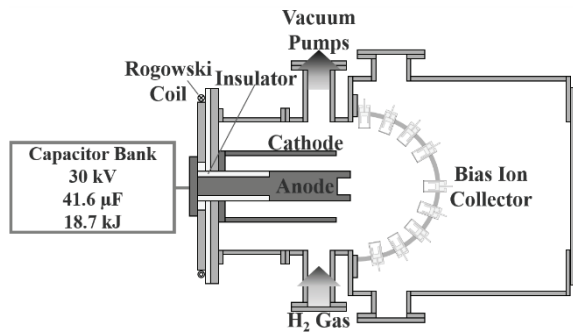


Fig. 6 Experimental configuration

on a circular frame of 110 mm in radius, centered at the focus, at nine different angles relative to the electrode axis,  $-80^\circ$ ,  $-60^\circ$ ,  $-40^\circ$ ,  $-20^\circ$ ,  $0^\circ$ ,  $30^\circ$ ,  $50^\circ$ ,  $70^\circ$  and  $90^\circ$ , as shown in Fig. 6.

#### 4. Experiment results and Discussion

Figure 7 shows the waveforms of the discharge current and the ion current density measured by BICs placed at  $0^\circ$  and  $80^\circ$ , where the cylindrical hollow-end anode was used and the filling pressure is 200 Pa. As seen in Fig. 7, the current has a large dip from 460 kA to 300 kA between 1.1  $\mu$ s and 1.9  $\mu$ s, which indicates the collapse of the plasma column after the pinch. The ion current density rises simultaneously with the current dip and the ion beam with a current density of 6.2 kA/cm<sup>2</sup> and a pulse duration of 200 ns is obtained. This indicates that the ion beam was accelerated by the electric field at the time of pinch. The ion current density at  $80^\circ$  rises at the almost same time as at  $0^\circ$  but a smaller current density of 0.4 kA/cm<sup>2</sup> and a wider pulse width of 3.5  $\mu$ s. It can be seen from Fig. 7 that the acceleration electric field in the plasma column is

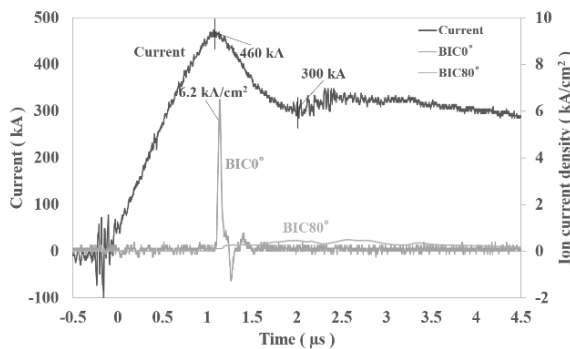


Fig. 7 Waveforms of discharge current and ion current density at  $0^\circ$  and  $80^\circ$

strongly generated in the axial direction of the anode electrode. Therefore, it is considered that the ion beam has maximum at  $0^\circ$  and is emitted radially around  $0^\circ$ .

Figure 8 shows the dependency of the gas pressure on the ion current density at  $20^\circ$  for the cylindrical and tapered anodes. With the tapered hollow-end anode, the aperture of the BIC placed at  $0^\circ$  narrowed due to the ablation and the measurement at  $0^\circ$  could not be performed accurately. Thus, the ion current density at  $20^\circ$  is used in Fig. 8. Three shots were made for each the cylindrical and tapered anode. Each data point shows the average value. It was found from this figure that the ion beam of the cylindrical hollow-end anode has the maximum value of 1.5 kA/cm<sup>2</sup> at the filling gas pressure of 200 Pa. On the other hand, the ion current density of the tapered hollow-end anode has the maximum value of 2.9 kA/cm<sup>2</sup> at 500 Pa. The optimum gas pressure of the ion beam depends on the shape of the anode tip. In addition, the ion current density was larger in the tapered hollow-end anode than in the cylindrical hollow-end anode.

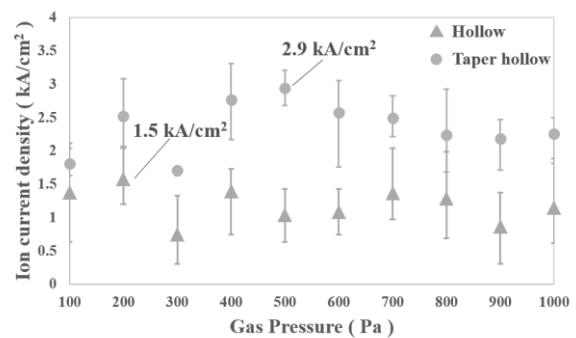


Fig. 8 Dependency of gas pressure on ion current density for cylindrical and tapered anodes

Figure 9 shows the angular distribution of the ion current density at the optimum filling gas pressure of 200 Pa and 500 Pa, respectively for the cylindrical and tapered anodes. Note that the ion current density at  $0^\circ$  for the tapered hollow-end type is shown for reference because of the ablation due to the intense ion beam. The fact that the ablation occurs only on the BIC placed at  $0^\circ$  indicates that the ion beam intensity is the highest. As seen in Fig. 9, the ion current density is the highest at  $0^\circ$  and decreases as the angle increases. Thus, it was found that the ion beam emanates radially around  $0^\circ$ . In comparison with the cylindrical hollow-

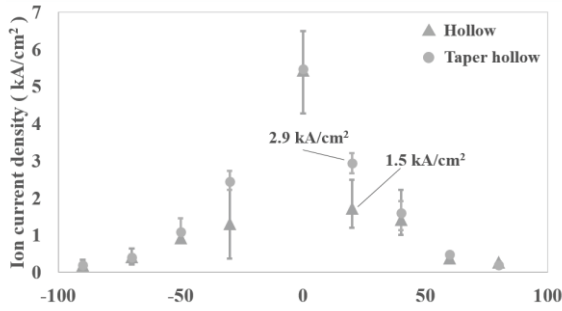


Fig. 9 Angular distribution of ion beam

end type, the ion current density for the tapered hollow-anode becomes higher at 20° and 30°, but is almost the same at the angles higher than 40°. With the tapered anode, the ion current density dose not increase uniformly in the azimuthal direction, but only in the vicinity of the axis. The tapered anode also has the higher reproducibility of the ion beam.

The effect of the tapered anode, reduction in the diameter, may be explained in the following way. Figure 10 shows schematic diagram of the influence of the anode tip geometry on the current sheath and the length of the plasma column. When the current sheath reaches the open end of the anode, it bows out into a shape like an umbrella, since the endpoints of the current sheet remain attached to the anode end. As shown in Fig. 10, in the case of the tapered anode, the current sheath makes a large angle ( $\theta$  : transition angle) with respect to the anode surface at the transit moment from the axial phase to the radial phase, since the speed of the current sheath at the anode end is larger in the tapered anode than in cylindrical one. As the transition angle becomes larger, the flexure of the current sheath is dramatically changed and the front part of the current sheath in contact with the anode elongates axially, which controls the final pinch plasma column length ( $h_1 < h_2$ ). Thus, the larger transition angle can suppress rapid changes in the current sheath motion at the transition and increase the symmetry of the accelerating current sheath, the swept mass introduced into the pinch phase, and the plasma lifetime before instabilities. As a result, the plasma column is strongly and stably pinched and the induced electric field, which is related to the sausage instability, is enhanced. As seen in Figs. 8 and 9, with the tapered anode, the ion beam current around the axis increases

and the reproducibility is improved as compared with the cylindrical anode.

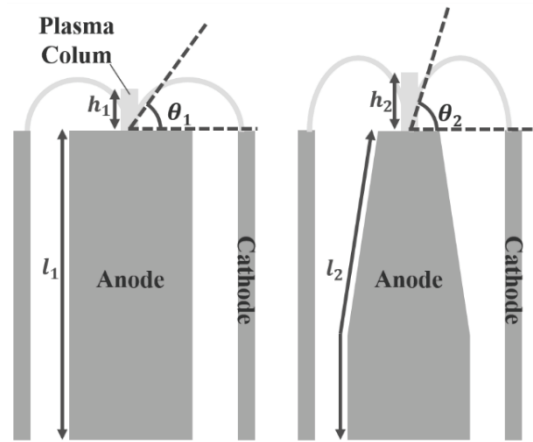


Fig. 10 Influence of anode tip geometry on current sheath and elongation of plasma column

## 5. Conclusions

The angular distribution of the pulsed ion beam from plasma focus device were evaluated by changing the shape of the anode. The tapered hollow-end tips significantly increase the intensity and reproducibility of the ion beam in comparison with the cylindrical hollow-end one. It was found that the ion beam intensity is dependent on the anode tip geometries and operating pressure. The results indicates that the plasma focus can generate the optimal ion beam by using an appropriate anode tip.

## • References

- [1] J. M. Koh et al., "Optimization of the high pressure operation regime for enhanced neutron yield in a plasma focus device," *Plasma Sources Sci. Technol.*, vol. 14, pp. 12–18, (2005).
- [2] V. Raspa, P. Knoblauch, F. D. Lorenzo, and C. Moreno, "Plasma focus based flash hard X-ray source in the 100 keV region with reproducible spectrum," *Phys. Lett. A*, vol. 374, pp. 4675–4677, (2010).
- [3] C.R. Kant, M.P. Srivastava and R.S. Rawat, "Thin carbon film deposition using energetic ions of a dense plasma focus", *Phys. Lett. A*, Vol.226, pp.212–216 (1997).
- [4] R.S. Rawat, V. Aggarwal, M. Hassan, P. Lee, S.V.

- Springham, T.L. Tan and S. Lee, "Nano-phase titanium dioxide thin film deposited by repetitive plasma focus", *Appl. Surf. Sci.*, Vol.255, pp.2932–2941 (2008).
- [5] K. Takao, Y. Doi, S. Hirata, I. Kitamura, K. Takahashi and K. Masugata, "Characteristics of ion beams produced in a plasma focus device", *Jpn. J. Appl. Phys.*, 40, pp.1013-1015 (2001).
- [6] H. Kelly, A. Lepone, A. Marquez, M. J. Sadowski, J. Baranowski and E. Skladnik-Sadowska, "Analysis of the Nitrogen Ion Beam Generated in a Low-Energy Plasma Focus Device by a Faraday Cup Operating in the Secondary Electron Emission Mode", *IEEE Trans. Plasma Sci.*, Vol.26, pp.113-117 (1998).
- [7] J. W. Mather in *Methods of Experimental Physics*, edited by H. Griem and R. H. Lovberg (Academic, New York, 1971), Vol. 9B, p. 187.
- [8] M. J. Bernstein, "Acceleration Mechanism for Neutron Production in Plasma Focus and z-Pinch Discharges", *Phys. Fluids* 13, pp.2858-2866 (1970).
- [9] J. H. Lee, L. P. Shomo, M. D. Williams and H. Hermansdorfer, "Neutron Production Mechanism in a Plasma Focus", *Phys. Fluids* 14, pp.2217 - 2222 (1971).
- [10] S. Lee and A. Serban, "Dimensions and Lifetime of the Plasma Focus Pinch", *IEEE Trans. Plasma Sci.*, Vol.24, pp.1101-1105 Sing Lee and Adrian Serban, (1996)
- [11] Morteza Habibi, "Angular distribution of ion beam emitted from a 3.5 kJ plasma focus device using different shapes of anodes", *Phys. Lett. A*, Vol.380, pp.439-443, (2016).

# Influence of voltage polarity on development of pulsed discharge over water surface and active species production

Hirotohi Takayama\*, Masahiro Takeda\*, Kazuki Karashima\*\*, Katsuyuki Takahashi\*\*\*, Koichi Takaki\*\*\* and, Takao Namihira\*\*\*\*

\* Faculty of Science and Engineering, Iwate University

\*\* Graduate School of Science and Technology, Kumamoto University

\*\*\* Agri-Innovation Center, Iwate University

\*\*\*\* Institute of Pulsed Power Science, Kumamoto University

**Abstract**— The influence of the voltage polarity on the development of pulsed discharge over the water surface and the hydroxyl radical production is investigated. A tungsten wire is placed above the water and is used as high voltage electrode. A stainless-steel disk is sunk to the bottom of the water and connected to the ground. The positive and negative pulsed high voltages are generated using a capacitive energy storage pulsed power generator driven by a MOS-FET. An ICCD camera is used for observation of the development of discharges. An indigo carmine solution is used as a chemical probe of hydroxyl radical. The emission intensity at wavelength of 308 nm corresponding hydroxyl radicals is observed using a spectrometer. The maximum discharge length, the propagation speed of discharges and the emission intensity in the case of negative polarity are higher than them of positive polarity. On the other hand, the amount of hydroxyl radical dissolved into the solution in the case of positive polarity is higher than that of negative polarity. The results show that positive ions produced in the positive discharges could contribute to hydroxyl radical production in the solution by the sputtering effect.

**Keywords**— Pulsed power, Water surface discharge, Polarity effect, Hydroxyl radical, Water treatment

## I. Introduction

A pulsed discharge plasma contacts to water surface has been attracted much attention for treating pollutants in water [1]-[4]. The pulsed discharge plasma can produce a non-thermal plasma with various chemical species. Those active species contribute to the decomposition of organic compounds in wastewater [5]-[7]. The discharge plasma can decompose persistent compounds quickly. Even though other advanced oxidation technologies require pH adjustment for productions of active species, the plasma does not require it because the active species is directly produced by the plasma [10]-[12]. However, its high running cost and processing equipment are main obstacle for practical use [13]. To improve the energy efficiency of wastewater treatment by discharge plasma, it is necessary to understand the basic property of discharge plasma at the gas-liquid interface.

It has been reported that the production efficiency of active species by discharges is affected by the voltage polarity [8][9]. The active species are mainly produced in the plasma through the chemical reactions such as electron impact. Using an atmospheric DC glow discharge contacts to the water surface with the positive polarity, it has been reported that hydroxyl radicals are also generated under water because the positive ions accelerated by the electric field collide with the grounded liquid surface[8]. The hydroxyl radical has high oxidation potential and contributes the oxidation reaction. In the case of negative polarity, the electrons accelerated by the

electric field collide with the liquid surface. Those electrons loses energy through repeated collisions with water molecules, and eventually becomes trapped by the water molecules to form a hydrated electron[9]. The hydrated electron has high reduction potential and contributes the reduction reaction.

In this study, the influence of voltage polarity on the development of pulsed discharge over the water surface and the production of chemical active species at the gas-liquid interface was investigated. The development of the discharge was observed using an ICCD camera. The emission spectra of the discharge was observed using a spectroscopy. The amount of hydroxy radical produced by the discharges was estimated using an indigo carmine solution, used as a chemical probe of hydroxyl radical.

## II. Experimental Setup

Fig.1 shows a schematic diagram of the discharge reactor. A stainless-steel plate (133 mm in diameter) was placed on the bottom of an acrylic resin cylindrical container (134 mm in diameter, 100 mm in height) and was used as the grounded electrode. A pulse high voltage was applied to a tungsten wire (0.5 mm in diameter) placed 3 mm above the liquid surface to generate discharges. A quartz glass container (150 mm in diameter) was placed on the cylindrical to seal the reactor. Argon gas was purged into the inside of the reactor with a gas

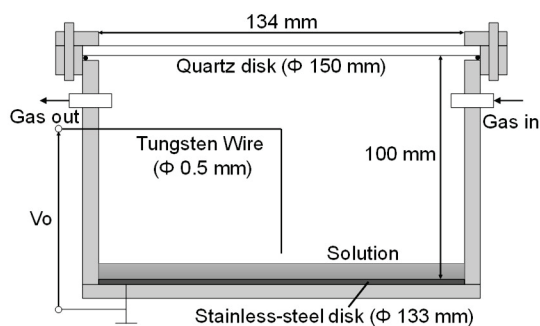


Fig 1 Schematic diagram of the reactor

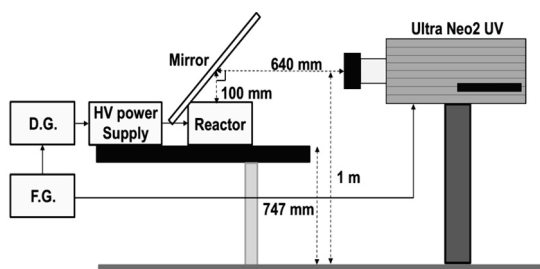


Fig 2 Schematic of the experimental system

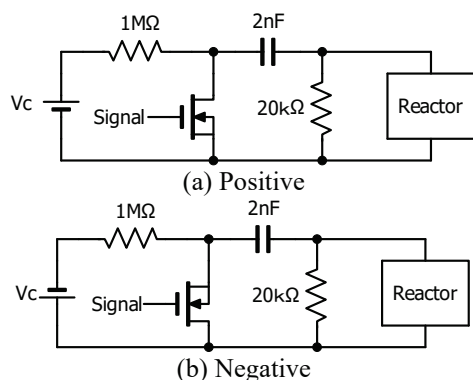
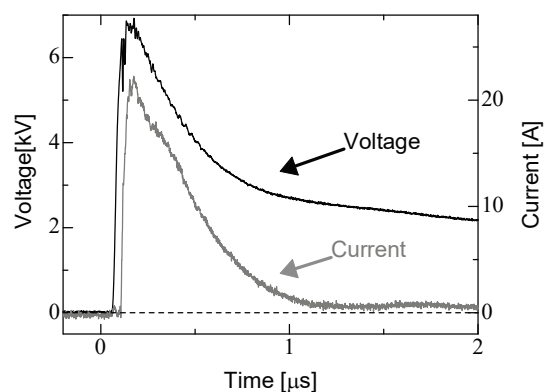
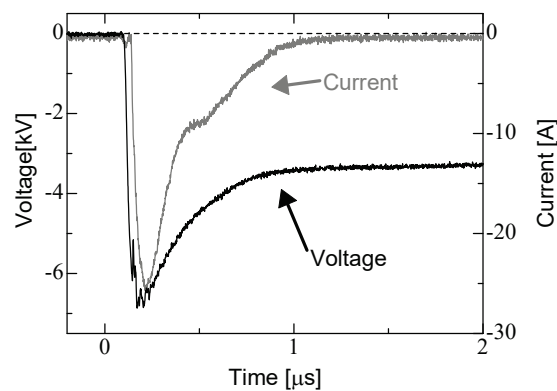


Fig 3 Schematic diagram of the discharge circuit

flow rate of 1 L/min. Fig.2 shows a schematic of the experimental system. A mirror placed above the reactor to observe the discharge development. The development of the same discharge was continuously observed by framing photographs continuously taken by a high-speed framing ICCD camera (Nac, Ultra Neo2 UV) with an interval of 150 ns. The exposure time of the ICCD camera was 150 ns. The velocity of development was estimated by dividing the discharge length by time. Fig.3 shows schematic diagrams of the high voltage pulsed power supply for (a) positive and (b) negative polarities. The pulsed power supply consisted of a MOS-FET (BEHLKE, HTS 201-20-LC2), a capacitor (MURATA, N4700 2 nF), and a 20 kΩ resistor parallelly connected to the reactor. Fig.4 shows typical waveforms of voltage and current. The maximum value of the applied voltage is fixed at  $\pm 7$  kV. The discharge repetition is frequency of 15 pps. The emission spectrum of the discharge was measured using a spectrometer (Stellarnet, Blue-WAVE UVN) with an exposure time of 10 s. The solution used for the spectroscopic measurement was 50 mL potassium nitrate solution. The conductivity was adjusted by the potassium nitrate concentration. The indigo carmine solution was prepared by dissolving the indigo carmine to 50 mL purified water with a concentration of 0.22 mM. The amount of indigo carmine decomposition was calculated using the following



(a) Positive discharge



(b) Negative discharge

Fig 4 Typical waveforms of voltage and current

equation (1) with an absorbance at 610 nm measured by a UV-vis spectrometer (SHIMADZU, UV-1850).

$$\begin{aligned} & \text{Amount of indigo carmine decomposition} \\ &= 50 \text{ [mL]} \times \text{Concentration(initial) [mM]} \\ & \times \frac{\text{Absorbance(initial)} - \text{Absorbance(treated)}}{\text{Absorbance (initial)}} \text{ [}\mu\text{mol]} \quad (1) \end{aligned}$$

The concentration of  $\text{H}_2\text{O}_2$  produced by the discharge was measured using the pack test (Kyoritsu Riken, WAK- $\text{H}_2\text{O}_2$ ). The discharge treatment time for indigo carmine and potassium nitrate solutions was 5 minutes.

### III. Results and Discussion

#### A. Observation of discharge

Fig.5 shows the framing photographs of the development of the discharge taken with the ICCD camera. The discharge develops from the electrode placed at the center to outer side of the reactor. Fig.6 shows relationship between discharge time and development length. In the early stages of the discharge, the discharge propagates linearly and then, the propagation is suppressed because the applied voltage is decayed. The maximum discharge length decreases with increasing conductivity. Fig.7 shows the velocity of the discharge as a function of conductivity. The discharge velocity of negative polarity is higher than that of positive polarity, especially, in the conductivity lower than 100  $\mu\text{S/cm}$ . At the conductivity of 100  $\mu\text{S/cm}$ , the discharge velocity is approximately 0.27 mm/ns for the negative polarity and

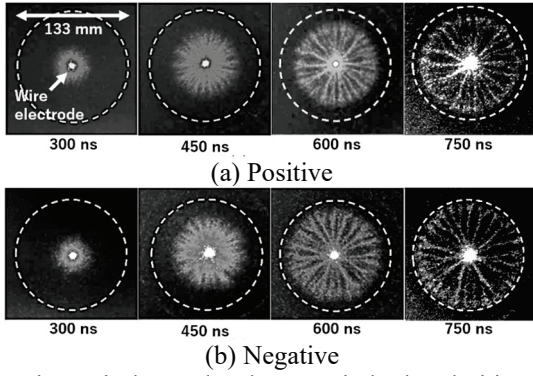


Fig 5 Discharge development in both polarities

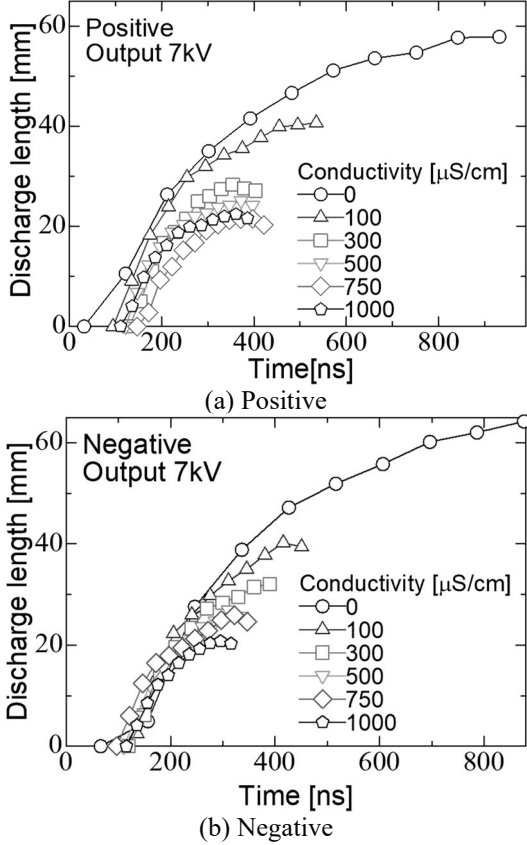


Fig 6 Time change of discharge length

approximately 0.18 mm/ns for the positive polarity. Fig.8 shows the relationship between the solution conductivity and the discharge length. The discharge length of negative polarity is longer than that of the positive polarity, and the discharge length decreases with increasing the conductivity. The decay time of the applied voltage decreased with the decrease in resistance in the liquid due to the increase in conductivity, and the relaxation time of the charge accumulated on the water surface also decreases. Therefore, the development of the discharge is suppressed by increasing the conductivity.

Fig.9 shows the photograph of the discharge taken by a digital camera with an exposure time of 1 s. The discharge channel of positive polarity is serration. On the other hand, the discharge channel of negative polarity is straighter than that of positive polarity, and the its brightness is higher than that of positive polarity.

Fig.10 shows typical emission spectrum of the discharge measured by the spectroscope. The intensity of the emission

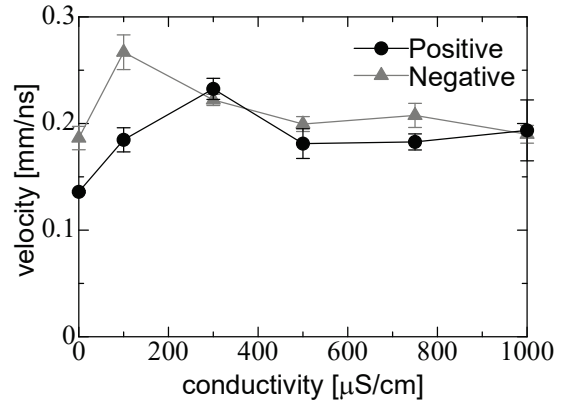


Fig 7 The discharge velocity as a function of conductivity

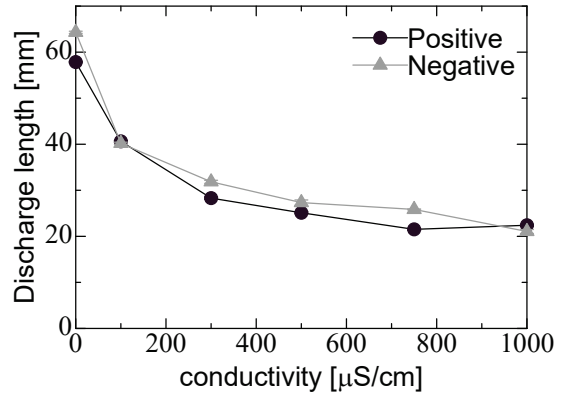
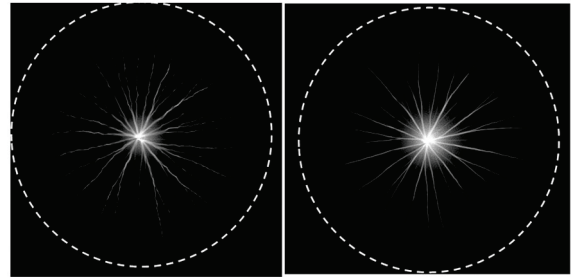


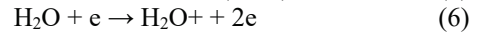
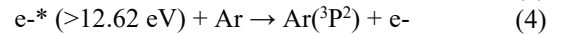
Fig 8 The discharge length as a function of conductivity



(a)Positive (b) Negative

Fig 9 Difference in discharge shape for positive and negative polarities

spectrum in the case of negative is higher than that of positive. When the atmosphere gas is Ar, hydroxyl radicals are produced in the plasma by the following reactions[14]-[17].



As shown in the fig. 10, the peaks at wavelength of 282 and 308 nm are emission lines of hydroxyl radicals. Fig.11 shows the intensity at wavelength of 308 nm which corresponds to excitation of hydroxyl radical as a function of conductivity.

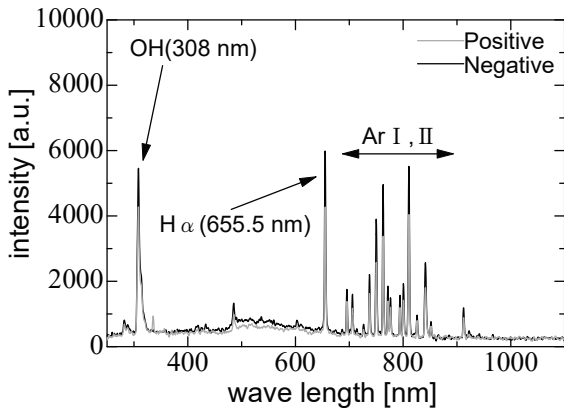


Fig 10 Example of observed emission spectrum

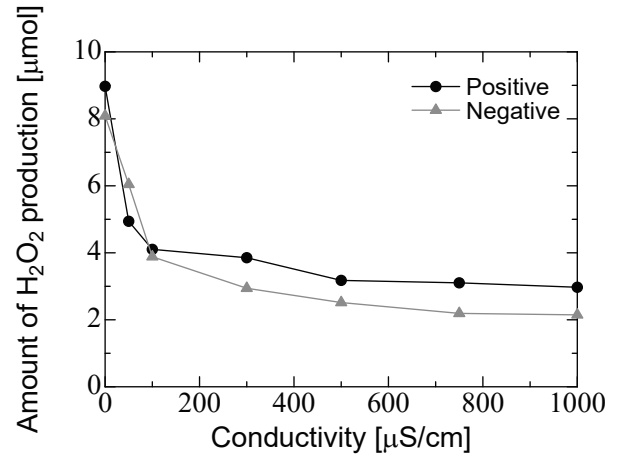


Fig 13 Amount of H<sub>2</sub>O<sub>2</sub> production as a function of conductivity

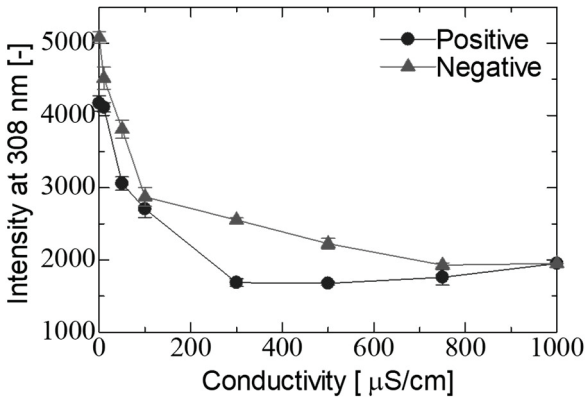


Fig 11 The emission intensity (308 nm) as a function of conductivity

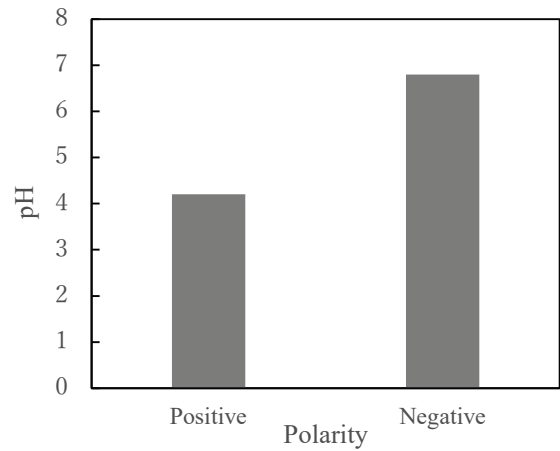


Fig 14 pH of KNO<sub>3</sub> solution after discharge treatment

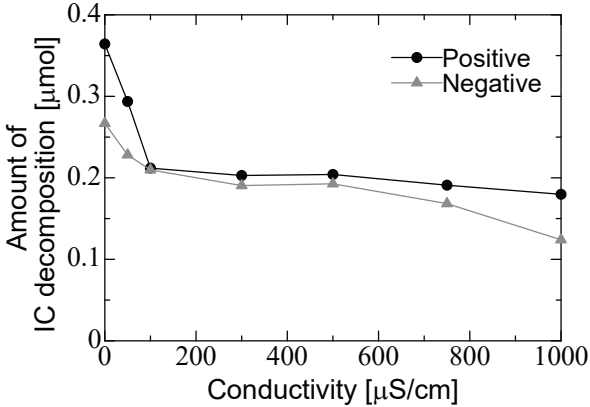


Fig 12 Amount of Indigo carmine decomposition as a function of conductivity

The emission intensity of negative polarity is higher than that of positive polarity, which shows The amount of hydroxyl radical production by discharges of negative polarity is higher than positive polarity. Therefore, the ionization density is higher in the negative polarity than in the positive polarity.

### B. Decomposition of Indigo carmine solution

Fig.12 shows the amount of indigo carmine decomposition as a function conductivity. The amount of indigo carmine decomposition decreases with increasing conductivity in both polarities. Fig.13 shows the amount of H<sub>2</sub>O<sub>2</sub> production as a function conductivity. The amount of H<sub>2</sub>O<sub>2</sub> production decreases with increasing conductivity in

both polarities. These results are similar to Fig.8 and Fig.11. On the other hand, the H<sub>2</sub>O<sub>2</sub> production and indigo carmine decomposition of the positive polarity is higher than them of the negative polarity. The results show that the amount of hydroxyl radical dissolved into the water are higher than them of the negative polarity. In the case of positive polarity, a positive ion sheath is formed between the discharge channel and the liquid surface [18]. The positive ions accelerated by this electric field collide with the liquid surface and generate hydroxyl radicals through following reactions [19][20].

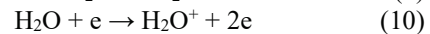
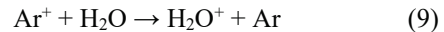


Fig.14 shows the pH of KNO<sub>3</sub> solution after discharge treatment with a treatment time of XX min. The initial pH of the solution is 5.5. The pH of the negative polarity decreases and that of positive polarity increases after discharge treatment. In positive polarity, hydrogen ions are formed in the liquid as shown in the equation (11), and the pH decreases [21]. Therefore, the amount of hydroxyl radical dissolved in the solution in the positive is higher than that in negative. In negative polarity, hydroxide ions are formed as shown in equation (12), and the pH increases[21].



#### IV. Introduction

The influence of discharge polarity on the development of the pulsed discharge on the water surface and the production of chemical active species is investigated. The discharge length and velocity in the negative polarity was faster than that in the positive polarity. The discharge development decreased with increasing conductivity in both polarities. The emission intensity at 308 nm corresponds to hydroxyl radical in the negative polarity is higher than that in the positive, which shows that the amount of hydroxyl radical production in the negative is higher than that in positive. The amount of indigo carmine decomposition and the amount of H<sub>2</sub>O<sub>2</sub> production in the positive polarity were higher than them in the negative polarity, and the amount of hydroxyl radical dissolved in the solution in the positive is higher than that in the negative. The results show that hydroxyl radical is generated in the solution by positive ions generated by the plasma and accelerated by the ion sheath formed between the discharge channel and the liquid surface.

#### Acknowledgements

This work was supported by a Grant-in-Aid for Scientific Research (S), Grant Number 19H05611.

#### References

- [1] K. Takahashi, Y. Saito, R. Oikawa, T. Okumura, K. Takaki and T. Fujio, *J. Electrostat.*, 2018, 91, 61-69
- [2] T. von Woedtke, S. Reuter, K. Masur, and K. D. Weltmann, *Phys. Rep.*, 2013, 530, 4, 291-320
- [3] Y. Huang, Y. Kou, C. Zheng, Y. Xu, Z. Liu and K. Yan, *IEEE Trans. Plasma Sci.*, 2016, 44, 6, 2654-2655
- [4] K. Takahashi, K. Takaki, and N. Satta, *J. Adv. Oxidat.*, 2012, 15, 2, 365-373
- [5] H. Akiyama, *IEEE Trans. Dielectr. Electr. Insul.*, 2000, 7, 5, 646-653
- [6] K. Takahashi, K. Takaki and N. Satta, *J. Adv. Oxidat.*, 2012, 15, 2, 365-373
- [7] M. A. Malik, A. Ghaffar and S. A. Malik, *Plasma. Sources Sci*, 2001, 10, 1, 82-91
- [8] A. A. Joshi, B.R. Locke, P. Arce, W.C. Finney : *Journal of Hazardous Materials*, Vol.41, No.1 pp.3-30 (1995)
- [9] Paul Rumbach, David M. Bartels, R. Mohan Sankaran and David B. Go : *Nature Communications*, Vol. 6, p. 7248 (2015)
- [10] K. Takahashi, K. Takaki, N. Satta and M. Akiyama, *Proceedings of environmental engineering research*, 2010, Vol. 47, pp.31-37 (in Japanese)
- [11] K. Takahashi, Y. Sasaki, S. Mukaigawa, K. Takaki, T. Fujiwara and N. Satta, *IEEE Trans. Plasma Sci.*, 2010, 38, 2694-2700
- [12] A. Yonezawa, K. Takahashi, N. Satta, and K. Takaki, *J. Inst. Electrostat*, 2011, Vol. 35, pp.31-37 (in Japanese)
- [13] R. Ono, Y. Nakagawa and T. Oda, *J. Phys.D, Appl. Phys.*, 2011, 44, 485201-485214
- [14] T. Shirafuji, T. Murakami, *Jpn. J. Appl. Phys.*, 54 (2014) 01AC03.
- [15] N. Takeuchi, M. Ando, K. Yasuoka, *Jpn. J. Appl. Phys.*, 54 (2015) 116201.
- [16] B. Eliasson, W. Egli, and U. Kogelschatz, *Pure & Appl. Chem.*, 1994, Vol.66, No.6, pp.1275-1286
- [17] P. Wentworth Jr., E. McDunn, A.D. Wentworth, C. Takeuhi, J. Nieva, T. Jones, C. Bautista, J. M. Ruedi, A. Gutierrez, K.D. Janda, B.M. Babior, A. Eschenmoser and R.A. Lerner, *Science*, 2002 Vol.298, No.13, pp.2195-2199
- [18] D. Tanaka, K. Akiko and K. Hidaka, *IEEJ Transactions on Fundamentals and Materials*, 2014, Vol.134, No.3, pp. 118-125
- [19] B. Eliasson, W. Egli, and U. Kogelschatz, *Pure & Appl. Chem.*, 1994, Vol.66, No.6, pp.1275-1286
- [20] P. Wentworth Jr., E. McDunn, A.D. Wentworth, C. Takeuhi, J. Nieva, T. Jones, C. Bautista, J. M. Ruedi, A. Gutierrez, K.D. Janda, B.M. Babior, A. Eschenmoser and R.A. Lerner, *Science*, 2002 Vol.298, No.13, pp.2195-2199
- [21] S. Wakisaka, K. Tsuda, K. Takahashi, and K. Satoh :, *IEEE Transactions on Plasma Science*, Vol. 47, No. 2, pp. 1083-1088 (2019)

# Influence of Drying Rate and Quality Changes on Hot Air Drying Processing of Spinach using Pulse Electric Field

Takahiro Yamada<sup>\*</sup>, Yamakage Kouya<sup>\*\*</sup>, Katsuyuki Takahashi<sup>\*,\*\*\*</sup>, Koichi Takaki<sup>\*,\*\*\*</sup>,  
Takahiro Orikasa<sup>\*\*,\*\*\*</sup>, Junichi Kamagata<sup>\*\*\*\*</sup>, and Hitoshi Aoki<sup>\*\*\*\*</sup>

<sup>\*</sup> Faculty of Science and Engineering, Iwate University

<sup>\*\*</sup> Faculty of Agriculture, Iwate University

<sup>\*\*\*</sup> Agri-Innovation Center, Iwate University

<sup>\*\*\*\*</sup> Inc Nichirei Foods

**Abstract**—Influence of pulse electric field (PEF) on the drying rate and quality changes of spinach on the hot air drying process is investigated. Eight spinach leaves cut to square shape with an area of 60 mm<sup>2</sup> are used as a sample. PEF is generated by a capacitive energy type pulse generation circuit consisted of a capacitor and a SiC-MOSFET. Parallel plate electrodes with a gap length of 10 mm are used to apply PEF to the sample. The samples are dehydrated using a hot air dryer after the PEF treatment. The moisture content of the samples decreases with increasing drying time, and has a constant value after 2 hours and 3.5 hours for the PEF treatment group and control group, respectively. The drying rate constant in the case of PEF treatment group is 1.6 times higher than that of control group. These results show that the moisture permeability of leaves is improved by destroying the cell membrane by PEF. The surface area of samples after drying process in the case of PEF treatment group is larger than that of control groups, which could also improve the drying rate constant. In addition, the influence of PEF treatment on the quality after hot air drying process was small.

**Keywords**— Pulse electric field, spinach, Hot air drying, electroporation, drying rate, quality changes

## I. Introduction

In recent years, processed foods demands have increased due to the development of various food cultures. The dry processed food products has been widely distributed because of their advantages in a long storage period and a transportability. Hot air drying, one of the drying processes, is an useful way for drying foods. However, it takes a lot of time to finish drying and energy costs.

Pulsed electric field (PEF) can induce various physical and chemical effects inside the food, which causes irreversible destruction of the cell membrane and improves the moisture permeability with non-heating and low energy. Recent studies have reported that PEF treatment softens cellular tissues of fruits and vegetables<sup>(1)</sup>. Also, there are reports that softening of fruits and vegetables contributes to the improvement of moisture evaporation under hot air drying<sup>(2)</sup>. Therefore, by introducing PEF before hot-air drying, the drying time can be shortened and the cost of drying can be reduced. Additionally, PEF treatment does not include a dipping operation, which can prevent leakage of water-soluble components such as L-ascorbic acid. In this study, the influence of PEF on drying rate and quality changes of spinach during the hot air drying process is investigated.

## II. Experimental Setup

### A. Material

Spinach (*Spinacia oleracea* L.) from Iwate prefecture was purchased from a supermarket. Spinach was stored in a refrigerator at 4 °C, and used within one day. Spinach leaves were shaped squarely with the area of 60 mm<sup>2</sup>. The initial moisture content of the sample was  $10.8 \pm 0.8$  (dry basis moisture content (D.B.)) (n = 16) using the 105 °C-24 hours method (3).

### B. PEF treatment method

Figure 1 shows the schematic diagram of the PEF treatment system. Figure 2 shows the schematic diagram of the parallel plates electrode reactor. PEF treatment is performed by clamping a sample between parallel plates, and using a capacitive energy storage type pulse generator driven by a SiC-MOSFET. The capacitor is charged using a DC power supply (Pulse Electronic Engineering Co., Ltd., MODEL-600F). When the SiC-MOFET is turned on, the energy stored in the capacitor is transferred to the reactor, and a pulsed electric field is applied to the sample in the reactor. Figure 3 shows the photograph of Spinach location in the reactor. Spinach leaves are stacked eight. The gap length between the plates is 10 mm. Figure 4 shows the typical waveforms of applied voltage and current flows the sample. The applied voltage, pulse width, and pulse repetition rate are 3 kV, 1  $\mu$ s, 1-30 pps, respectively.

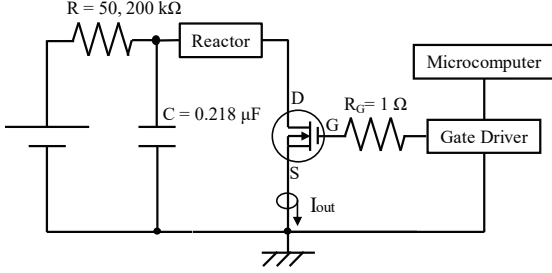


Fig.1 Experimental circuit  
High Voltage

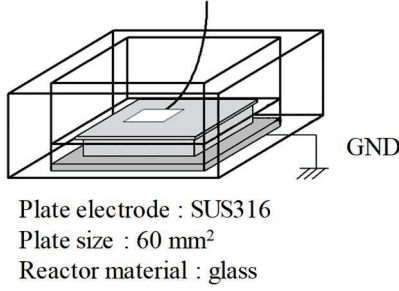


Fig.2 Schematic diagram of a parallel plate electrode reactor

### C. PEF treatment method

Figure 1 shows the schematic Samples after PEF treatment and control group are put on a wire mesh placed in a hot air dryer (Yamato Scientific Co., Ltd., DKM600) with an inner temperature of 50 °C. The mass of the samples is measured during drying process. The drying process is completed when the mass change is less than 0.01 g. The dry basis moisture content ( $M_{dry}$ ) is calculated using the following equation,

$$M_{dry} = \frac{W - W_0}{W_0} \quad (1),$$

where  $W$  and  $W_0$  are the measured weight and the dry weight calculated from initial moisture content, respectively. The drying rate ( $-dM_{dry}/dt$ ) represents the amount of removed water from the sample per unit time, which is obtained from the following equation,

$$-\frac{dM_{dry}}{dt} = aM_{dry} + b \quad (2),$$

where  $a$ ,  $b$ , and  $W_{dry}$  are the drying rate constant, intercept, and dry basis moisture content, respectively.

### D. Quality change measurement method

*L*-ascorbic acid, potassium, and Brix sugar content of the samples are evaluated before and after drying process. The drying time set to 5 hours, because preliminary experiment showed that the sample dried after 5 hours in a hot air dryer set at 50 °C. *L*-Ascorbic acid has been used as an indicator of the quality dried fruits and vegetables <sup>(4),(5)</sup>. The measurement method is as follows. The samples after drying mix with a 2% metaphosphoric acid solution (w/w) using a homogenizer (As One Co., Ltd., CM-100) (8000 rpm, 10 min, 0 min). After filtering through a filter paper (ADVANTEC, 5A 150 mm), the *L*-ascorbic acid content in the filtered liquid (filtrate) measured with RQ-flex Plus (Merck Co., Ltd.). In addition,

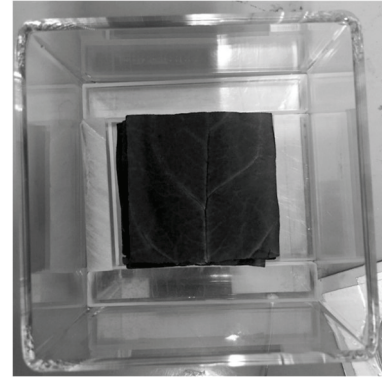


Fig.3 Photograph of Spinach location in the reactor

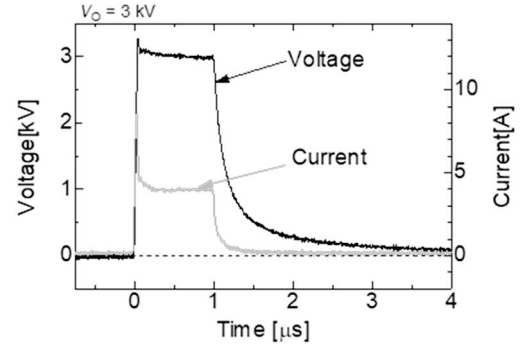


Fig.4 Typical waveforms of voltage and current

the *L*-ascorbic acid residual rate was evaluated by dividing the value of the PEF treatment group by that of the control group Potassium can adjust the osmotic pressure of cells, so that essential soluble mineral for the human body. The measurement method is as follows. The dried sample mix with a distilled water using a homogenizer (As One Co., Ltd., CM-100) (8000 rpm, 10 min, 0 min). After that, it is measured by the same way as *L*-ascorbic acid.

Brix sugar content is generally used as an indicator of fruit and vegetable quality. The measurement was performed by the same way as the potassium measurement until the preparation of the filtrate. The Brix sugar content contained in the filtrate was measured using a hand-held refractometer (Atago Co., Ltd., N1).

## III. Results and Discussion

### A. Hot air drying evaluation

Figure 5 shows the leaf weight of spinach as a function of dry time during hot air drying process. The weight content of the samples decreases with increasing drying time, which indicates that the water of spinach is transpired during the hot air drying process. The weight after drying of control and PEF treatment group were  $0.076 \pm 0.003$  g and  $0.082 \pm 0.004$  g, respectively, and it was equivalent.

Figure 6 shows the moisture content of spinach as the function of time during the drying process. The moisture content of the samples decreases with increasing drying time. And the moisture content of the PEF treatment group and control group have constant values after 2 hours and 3.5 hours, respectively. As the result, the drying time could be reduced by about 1.5 hours by PEF treatment before hot air drying. Therefore, the drying time and cost could reduce by about 40 to 50%.

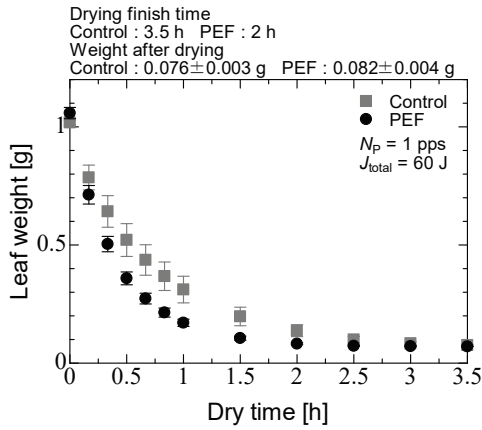


Fig.5 Leaf weight of spinach as a function of dry time during hot air drying process

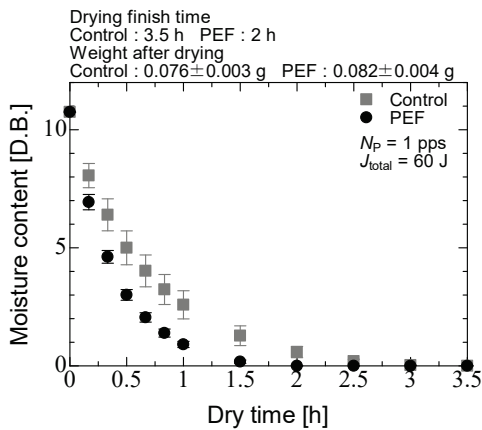


Fig.6 Moisture content of spinach as a function of dry time during hot air drying process

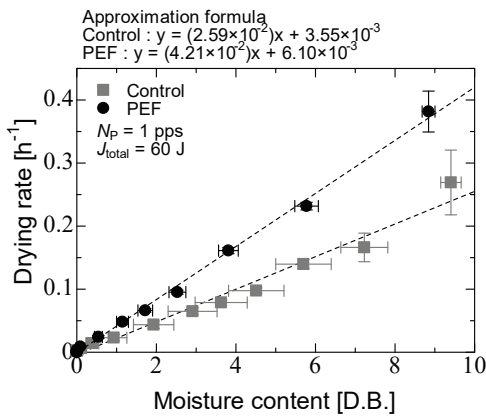


Fig.7 Drying rate of spinach as a function of moisture content

Figure 7 shows the drying rate of spinach as a function of moisture content. The drying rate decreases linearly as the decrease of moisture content. The drying rate constant of control and PEF treatment groups were 0.026 and 0.042, respectively. As a result, the drying rate constant was increased by about 1.6 times.

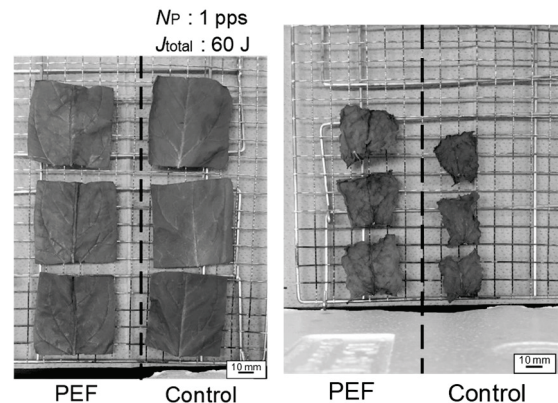


(a)



(b)

Fig.8 Photographs of leaves (a) before and (b) after PEF treatment



(a)

(b)

Fig.9 Photographs of leaves (a) before and (b) after hot air drying

Figure 8 shows the photographs of leaves (a) before and (b) after PEF treatment. From diagram, it can visually confirm that moisture adhere to the leaf surface after the PEF treatment. The cell membrane is broken by PEF treatment and the moisture move to the leaf surface, which facilitate the evaporation of moisture during drying.

Figure 9 shows the surface area of leaves as a function of dry time during hot air drying process. The spinach leaf is shrunk after 3.5 hours drying. The decrease in the apparent surface area of spinach in the control group is higher than that of PEF group. Figure 10 shows the surface area of leaves quantitated with ImageJ software as a function of dry time during hot air drying process. The drying surface area after 3.5 hours drying of control and PEF treatment groups were  $7.32 \pm 1.94 \text{ cm}^2$  and  $12.59 \pm 0.67 \text{ cm}^2$ , respectively. Recent

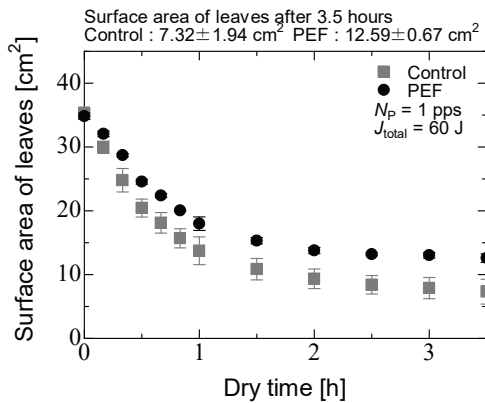


Fig.10 Surface area of leaves as a function of dry time during hot air drying process

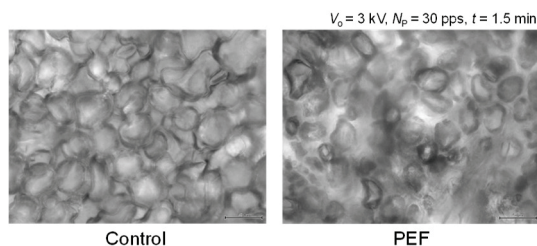


Fig.11 Sample structure before hot-air drying using an optical microscope

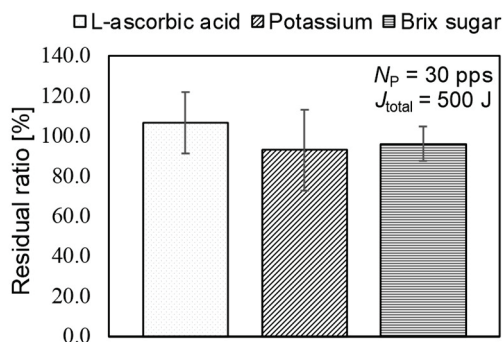


Fig.12 Residual ratio of L-ascorbic acid and Potassium, Brix sugar for dried Spinach after hot air drying process

studies have reported that suppression of shrinkage of the sample surface area has improved the drying rate<sup>(7)</sup>. In this study, it was considered that the shrinkage of leaves during hot air drying could be suppressed because the cell walls are separated by the PEF treatment. Figure 11 shows the sample structure before hot-air drying using an optical microscope (OLYMPUS, BX41). From the figure, it can be seen that the cell walls are adhered in the control group, but the cell walls are separated in the PEF treatment group. When the cell wall sticks, it shrinks due to the force pulling the inside of the leaf. On the other hand, the adhesion of the cell wall of the PEF treatment groups was weak, so that the force of pulling inside of leaf was dispersed, which shrinkage was suppressed. The cell wall adhesion is caused by the action of pectin. The pectin is degraded by the polygalacturonase and pectin lyase, and it has been reported that polygalacturonase is localized in

the vacuole<sup>(8)</sup>. Therefore, it was suggested that polygalacturonase in the vacuole was migrated to the cell wall by PEF treatment, and was reacted pectin. As the result, the cell walls were separated.

#### B. Quality change evaluation

Figure 12 shows the residual ratio of L-ascorbic acid and Potassium, Brix sugar for dried Spinach after hot air drying process. From the figure, the residual ratio of L-ascorbic acid, potassium, and Brix sugar content were  $106.3 \pm 15.3\%$ ,  $92.9 \pm 20.2\%$ , and  $95.9 \pm 8.5\%$ , respectively. The results show the contents inside sample could be kept by PEF treatment.

#### IV. Conclusion

In this study, the influence of PEF on drying rate and quality changes of spinach during the hot air drying process is investigated. The drying rate constant of PEF treatment group better increased by about 1.6 times than control group, and the drying time can be reduced 1.5 hours. The time and cost for the drying process can be reduced about 40 to 50%. The contents inside sample could be kept by PEF treatment.

#### Acknowledgements

The part of work was supported by Urakami Foundation for Food and Food Culture Promotion. Also, the SiC-MOSFET used in the experimental equipment was provided by Tsukuba Power Electronics Constellations (TPEC).

#### References

- [1] De Vito F, *et al.* : "Pulse Duration and Efficiency of Soft Cellular Tissue Disintegration by Pulsed Electric Fields", *Food and Bioprocess Technology*, Vol.1, pp.307-313 (2008)
- [2] Nilnakara S, *et al.* : "Production of antioxidant dietary fibre powder from cabbage outer leaves", *Food and Bioprocess Technology*, Vol.87, No.4, pp.301-307 (2009)
- [3] Topuz A, *et al.* : "The effect of drying method and storage on color characteristics of paprika", *LWT Food Science and Technology*, Vol.42, pp.1667-1673 (2009)
- [4] Santos, P. H. S. *et al.* : "Retention of vitamin C in drying processes of fruits and vegetables", *A Review Drying Technology*, Vol.26, pp.1421-1437 (2008)
- [5] Orikasa T, *et al.* : "Analysis of changes in moisture content and L-ascorbic acid of sweet potatoes during hot air drying", *Journal of Miyagi University, School of Food, Agricultural and Environmental Sciences*, Vol.5, pp.35-41 (2011)
- [6] Zimmermann U, *et al.* : "DIELECTRIC BREAKDOWN OF CELL MEMBRANES", *Biophysical Journal*, Vol. 14, No. 11, pp. 881-899 (1974)
- [7] Watanabe T, *et al.* : "The influence of inhibit avoid

water defect responses by heat pretreatment on hot air drying rate of spinach” , *Journal of Food Engineering*, Vol.168, pp.113-118 (2016)

- [8] Hong Wu, *et al.* : “Reduction in vacuolar volume in the tapetal cells coincides with conclusion of the tetrad stage in *Arabidopsis thaliana*”, *Sexual Plant Reproduction*, Vol.18, pp.173-178 (2005)

[9]

# Silicon wafer etching by burst-mode high-power inductively coupled Ar/CF<sub>4</sub> plasmas with 150 kHz band frequency

Yuma Saito\*, Kodai Shibata\*, Katsuyuki Takahashi\*, Seiji Mukaigawa\*, Koichi Takaki\*, Ken Yukimura\*, Hisato Ogiso\*\*, Shizuka Nakano\*\*

\*Faculty of Engineering, Iwate University, Japan

\*\*National Institute of Advanced Industrial Science and Technology, Japan

**Abstract**— A silicon wafer etching using a burst pulse high-power inductively coupled plasma (ICP) is investigated. A 200  $\mu\text{s}$  wide burst of a 157 kHz power supply is employed to generate ICP with a repetition rate of 50 Hz. A rectangular pulsed voltage synchronized with the burst power supply is applied upto 1 kV at the wafer. Mixed gas of argon (Ar) and tetrafluoromethane (CF<sub>4</sub>) is supplied into the vacuum chamber. The plasma density and electron temperature are  $10^{19} \text{ m}^{-3}$  and 2.8 eV where the wafer is, respectively. In the case of Ar plasma, the silicon etching rate is 0.01  $\mu\text{m}/\text{min}$  with 1000 V negative bias. The etching rate increases to 0.23  $\mu\text{m}/\text{min}$  by adding CF<sub>4</sub> into Ar and increases linearly with increasing the bias voltage. The target current and emission intensity of Ar<sup>+</sup> and F<sup>\*</sup> are depended on bias voltage from -300 to -1000 V. The etching rate sharply increases by increasing CF<sub>4</sub> content from 0% to 10%, and it becomes almost constant at 10%. The dependency of emission intensity of F<sup>\*</sup> on CF<sub>4</sub> content is similar to the dependency the etching rate.

**Keywords**—burst-ICP (Inductively coupled plasma), high density plasma, etching, silicon wafer, pulsed plasma, CF<sub>4</sub>

## I. Introduction

Techniques of ion beam milling, reactive ion etching, radio frequency (rf) sputter etching, and plasma etching have been used for the profile control of semiconductor device fabrication. Plasma etching of materials is used for processes such as planarization, patterning, and removal of the damage layer and resist removal (ashing). As plasma sources, inductively coupled plasma (ICP) has been widely used for these processes due to its advantages.<sup>1-4)</sup> For example, ICP can be generated without electrodes, generated ions can be independently controlled by the applied bias voltage to the substrate.<sup>5,6)</sup> ICP can be generated and maintained with a wide range of driving frequency from 50 Hz up to GHz.<sup>1)</sup> Typically, plasma reactors use an rf power source with constant average power or voltage to excite the plasma in a vacuum chamber. Such mode of operation is known as continuous-wave rf mode.<sup>7)</sup> Several researchers have demonstrated through numerical modeling and experimental studies that pulsing the rf power input, i.e., pulsed rf mode, has the promise to increase the flexibility of plasma processing by enlarging the range of operating conditions.<sup>7)</sup> Pulsed plasmas have emerged as promising candidates to address the formidable challenges of fabricating future generations of micro-devices.<sup>8)</sup>

A high-power pulsed ICP system with a frequency of 100–200 kHz has been developed to generate a high-density plasma.<sup>9-14)</sup> In this system, a 100–600  $\mu\text{s}$  wide burst of the rf power is used to produce a plasma with the duty cycle on the order of 1%–10%. The inductor coil and the capacitor are resonant at the frequency without an impedance matching facility. Because the power density in this system is much higher than the general rf system, a high plasma density of  $10^{19}$

$\text{m}^{-3}$  can be obtained. If the duty ratio and the burst duration of the rf power source can be adequately adjusted, it is possible to optimize process conditions. For example, the plasma is compact with a cylindrical shape and a diameter of 50 mm. Thus, the size and cost of the equipment can be reduced, and the high-density plasma source is expected to be applied to high-speed processes. This plasma source can possibly be applied to a minimal fab semiconductor manufacturing system in a similar manner to the 1-inch-sized high-power impulse magnetron sputtering system.<sup>15,16)</sup>

In this paper, a silicon wafer was etched by the high-power pulsed inductively coupled Ar/CF<sub>4</sub> plasma and the etching rate was evaluated. A rectangular pulse voltage of negative polarity was applied on the wafer holder electrode. The influence of bias voltage, the ratio of CF<sub>4</sub> to Ar, and rf power on the etching rate were investigated. To investigate the basic characteristics for the etching process using this plasma source, Ar/CF<sub>4</sub> gas and silicon wafer were used because they have been widely used in basic experiments.

## II. Experimental Setup

Fig. 1 shows a schematic of the experimental apparatus. The vacuum chamber consists of cylindrical glass tubes (51 mm inner diameter, 55 mm external diameter) connected in series. A solenoid coil (50 turn, 70 mm length, 84  $\mu\text{H}$ ) is wound on the glass tube. The capacitor of 12 nF is connected to the coil in parallel. A 200  $\mu\text{s}$  wide burst of a 157 kHz power supply (PS-1) is employed to generate ICP with a repetition rate of 50 Hz. 157 kHz is resonance frequency of the LC

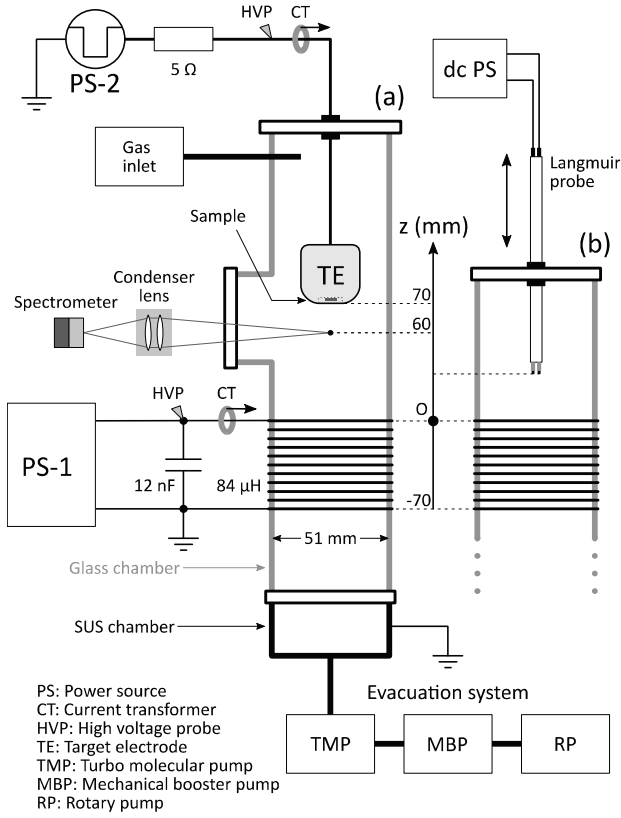


Fig. 1 Schematic of the experimental apparatus.

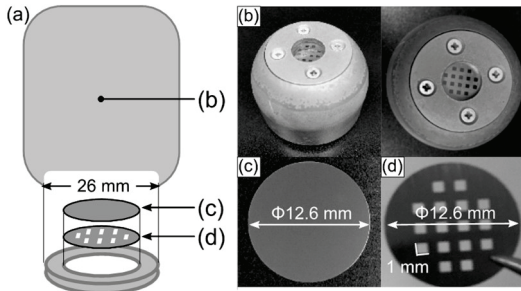


Fig. 2 (a) Structure of sample holder, (b) target electrode, (c) silicon wafer, and (d) stainless steel mask.

resonance circuit consisted of the capacitor (12 nF) and the coil (84  $\mu$ H). Argon (Ar) and tetrafluoro-carbon ( $\text{CF}_4$ ) gases are supplied through mass flow controllers (SEC-400MK3 and SEC-E40MK3, HORIBA, respectively) into the chamber. Total gas flow rate is controlled in range of 11.3–40.0 sccm. Gas pressure inside the chamber ranges from 1 to 2.4 Pa. The coil voltage and current are measured by a high voltage probe (HV-P30, Iwatsu) and a current monitor (model 110A, Pearson), respectively.

**Fig. 2** shows (a) structure of sample holder, (b) target electrode (40 mm diameter, 35 mm length), (c) silicon wafer [(100), 12.6 mm diameter, 250  $\mu$ m thickness], and (d) stainless steel mask (12.6 mm diameter, 150  $\mu$ m thickness). Since the wafer has been stored in room air, oxide films can be formed naturally on the surface of the wafer. A stainless-steel mask (12.6 mm diameter, 150  $\mu$ m thickness) with 1 mm square holes is placed on the wafer. The target electrode is made of Ti (40 mm diameter, 35 mm length) and has a cylindrical shape with round edges. The target electrode is placed in the chamber at 70 mm away from the coil end as shown in **Fig. 1** (a). A rectangular pulse voltage of negative polarity (PS-2) is

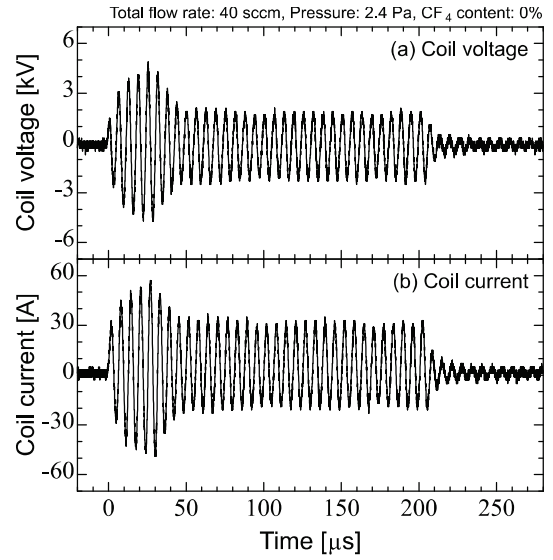


Fig. 3 Typical waveforms of (a) coil voltage and (b) current.

applied to the target electrode through a 5  $\Omega$  current controlling resistance. A 200  $\mu$ s wide rectangular pulsed voltage synchronized with the burst power supply (PS-1) is applied to the target with an amplitude ranged from 0 to -1000 V, and the repetition rate is 50 Hz. Voltage applied to the target and current flowing into the electrode are measured by a high voltage probe (P-5100, Tektronix) and a current monitor (model 110A, Pearson), respectively. The integrated optical emission spectra in the whole event during the plasma generation are measured by a spectrometer (Blue-WAVE model UVN-25, StellarNet, 600 Gr/mm grating). The observation point is focused using a condenser lens at 10 mm away from the bottom face of target electrode.

The electron temperature and ion density are obtained by floating double probe measurement.<sup>17–20</sup> Electron energy distribution function is assumed as Maxwellian.<sup>12</sup> The probe tips are cylindrical stainless steel electrodes (0.5 mm diameter), with exposed length of 3 mm. The distance between the tips is 8 mm. The probe tips are placed in the chamber as show in **Fig. 1**(b).

The wafer is etched by ICP for 20 minutes. Surface profile of the etched wafer is measured by a surface roughness tester (Form Talysurf Super S5K, Taylor Hobson), and the etching rate is calculated by dividing the etching depth with the etching time.

### III. Experimental results

**Fig. 3** shows typical waveforms of (a) coil voltage and (b) current. Total gas flow rate of Ar and  $\text{CF}_4$  is 40 sccm, pressure is 2.4 Pa,  $\text{CF}_4$  content is 0%, bias voltage is -800 V, and rf power is 6 kW. The maximum coil voltage and current during the time from 0 to 30  $\mu$ s are 4.9 kV and 57 A, respectively. The impedance across the induction coil is 85  $\Omega$  at 157 kHz, which almost coincides with the calculated coil impedance of 83  $\Omega$  calculated from the amplitudes of voltage and current. In the time from 30  $\mu$ s to 200  $\mu$ s, the coil voltage and current values decrease to 1.9 kV and 26 A, respectively. The calculated value of the load impedance is 73  $\Omega$  and is almost constant value. The result indicates that the plasma is generated at the time of 30  $\mu$ s because the load impedance changed at that moment.<sup>21,22</sup> During plasma generation, the

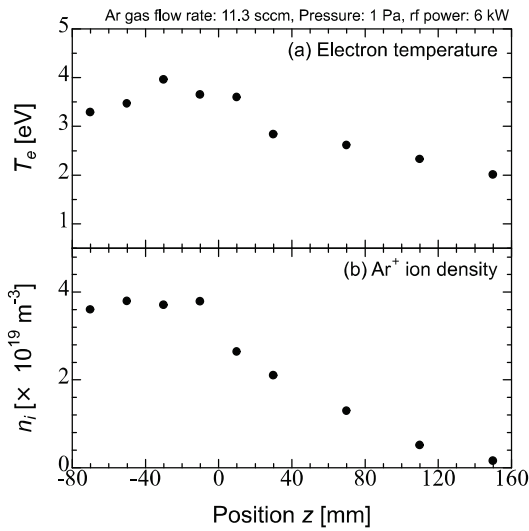


Fig. 4 (a) Electron temperature and (b) ion density for Ar plasma as functions of the position of the probe tips from the coil end.

power factor calculated from the phase difference between voltage and current is about 0.24, and the effective power of the coil is about 6.0 kW.

**Fig. 4** shows the (a) electron temperature ( $T_e$ ) and (b) ion density ( $n_i$ ) for Ar plasma as functions of the axial position  $z$ . Ar gas flow rate is 11 sccm, pressure is 1 Pa, and rf power is 6 kW. The target electrode is not placed in the chamber.  $T_e$  and  $n_i$  inside the coil are approximately 3.7 eV and  $3.8 \times 10^{19} \text{ m}^{-3}$ , respectively. As leaving from the coil,  $T_e$  and  $n_i$  drop to approximately 2.0 eV and  $1.5 \times 10^{18} \text{ m}^{-3}$ , respectively. The ion density is higher than conventional rf ICP.<sup>1)</sup>

**Fig. 5** shows the waveforms of (a) the target voltage and the target current in the cases of injecting (b) a pure Ar gas and (c) Ar/CF<sub>4</sub> mixed gas for various bias voltages. In **Fig. 5 (b)**, the target current rises from approximately 70  $\mu\text{s}$ . Target current reaches a maximum value of approximately 5.5 A at 110  $\mu\text{s}$ . The voltage drop across the current controlling resistor (5  $\Omega$ ) is several tens of volt and is small enough compared to the bias voltage. In **Fig. 5 (c)** the target current rises at the same timing as in **Fig. 5 (b)**. Target current gradually increases from 90  $\mu\text{s}$ , reaching a maximum of about 1.5 A at 200  $\mu\text{s}$ . The maximum current value is about 3 times lower than that of pure Ar gas. When the electric power supply is turned off at 200  $\mu\text{s}$ , plasma starts attenuating. Therefore, the rate of target current decays from 200  $\mu\text{s}$ . The target current gradually increases with the decrease in the bias voltage. The total ion flux into the target is almost independent to the bias voltage because the current can be increased by the expansion of the ion sheath thickness according to the Child-Langmuir law.<sup>4,23)</sup> It seems that the reaction has not reached equilibrium because the target current increases continuously, until the rf power supply is turned off as shown in **Fig. 5 (c)**. Therefore, the target current can be saturated at higher negative bias voltage. **Fig. 6** shows the waveforms of the target current for various CF<sub>4</sub> content. The bias voltage is -800 V, the total gas flow rate of Ar and CF<sub>4</sub> is 40 sccm, and rf power is 6 kW. In the pure Ar plasma without CF<sub>4</sub> gas, the target current sharply rises from about 80  $\mu\text{s}$  and has a constant value at approximately 3.4 A from 130 to 200  $\mu\text{s}$ . The plasma density decreases because of the diffusion from the ionization region, and the target current is lower than higher pressure as shown in **Fig. 5 (b)**. With increasing CF<sub>4</sub> content, the increasing rate of the target current decreases. It has been reported that the density of Ar/CF<sub>4</sub>

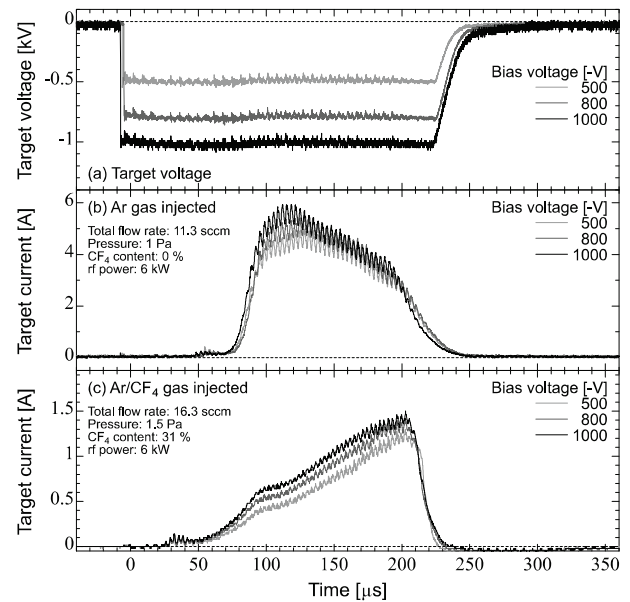


Fig. 5 Waveforms of (a) the target voltage and the target current in the cases of injecting (b) Ar gas and (c) Ar/CF<sub>4</sub> mixed gas for various bias voltages.

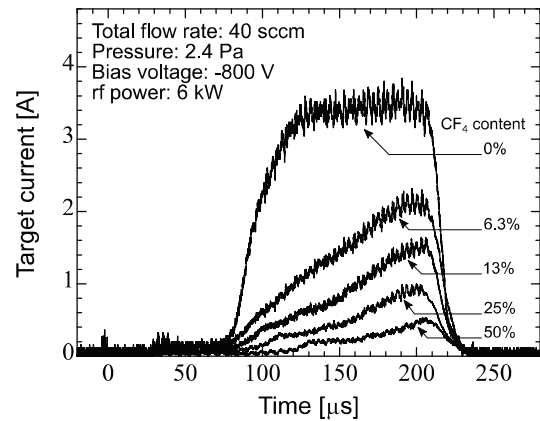


Fig. 6 Waveforms of the target current for various CF<sub>4</sub> content.

plasmas measured using a Langmuir probe decreases with increasing the CF<sub>4</sub> content.<sup>24,25)</sup> The ionization collision frequency decreases with increasing CF<sub>4</sub> content, which decreases the increasing rate of target current. With increasing the CF<sub>4</sub> content, the amplitude of the coil voltage and current and the coil impedance increased, and the power factor decreased; however, the power consumption remained almost constant. **Fig. 7** shows the waveforms of target current waveforms for various rf power. The bias voltage is -800 V, the total gas flow rate of Ar and CF<sub>4</sub> is 20 sccm, and CF<sub>4</sub> content is 25%. The target current increases with the rf power. It is considered that ion density increases with the rf power.

**Fig. 8** shows the optical emission spectra (OES) in the case of injecting pure Ar gas and Ar/CF<sub>4</sub> gas when the wavelength ranges (a) from 300 to 600 nm and (b) from 600 to 900 nm. Ar (I), Ar (II), F (I), and C<sub>2</sub> (swan band) spectra are observed.<sup>25-31)</sup> The spectra of Ar (I) and Ar (II) are mainly observed in the infrared region and the wavelength range from 400 to 500 nm. Ti (II) spectra are observed in the range of 300-400 nm.<sup>32)</sup> It is considered that Ti<sup>+</sup> ions appear in the gaseous phase by Ar<sup>+</sup> ion sputtering to the target electrode. The emission intensity of Ar (I) and Ar (II) decreases and F (I), and C<sub>2</sub> (swan band) spectra are observed with injecting

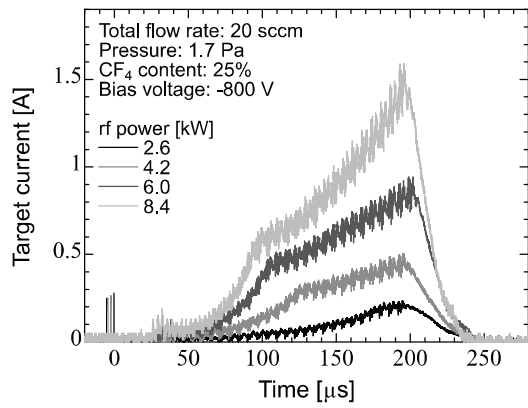


Fig. 7 Waveforms of the target current for various rf power.

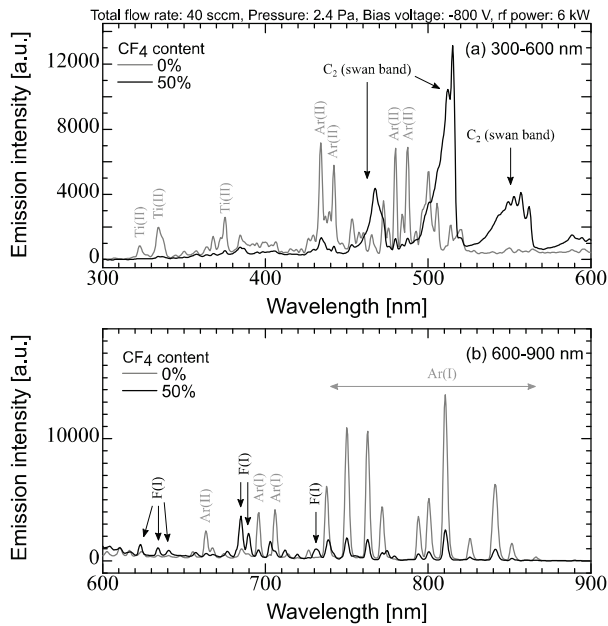


Fig. 8 Optical emission spectra in the case of injected pure Ar gas and Ar/CF<sub>4</sub> gas in the wavelength ranges (a) from 300 to 600 nm and (b) from 600 to 900 nm.

CF<sub>4</sub> gas, because the CF<sub>4</sub> is dissociated by electron collision. F (II) spectra at the wavelengths of 385 nm, 402 nm, and 425 nm, are not observed. **Fig. 9** shows the emission intensity at wavelengths of 442 and 685.6 nm, which correspond to Ar (II) and F (I), as functions of the bias voltage. The total gas flow rate is 16.3 sccm, pressure is 1.5 Pa, CF<sub>4</sub> content is 31%, and rf power is 6 kW. The emission intensity of Ar (II) and F (I) slightly increases with increasing the bias voltage. These results show that the ionization of Ar atoms and dissociation of CF<sub>4</sub> are independent to the bias voltage. **Fig. 10** shows the emission intensity of Ar (II) and F (I) as functions of CF<sub>4</sub> content. The bias voltage is -800 V, the total gas flow rate is 40 sccm, pressure is 2.4 Pa, and rf power is 6 kW. As CF<sub>4</sub> content increases, the emission intensity of Ar (II) decreases because of decrease in the Ar atom density. The emission intensity of F (I) sharply increases with increasing CF<sub>4</sub> content from 0 to 10% and become almost constant with CF<sub>4</sub> content of 10%. **Fig. 11** shows the emission intensity of Ar (II) and F (I) as functions of rf power. The bias voltage is -800 V, the total gas flow rate is 20 sccm, pressure is 1.7 Pa, and CF<sub>4</sub> content is 25%. As rf power increases, the emission intensity of Ar (II) and F (I) increase. These results show that the electron collisional dissociation of CF<sub>4</sub> is enhanced by increasing the electron density.

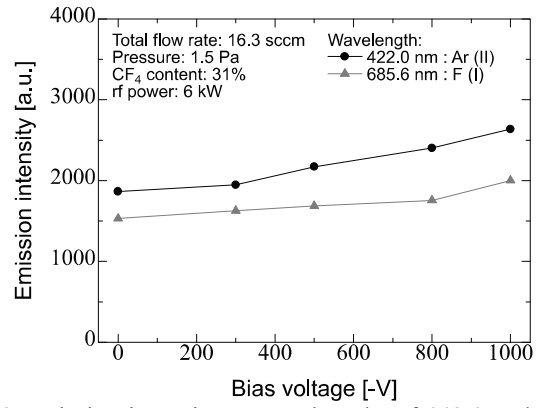


Fig. 9 Emission intensity at wavelengths of 442.0 and 685.6 nm, which correspond to Ar (II) and F (I), as functions of the bias voltage.

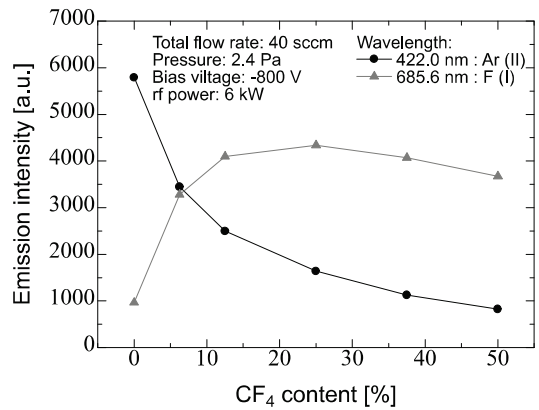


Fig. 10 Emission intensity of Ar (II) and F (I) as functions of CF<sub>4</sub> content.

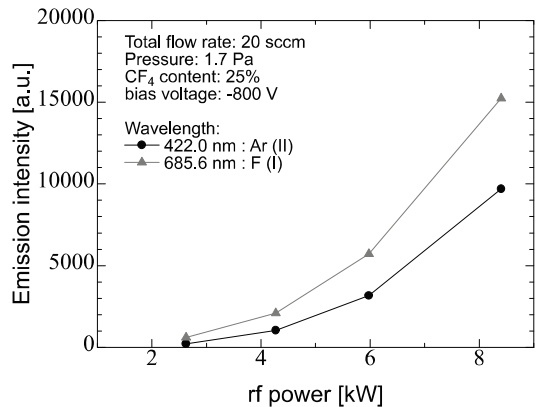


Fig. 11 Emission intensity of Ar (II) and F (I) as functions of rf power.

**Fig. 12** shows the surface profiles of silicon wafers processed in (a) a pure Ar plasma and (b) Ar/CF<sub>4</sub> plasma. The vertical axis zero means the surface of the silicon wafer before the etching process. The axis ranging of 85.7–86.7 mm and 87.7–88.7 mm are the areas of the wafer surface which are exposed to a plasma. In **Fig. 12 (a)**, the maximum etch depth is approximately 0.2 μm. The wafer is etched by Ar<sup>+</sup> ion sputtering. The metal mask made by Ti is also etched by the ion bombardment, and the fraction could deposit in the trenches. The shape of sputter-etched part (around 86 mm on the horizontal axis) is similar to the shape of the physically etched Si surface profile reported by Miyake *et al.*<sup>33)</sup> Therefore, the etching rate by Ar<sup>+</sup> ion physical etching is 0.01 μm/min. In **Fig. 12 (b)**, the etch depth is approximately 4.5

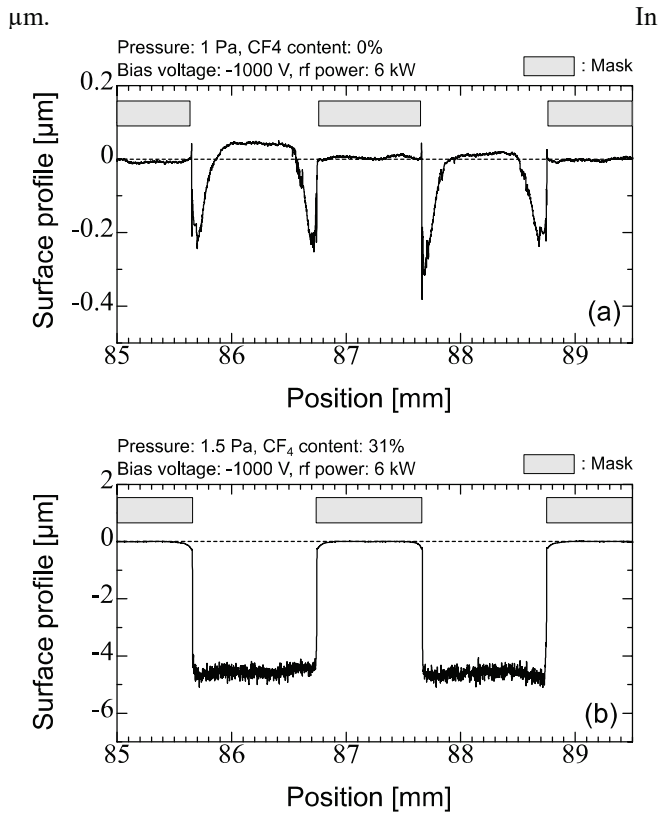


Fig. 12 Surface profiles of the silicon wafers processed in (a) a pure Ar plasma and (b) Ar/CF<sub>4</sub> plasma.

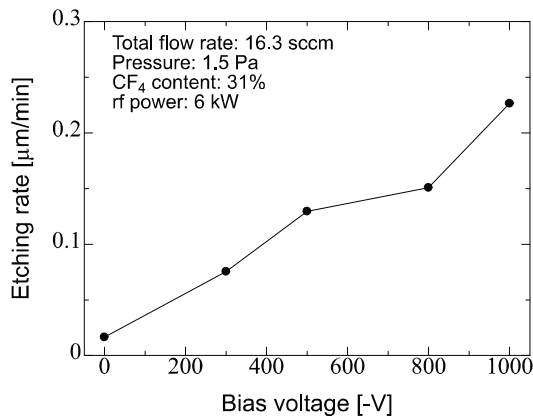


Fig. 13 Etching rate as a function of the bias voltage.

Ar/CF<sub>4</sub> plasma, no deposits seems to be observed in the bottom of the trenches. The etching rate is 0.23  $\mu\text{m}/\text{min}$  and it is 23 times faster than by physical sputter etching, which shows F atom acts as an etchant. **Fig. 13** shows the etching rate as a function of the bias voltage. The total gas flow rate is 16.3 sccm, pressure is 1.5 Pa, CF<sub>4</sub> content is 31%, and rf power is 6 kW. The etching rate is approximately proportional to the bias voltage. The results show that the increase in the reactive ion sputtering yield with increasing the bias voltage contributes to increasing the etching rate. This is because that the total ion flux and F atoms density is almost independent to the bias voltage. **Fig. 14** shows the dependence of the etching rate on CF<sub>4</sub> content. The total gas flow rate is 40 sccm, pressure is 2.4 Pa, the bias voltage is -800 V, and rf power is 6 kW. The dependence of the etching rate on CF<sub>4</sub> content almost corresponds to the emission intensity of F (I) shown in **Fig. 10**. Although the total ion flux decreases with increasing CF<sub>4</sub> content as shown in **Fig. 6**, it appears that the etching rate

is almost independent to the ion flux. Because the F atom

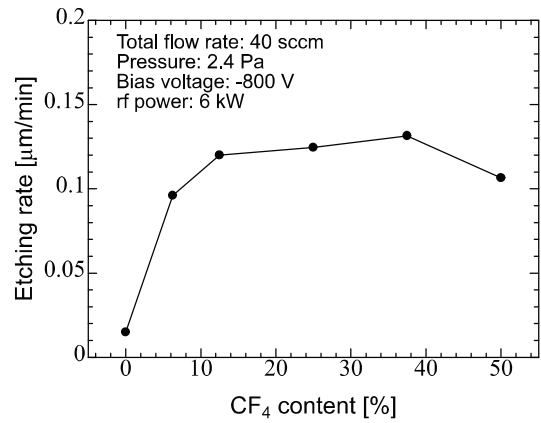


Fig. 14 Dependence of the etching rate on CF<sub>4</sub> content.

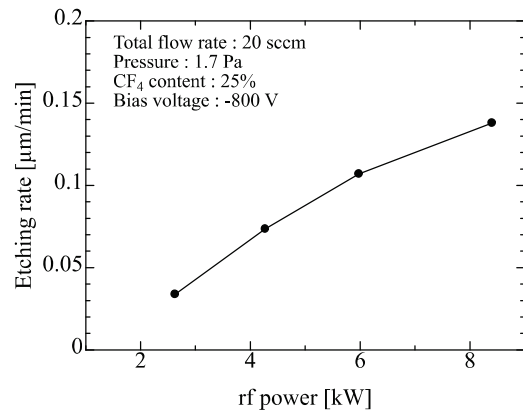


Fig. 15 Etching rate as a function of rf power.

density and the fraction of the silicon surface covered by the reaction products can be lowered, a part of the ion flux limited by this fraction contributes to the reactive ion etching. **Fig. 15** shows the etching rate as a function of rf power. The total gas flow rate is 20 sccm, pressure is 1.7 Pa, CF<sub>4</sub> content and the bias voltage is -800 V. The etching rate increases with rf power. It is considered that the increase of the positive ion density and F radical density makes the etching rate faster.

#### IV. Conclusions

Silicon wafer etching rate characteristics by the high-power pulsed inductively coupled Ar/CF<sub>4</sub> plasma is investigated. The etching rate dependence on bias voltage, CF<sub>4</sub> content, and rf power is investigated. The etching rate is compared with optical emission spectrum and current flowing into the substrate measured during the process. In a pure Ar plasma (physical sputter etching) the silicon etching rate is 0.01  $\mu\text{m}/\text{min}$ . In Ar/CF<sub>4</sub> plasma (reactive ion etching), the silicon etching rate increases with the bias voltage to the target electrode, and the maximum rate is 0.23  $\mu\text{m}/\text{min}$ . If the etching rate is proportional to the duty ratio, high-speed etching of 11.5  $\mu\text{m}/\text{min}$  at a 50% duty ratio becomes possible. The target current and emission intensity of Ar<sup>+</sup> and F\* are hardly depended on bias voltage in the range of -300 to -1000 V. With the increase of CF<sub>4</sub> content, the etching rate sharply increases from 0% to 10%, and it becomes almost constant from 10%. The emission intensity of F\* is similar to this dependence on CF<sub>4</sub> content.

## Acknowledgements

The authors are grateful to Mr. Y. Shida of Iwate University for fabrication of the experimental equipment. This work was supported by a Grants-in-Aid for Scientific Research (S) (No. 19H05611).

## References

- [1] J. Hopwood, *Plasma Sources Sci. Technol.*, **1**, p. 109, (1992).
- [2] S. Xu, K. N. Ostrikov, Y. Li, E. L. Tsakadze, and I. R. Jones, *Phys. Plasmas*, **8**, p. 2549, (2001).
- [3] U. Helmerson, M. Lattemann, J. Bohlmark, A. P. Ehiasarian, and J. T. Gudmundsson, *Thin Solid Films*, **513**, p. 1, (2006).
- [4] M. A. Lieberman and A. J. Lichtenberg, *Principles of Plasma Discharges and Materials Processing* (Wiley, New York, 2005) 2nd ed.
- [5] T. Makabe and Z. L. Petrovic, *Plasma Electronics: Applications in Microelectronic Device Fabrication* (CRC Press, New York, 2014) 2nd ed., p. 285.
- [6] K. Nakamura and H. Sugai, *J. Plasma Fusion Res.*, **74**, p. 155, (1998).
- [7] S. Banna, A. Agarwal, K. Tokashiki, H. Cho, S. Rauf, V. Todorow, K. Ramaswamy, K. Collins, P. Stout, J. Y. Lee, J. Yoon, K. Shin, S. J. Choi, H. S. Cho, H. J. Kim, C. Lee, and D. Lymberopoulos, *IEEE Trans. Plasma Sci.*, **37**, p. 1730, (2009).
- [8] D. J. Economou, *J. Phys. D: Appl. Phys.*, **47**, 303001, (2014).
- [9] M. Tuszewski, J. T. Scheuer, and R. A. Adler, *Surf. Coat. Technol.*, **93**, p. 203, (1997).
- [10] K. Yukimura and A. P. Ehiasarian, *Nucl. Instrum. Methods Phys. Res. B*, **267**, p. 1701, (2009).
- [11] K. Yukimura, H. Ogiso, S. Nakano, and A. P. Ehiasarian, *IEEE Trans. Plasma Sci.*, **39**, p. 3085, (2011).
- [12] K. Yukimura, H. Ogiso, and S. Nakano, *Vacuum*, **153**, p. 195, (2018).
- [13] K. Shibata, S. Konno, K. Takahashi, S. Mukaigawa, K. Takaki, and K. Yukimura, *Proc. IEEE 21st Int. Conf. Pulsed Power*, 2017.
- [14] Y. Saito, K. Shibata, K. Takahashi, S. Mukaigawa, K. Takaki, and K. Yukimura, *Jpn. J. Appl. Phys.*, **58**, SAAB06, (2019).
- [15] D. A. Loch and A. P. Ehiasarian, *Mater. Sci. Eng.*, **39**, 012006, (2012).
- [16] S. Hara, H. Maekawa, S. Ikeda, and S. Nakano, *Bull. Jpn. Soc. Precis. Eng.*, **77**, p. 249, (2011).
- [17] E. O. Johnson and L. Malter, *Phys. Rev.*, **80**, p. 58, (1950).
- [18] Y. Yin, J. Messier, and J. A. Hopwood, *IEEE Trans. Plasma Sci.*, **27**, p. 1516, (1999).
- [19] B. E. Cherrington, *Plasma Chem. Plasma Process.*, **2**, p. 113, (1982).
- [20] V. I. Demidov, S. V. Ratynskaia, and K. Rypdal, *Rev. Sci. Instrum.*, **73**, p. 3409, (2002).
- [21] R. B. Piejak, V. A. Godyak, and B. M. Alexandrovich, *Plasma Sources Sci. Technol.*, **1**, p. 179, (1992).
- [22] J. T. Gudmundsson and M. A. Lieberman, *Plasma Sources Sci. Technol.*, **6**, p. 540, (1997).
- [23] M. A. Lieberman, *J. Appl. Phys.*, **66**, p. 2926, (1989).
- [24] T. Kimura and K. Ohe, *Plasma Sources Sci. Technol.*, **8**, p. 553, (1999).
- [25] A. M. Efremov, D. P. Kim, and C. I. Kim, *Vacuum*, **75**, p. 133, (2004).
- [26] C. B. Labelle and K. K. Gleason, *J. Appl. Polym. Sci.*, **80**, p. 2084, (2001).
- [27] L. G. Christophorou, J. K. Olthoff, and V. V. S. Rao, *J. Phys. Chem. Ref. Data*, **25**, p. 1341, (1996).
- [28] T. Y. Jung, D. H. Kim, and H. B. Lim, *Bull. Korean Chem. Soc.*, **27**, p. 373, (2006).
- [29] R. d' Agostino, F. Cramarossa, and S. D. Benedictis, *Plasma Chem. Plasma Process.*, **2**, p. 213, (1982).
- [30] K. Sasaki, T. Wakasaki, K. Kadota, *Appl. Surf. Sci.*, **197–198**, p. 197, (2002).
- [31] Z. S. Gong, J. Sun, N. Xu, Z. F. Ying, Y. F. Lu, D. Yu, and J. D. Wu, *Diamond & Related Materials*, **16**, p. 124, (2007).
- [32] M. Audronis, V. B. Gonzalez, B. Daniel, *Surf. Coat. Technol.*, **204**, p. 2159, (2010).
- [33] S. Miyake and T. Kasai, *Bull. Jpn. Soc. Precis. Eng.*, **48**, p. 170, (1982).

## Publication List of NIFS-PROC. Series

- NIFS-PROC-109 Edited by Shigeru MORITA, Liqun HU and Yeong-Kook OH  
Proceeding of A3 Foresight Program Seminar on Critical Physics Issues Specific to Steady State Sustainment of High-Performance Plasmas 11-14 July, 2017, Sapporo, Japan  
Jan. 12, 2018
- NIFS-PROC-110 Edited by Jun Hasegawa and Tetsuo Ozaki  
Recent Developments of Pulsed Power Technology and Plasma Application Research  
Jan. 12, 2018
- NIFS-PROC-111 Edited by Liqun HU, Shigeru MORITA and Yeong-Kook OH  
Proceeding of A3 Foresight Program Seminar on Critical Physics Issues Specific to Steady State Sustainment of High-Performance Plasmas 12 - 15 December, 2017, Chongqing, China  
Jun. 11, 2018
- NIFS-PROC-112 Edited by E. Kikutani (KEK) and S. Kubo (NIFS)  
Proceedings of the meeting on Archives in Fields of Natural Sciences in FY 2017  
Oct. 18, 2018 (Written in Japanese)
- NIFS-PROC-113 Pulsed Power and High-Density Plasma and its Applications  
Edited by Koichi Takaki and Tetsuo Ozaki  
Feb. 6, 2019
- NIFS-PROC-114 The 7th Japan-China-Korea Joint Seminar on Atomic and Molecular Processes in Plasma (AMPP2018)  
Edited by Daiji Kato, Ling Zhang, and Xiaobin Ding  
May 10, 2019
- NIFS-PROC-115 CFQS TEAM  
NIFS-SWJTU JOINT PROJECT FOR CFQS -PHYSICS AND ENGINEERING DESIGN-  
VER. 2.1 2019. SEP.  
Nov. 8, 2019
- NIFS-PROC-116 Satoshi Ohdachi, Editor of the Post-CUP Workshop proceeding  
Collected papers at the 2019 Post-CUP Workshop & JSPS-CAS Bilateral Joint Research Projects Workshop,  
24th-26th July, 2019, Nagoya, Japan  
Feb. 21, 2020
- NIFS-PROC-117 Edited by E. Kikutani (KEK) and S. Kubo (NIFS)  
Proceedings of the meetings on Archives in Fields of Natural Sciences in FY2018  
June. 9, 2020 (Written in Japanese)
- NIFS-PROC-118 Edited by Tetsuo Ozaki and Sunao Katsuki  
New Development of Beam Physics and the Application by New Generation Pulsed Power Technology  
June. 29, 2020  
National Institute for Fusion Science, National Institutes of Natural Sciences  
Institute of Fusion Science, School of Physical Science and Technology, Southwest Jiaotong University
- NIFS-PROC-119 Hefei Keye Electro Physical Equipment Manufacturing Co. Ltd.  
NIFS-SWJTU JOINT PROJECT FOR CFQS -PHYSICS AND ENGINEERING DESIGN-  
VER. 3.1 2020. NOV.  
Jan. 25, 2021
- NIFS-PROC-120 Edited by Izumi Tsutsui (KEK) and Shin Kubo (NIFS)  
Proceedings of the meetings on Archives in Fields of Natural Sciences in FY2019  
Feb. 25, 2021
- NIFS-PROC-121 Edited by Hiroaki Ito and Tetsuo Ozaki  
Frontier of Advanced Pulsed Power Technology and its Application to Plasma and Particle Beam  
Nov. 08, 2021  
National Institute for Fusion Science, National Institutes of Natural Sciences  
Institute of Fusion Science, School of Physical Science and Technology, Southwest Jiaotong University  
Hefei Keye Electro Physical Equipment Manufacturing Co. Ltd.
- NIFS-PROC-122 NIFS-SWJTU JOINT PROJECT FOR CFQS -PHYSICS AND ENGINEERING DESIGN-  
VER. 4.1 2022. JAN.  
Feb. 10, 2022
- NIFS-PROC-123 Edited by Jun Hasegawa and Tetsuo Ozaki  
Recent Developments of Pulsed Power Technology and Plasma Application Research  
Feb. 5, 2023
- NIFS-PROC-124 Frontiers of Pulse Power Technology Development  
Edited by Weihua Jiang  
Feb. 5, 2023